1971

Development of high Mach number/low Reynolds number aerodynamic characteristics for a blended, double-delta wing configuration

Douglas J. Elder

DEVELOPMENT OF HIGH MACH NUMBER/LOW REYNOLDS NUMBER AERODYNAMIC CHARACTERISTICS FOR A BLENDED, DOUBLE-DELTA WING CONFIGURATION

Douglas J. Elder

A THESIS

Submitted in partial fulfillment of the requirements for the degree of
Master of Science
in
Mechanical & Aerospace Engineering
to
The Graduate School
of
The University of Alabama in Huntsville

December 1971

ABSTRACT

The Graduate School

The University of Alabama in Huntsville

Degree: **Master of Science** **College/Dept.:** **Aerospace Engineering**

Name of Candidate: **Douglas J. Elder**

Title: **DEVELOPMENT OF HIGH MACH NUMBER/LOW REYNOLDS NUMBER AERODYNAMIC CHARACTERISTICS FOR A BLENDED, DOUBLE-DELTA WING CONFIGURATION**

The National Aeronautics and Space Administration's Space Shuttle Orbiter's high Mach number/low Reynolds number (aka viscous interaction/real gas) aerodynamics were developed based on various research studies. Four wind tunnels and a three-dimensional digital computer program developed the perfect gas aerodynamic characteristics, then correlated to single curves by the viscous parameter. A rapid and accurate analytical method for calculating the pressure distribution on blunt bodies in a uniform stream and real gas aerodynamic estimations were derived by solving the energy equation behind the shock. The gas was assumed to be perfect, the flow steady and inviscid, and the ratio of specific heat varied with velocity and altitude. The principal finding showed that viscous interaction increased axial force meaningfully, and real gas induced a nose-up pitching moment due to a change in pressure distribution. The body flap had to be deflected over twice the wind tunnel deflections to maintain trim.

ACKNOWLEDGMENTS

The author gratefully acknowledges the following professors, scientists, and engineers:

THE UNIVERSITY OF ALABAMA IN HUNTSVILLE, ALABAMA

Dr. Charles Scott, Director of Instruction, recommended my acceptance to the UAH in 1964.

Dr. Keith Hollingsworth, the Chair of Mechanical and Aerospace Engineering, consented to this belated thesis manuscript being accepted for partial fulfillment for a Master of Science in Aerospace Engineering.

Dr. Jason Cassibry is a Professor in the Department of Mechanical and Aerospace Engineering and is affiliated with the Propulsion Research Center at the University of Alabama in Huntsville. He reviewed the manuscript and provided invaluable feedback for completing the thesis to fulfill a Master of Science degree in Aerospace Engineering.

Dr. J. J. Brainerd, aerospace professor, provided the knowledge and intellectually stimulating environment in "Selected Topics in Fluid and Thermal Engineering," "Hypersonic Flow Theory," "Graduate Seminar I and II," and "Thesis."

Dr. Rudolf Hermann, the Director of the UAH Research Institute and Aerospace Professor, provided the knowledge and intellectually stimulating environment in "Compressible Fluid Flow," particularly rarefied flow.

THE UNIVERSITY OF ALABAMA, TUSCALOOSA, ALABAMA

Dr. Julian Doughty, aerospace professor, provided the knowledge and intellectually stimulating environment in "Boundary Layer Theory I and II" and "Hypersonic Flow Theory Special Problems."

MENTORS

Dr. David Dennis, a Junior High School science teacher, taught me the basics of rocketry and science fairing by starting the first school rocket club in the nation in 1955.

Konrad Dannenberg, the Deputy Manager of the Saturn Program, brought me to Huntsville, Alabama, to work as a college summer student in the NASA/MSFC Aerodynamic Design Branch (R-Aero-AD).

Edward L. Linsley, the Chief of the NASA/MSFC Aerodynamic Design Branch (R-Aero-AD), was my first aerospace engineering supervisor.

TABLE OF CONTENTS

LIST OF FIGURES

LIST OF TABLES

LIST OF SYMBOLS

a	Speed of sound, ft/s.
C	Factor of proportionality in the linear viscosity-temperature relation.
C_A	Axial force coefficient.
C_D	Drag Coefficient
C_M	Pitching moment coefficient.
C_N	Normal force coefficient.
C_p	Specific heat at constant pressure.
d	Dissociation length, ft.
G	Newtonian similarity parameter, $G(\gamma, \varepsilon, V, \eta)$.
H	Total enthalpy.
H	Static enthalpy.
Kn	Knudsen number, l/x
$\bar{K}^*_{\delta_{sc}}$	Viscous/Gas Parameter, $\bar{V}^*_{\delta_{sc}}$ /λ.
L	Vehicle length.
l	Mean free path length of a molecule, ft.
L/D	Lift-to-drag ratio.
M	Mach number.
p	Pressure
$\boldsymbol{P_n}$	Normalized pressure p.
Q	Ratio of local velocity to freestream velocity.
q	Dynamic pressure, lb/ft^2.
Re	Reynolds number.
$\mathcal{R}$	Gas constant, ft^2°Rs^2.
r	Nosetip radius, ft.
S	Distance is measured from the stagnation point along the surface.
T	Temperature, °R.
V	Velocity
$\bar{V}'$	Viscous (slip) parameter, $M^3\sqrt{C}/\sqrt{Re}$.
Z	Compressibility factor.
γ	Ratio of specific heats.
ε	Inverse of the density ratio, ρ_∞/ρ
η	Angle between the freestream velocity vector and the surface unit normal vector, degrees.
λ	Gas parameter, (γ-1) / (γ+1).
μ	Viscosity, lb s/ft^2.
ρ	Density, lb s^2/ft^4.
θ	Cone half angle.

Subscripts

L	Based on local flow field properties.
p	Pressure force and moment components.
r	Recovery factor.
∞	Freestream Conditions
std	standard conditions.
sl	Sonic line conditions.
ns	Normal shock conditions.
t	Total conditions
v	Viscous force and moment components.
w	Wall conditions.
δ	Based on local flow field properties at the outer edge of the boundary layer.
∞	Freestream conditions.

Superscripts

*’	Based on reference temperature.

CHAPTER 1

INTRODUCTION

During flight tests, the United States Air Force and Navy reentry vehicles (RV) routinely pass through the high altitude, viscous interaction/real gas regime. Until recently, RV configurations were mass-balanced and designed to fly ballistic trajectories, i.e., angles of attack and lift-to-drag ratios of roughly zero. With little or no angle of attack, both viscous interaction and real gas effects have little influence on overall system performance and effectiveness. On the other hand, it was anticipated in the late 1960s, but unproven, that viscous interaction and real gas flowfields would strongly affect system performance and effectiveness for a reentering spacecraft. The general lack of knowledge about the relationship between viscous interaction and real gas effects produced an environment of no practical means, either experimental or analytical, to study the combined impact on aerodynamic characteristics. There was the paradox of correlating perfect gas aerodynamics by Mach number, Reynolds number, Knudsen number, viscous (slip) parameter, or viscous interaction parameter with the expectation of replicating real gas effects. Coupling the two phenomena with one parameter seemed questionable since it was thought that viscous interaction mainly affects skin friction along the surface, and real gas mainly affects pressure on the surface.

On July 26, 1972, NASA announced that Rockwell International (RI) was selected as the prime contractor for the Space Shuttle—specifically the reusable Orbiter—after intense competition with McDonnell Douglas, Lockheed, and Grumman. Hence, the Orbiter became the first lifting body-wing configuration—a complex blended, double-delta wing at an angle of attack—developed for reentry from orbit. It was designed to perform an unpowered, gliding reentry from orbit at approximately 600,000 ft. (183 km). It would first experience rarefied air in the low-density, non-continuum flow regime where dynamic pressure is less than 1.0 psf. Then, between 350,000 ft. (107 km) and 300,000 ft. (91 km), it would enter the continuum, viscous interaction/real gas flow regime where dynamic pressure would rapidly increase. From its entry to approximately 240,000 ft. (73 km or a Mach number of 24), the angle of attack would vary between 40° and 42° to reduce some velocity before entering the higher-density air, where aerodynamic heating would be a significant design issue. Peak heating would last for another 10 minutes, from 240,000 ft. (73 km), while a gradual pitch down would be performed over the next 40,000 ft. Finally, it would only reach an angle of attack of 31° at approximately 200,000 ft. (61 km or a Mach number of 18). By then, the viscous interaction effects would become not discernible, but real gas effects would remain measurable for another 50,000 ft.

Because available aerodynamic prediction methodologies had limited applicability for complex configurations, both NASA and Rockwell International (RI) Space Division understood that knowledge of the hypersonic flowfield over the Orbiter would be challenging. Thus, the program aimed to obtain the best possible preflight predictions through an extensive wind tunnel test program on the order of 100,000 hours of test time to conduct aerodynamic, thermodynamic, and structural dynamics.

With this goal, the Orbiter was tested in all available hypersonic wind tunnel facilities in the United States between early 1973 and 1975. Even so, only ideal (perfect) gas aerodynamic characteristics were obtainable in ground-test facilities since wind tunnels could not adequately simulate flight properties of real gas chemistry from 325,000 ft. down to 120,000 ft. In addition, the two major wind tunnels available for deriving the aerodynamic characteristics for high Mach number/low Reynolds number flow produced poor data quality, requiring major corrections to salvage their usefulness, namely:

- Arnold Engineering Development Center's (AEDC) von Karman Facility (VKF) Hotshot Tunnel F flowfield was contaminated by fine dust particles. The dust particles were produced by the vaporization of small amounts of copper, tungsten, and beryllium during electrical discharge in the tunnel's arc chamber. In addition, source flow and flow non-uniformities in the nozzle further contributed to the poor data quality. A joint and cooperative effort with the test facility resulted in the development of two methods to correct the data: one by this thesis candidate and one by the VKF engineers.

- CALSPAN Corporation's 48-inch shock tunnel's pitot probe used to measure dynamic pressure—required to compute aerodynamic force and moment coefficients—was mounted too far from the model and too close to the tunnel boundary layer to provide reliable values of dynamic pressure. It was also believed that misalignment of parts in the nozzle and irregularities downstream of the throat contributed to larger-than-normal errors. A solo effort by this thesis candidate resulted in the development of a method to correct the data and thus salvage its usefulness.

After correcting the data of the two test facilities, the force and moment data were correlated to single curves by the viscous (slip) parameter based on freestream properties. This correlation parameter best incorporates the Mach number, Reynolds number, and the factor of proportionality in the linear viscosity-temperature relationship. The methodology assumed that data points from the experimental and theoretical correlated curves could be extrapolated to locations on the trajectory profile having the same correlated values. This meant that the limited aerodynamic database obtained from AEDC Tunnel F and CALSPAN shock tunnel could be correlated and then extrapolated to the entire high-altitude flight trajectory from 300,000 ft. down to approximately 160,000 ft.

1.1 STATE-OF-THE-ART BEFORE 1973

Developing a coherent hypersonic aerodynamic database consisting of many variables (e.g., altitude, velocity, the complexity of the design, angle of incidence to the flow, control surface deflections, etc.) for the Orbiter configuration was a daunting challenge for the start of the program.

1.1.1 Hypersonic Arbitrary Body Aerodynamic Computer Program

The best program available for determining the hypersonic aerodynamic characteristics of the Orbiter was the Hypersonic Arbitrary Body Aerodynamic Computer Program[1] (HABP) [1]. The program was developed as a general engineering tool used in design and analysis studies, distinguished from theoretical research (i.e., numerical) flowfield codes.

---

[1] HABP was developed and became operational in 1968 by A.E. Gentry, et al, Douglas Aircraft Co., Inc., Santa Monica, California. This thesis candidate became skilled using the code in January 1969, as a graduate student with McDonnell-Douglas in St. Louis, Missouri.

HABP uses a combination of techniques and capabilities to perform complete aerodynamic analyses. For example, pressure calculation methods include modified Newtonian, blunt-body Newtonian-Prandtl-Meyer, tangent-wedge, tangent-cone, shock-expansion, Prandtl-Meyer expansion, blast wave, modified tangent-cone, boundary layer induced pressure, free molecular flow, and several empirical relationships.

Viscous forces, including viscous interaction effects, are also considered. Skin friction options include the Reference Temperature and Reference Enthalpy methods (for both laminar and turbulent flow), the Spalding Chi (for turbulent flow), and a special-blunt body skin friction method.

The HABP developers made an outstanding attempt to develop a program capable of analyzing arbitrary geometric shapes at hypersonic speeds, which was indeed an advancement in the state-of-the-art. However, most methods are semi-empirical and straightforward analytical solutions, thus configuration-dependent. In most cases, the calculation methodology's validity depends on the body shapes immediately upstream of the point of interest, the shock shape, and body curvature. In addition, most calculation methods are applicable only for two-dimensional flow, but a few can be applied to three-dimensional flow with some degree of confidence. It must be remembered that the HABP is an impact solution rather than a flowfield solution such as those under development by NASA, DoD, and the academic community.

It must be emphasized that the aerodynamicist specifies the particular method most suitable for each vehicle component. Thus, the more knowledgeable and skilled the aerodynamicist is with flowfield properties and HABP modeling, the better the results.

1.1.2 Correlation Parameters

Because of computational limitations, many investigators were concerned with developing schemes for correlating a limited theoretical and experimental aerodynamic database for predicting preflight aerodynamics [2-14]. They examined various parameters to correlate aerodynamic characteristics, temperature, skin friction, boundary layer transition, base pressure, etc. Probably the best-known correlation parameters that were investigated for use in the high-altitude flow regime were Mach number (*M*), Reynolds number (*Re*), Knudsen number (*Kn*), viscous (slip) parameter ($\bar{V}'$), and viscous interaction parameter ($\bar{X}$).

With that said, the state-of-the-art for predicting the high Mach number/low Reynolds number aerodynamics for complex, lifting body-wing configurations, such as the Orbiter, needed to be improved in technical maturity. Many NASA and Rockwell International Space Division engineers did not view existing computational tools confidently before the program started. They felt that the state-of-the-art computational methods could not produce conclusive predictions of flight aerodynamics. With justification, both organizations had far greater faith in wind tunnel data measurements than theoretical predictions.

1.2 STATEMENT OF THE PROBLEM

Five problem areas were identified in the development of high Mach number/low Reynolds number aerodynamic characteristics of the Orbiter:

1. No high Mach number/low Reynolds number wind tunnel data was available for theoretical predictions to compare with. *Problem: Having no experimental data*

for similar configurations would delay determining the quality of theoretical tools until wind tunnel tests were performed.

2. No high Mach number/low Reynolds number flight data was available for theoretical/experimental predictions to compare with. *Problem: Having no flight data for similar configurations would delay determining the quality of theoretical and wind tunnel data until after the first flight. The Orbiter development bypassed the general rule for manned reentry programs: "develop slowly and cautiously from safe to more severe entry conditions (e.g., Apollo)."*

3. No CFD solutions for computing flowfield and aerodynamic characteristics would be available. *Problem: The HABP was a perfect gas impact solution and had never been calibrated against flight data for complex configurations.*

4. No computational tools were available for computing real gas effects. *Problem: Without understanding real gas's effects on vehicle stability and control, a high degree of uncertainty would be introduced for the first reentry.*

5. The viscous parameter, $\bar{V}_{\infty}'$, had never correlated experimental data and then extrapolated it to flight conditions for complex configurations. *Problem: Without understanding the accuracy of extrapolating wind tunnel predictions to flight conditions, a high degree of uncertainty would be introduced for the first reentry.*

1.2.1 Technology Limitations

The DoD, NASA, and academia had yet to develop numerical CFD flowfield codes needed to substantiate the wind tunnel and theoretical aerodynamic predictions to be developed in this research work. HABP was available for predicting perfect gas

aerodynamic characteristics. AEDC Tunnel F and CALSPAN 48-inch shock tunnel were experienced in hypersonic testing. Still, they needed more experience with large angles of attacks and simulating Orbiter high-altitude flight conditions.

1.2.2 How Technology Limitations Resolved

There were four steps identified to solving the five problem areas listed above:

1. Develop the Orbiter's low-altitude, hypersonic aerodynamic characteristics from wind tunnel measurements and HABP computations for a Mach number range from 5 to 10. NASA/Ames Research Center's 3.5-ft hypersonic blowdown tunnel (Mach 5, 7, and 10) and USAF Arnold Engineering Development Center's (AEDC) von Karman Facility (VKF) continuous wind tunnels B (Mach 6 and 8) and C (Mach 10) were the available tunnels capable of achieving Mach numbers 5 to 10. These tunnels would establish the starting conditions for the viscous interaction regime.

2. Develop the Orbiter's high-altitude, hypersonic aerodynamic characteristics from wind tunnel measurements and HABP calculations for a Mach number range from 10 to 20. AEDC VKF Hotshot Tunnel F and CALSPAN Corporation's 48-inch shock tunnel could achieve Mach numbers 10 to 20.

3. Correlate the HABP predictions and the AEDC Tunnel F and CALSPAN 48-inch shock tunnel data by the viscous parameter, $\bar{V}_{\infty}'$, based on freestream conditions.

4. Derive "incremental" aerodynamic characteristics (i.e., $\Delta C_{M_{Real\,Gas}}$) and add to resultant wind tunnel/theoretical aerodynamic characteristics (i.e., $C_{M_{total}} = C_{M_{Ideal\,Gas}} + \Delta C_{M_{Real\,Gas}}$) to derive flight predictions.

1.2.3 Hypothesis

It was assumed that normal force and axial force coefficients derived from wind tunnel and ideal gas computations might be sufficiently accurate for making preflight predictions. Viscous interaction would mainly affect the axial force, whereas real gas would affect the pressure distribution on the body at a high angle of attack, hence the pitching moment. Thus, the deficiency of the wind tunnel-derived pitching moment data would most likely require adjustment to compensate for real gas effects.

Eight unconfirmed hypotheses were defined at the start of this effort:

1. Viscous interaction should mainly affect the shear and axial force coefficient.
2. Viscous interaction should only have a negligible effect on the normal force coefficient.
3. Viscous interaction should cause significant degradation in the lift-to-drag ratio.
4. An increase in axial force coefficient due to viscous interaction might enhance a nose-down pitching moment and increase stability.
5. Normal force and axial force coefficients derived from wind tunnels and perfect gas computations should be sufficiently accurate for making preflight predictions.
6. The viscous parameter, $\bar{V}_{\infty}'$, should be suitable for correlating high Mach number/low Reynolds number normal force and axial force data from wind tunnel and HABP.
7. Real gas chemistry should change the pressure distribution on the body and hence change the pitching moment, resulting in the need to correct the ideal gas pitching moment values.

8. The pressure distribution over the entire lower surface might change proportionally with the inverse of the sonic density ratio (ε_{sl}) during reentry; i.e., only one pressure distribution can exist for only one sonic line condition.

1.3 THESIS CANDIDATE'S CONTRIBUTIONS

What part of the Space Shuttle Orbiter reentry hypersonic aerodynamics and this thesis was the author responsible for developing? The following reviews his contributions.

Prerequisite Hypersonic Experience: From 1969 to January 1973, Lockheed Missiles and Space Co. employed me on Bradford Drive, Huntsville, AL., supporting the NASA/MSFC Aerodynamic Design Branch (R-Aero-AD) as an in-house contractor. Simultaneously, I was studying in the evenings toward my graduate degree in high-speed Fluids, Thermodynamics, and Engineering Math at the University of Alabama in Huntsville. Based on my knowledge of using HABP [1], the Aerodynamic Design Branch assigned me to develop hypersonic aerodynamic characteristics on numerous space shuttle concepts under their internal investigation and appraisal, including those by various NASA organizations, Rockwell International, McDonnell Douglas, Lockheed Missile & Space, and Grumman. I further developed the Aeromaneuvering Orbiter-to-Orbit Shuttle (AMOOS) concept and resultant hypersonic aerodynamics for NASA.

Rockwell International Employment: On July 26, 1972, NASA announced that Rockwell International (RI) was selected as the prime contractor for the Space Shuttle. As a result, over thirty-five RI engineers were involved in developing the Orbiter aerodynamics from a Mach number of 5 down to subsonic and landing at the Downey, CA, facility. At the same time, RI offered me a position to develop the Orbiter's hypersonic

aerodynamic characteristics from reentry to approximately Mach number 5.0. This included conducting all experimental and theoretical studies. In addition, the agreement with RI was that the research results could be used for my UAH thesis.

I would attend pre-test and post-test meetings, judge the quality of the data, compare it with my theory, and decide what test should be conducted next. The wind tunnel test team always consisted of (1) one or two model men to handle changing model parts such as elevons and the body flap; (2) a test engineer to interact closely with the facility engineers; and (3) himself, the aerodynamic engineer. I also developed methodologies with facility engineers to correct poor-quality data and salvage its usefulness. In addition, I hand-plotted the hundreds of wind tunnel data points on engineering graph paper (plotters were yet to be available) numerous times to obtain the aerodynamic characteristics as a function of control surface deflections, angles of attack, Mach number, viscous parameter, etc. In parallel with the wind tunnel test, I developed the perfect gas, inviscid/viscous aerodynamic characteristics using the HABP code, and real gas aerodynamic estimations by solving the energy equation behind the shock. Finally, I was responsible for developing the hypersonic database that would be relevant to NASA through the RI's "*Substantiation Report*" and *"Aerodynamic Design Data Book (ADDB).*"

Though I was the principal engineer in developing the hypersonic aerodynamic characteristics of the Orbiter vehicle, I note the most valuable contributors' work throughout this thesis and the References at the end. In addition, I typed and assembled this thesis from my internal technical papers in References.

NEXT CHAPTER DESCRIPTION

The next chapter, Chapter 2, describes the Orbiter's reentry flight characteristics predicted early in the Orbiter's concept development. First, a description of the Orbiter's configuration is presented. Then, the reentry altitude, Mach number, velocity, freestream dynamic pressure, Reynolds number, viscous parameter, and angle of attack are shown. The viscous parameter used to correlate the aerodynamic characteristics is defined.

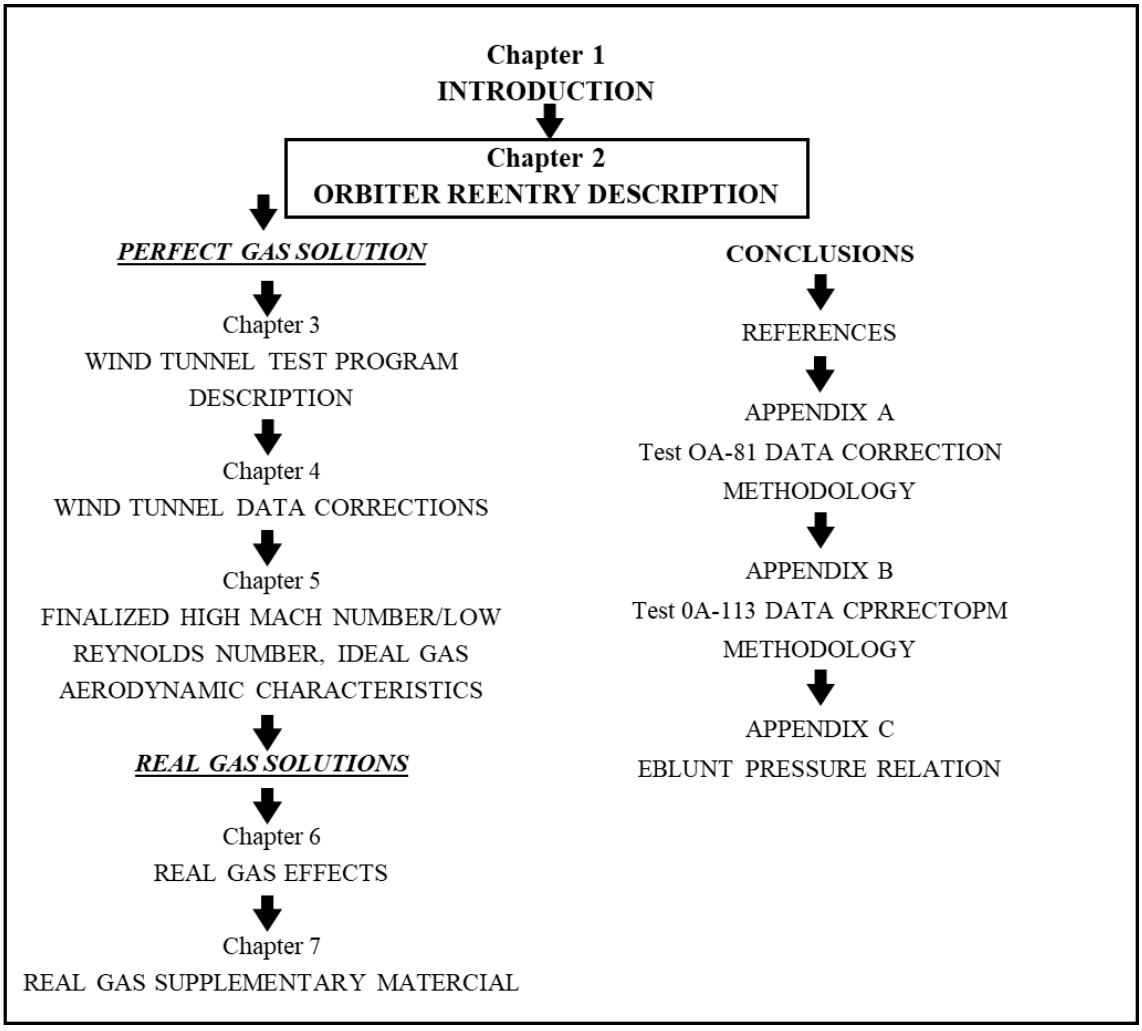

CHAPTER 2

ORBITER REENTRY DESCRIPTION

The Orbiter configuration is a blended, double-delta wing geometry when the lower surface is viewed at an angle of attack. The body flap is used as the primary trim device. The thick, double delta wings are configured with full-span elevons, comprising two panels per side. Each elevon panel is independently actuated. To obtain pitch control, all four panels are deflected symmetrically. To get roll control, the left and right elevons are deflected differentially. Aerodynamically, the Orbiter is longitudinally and laterally stable during a significant portion of the flight. Figure 2.1 shows Configuration 140A/B, the baseline configuration for all hypersonic wind tunnel tests between 1973 and 1975.

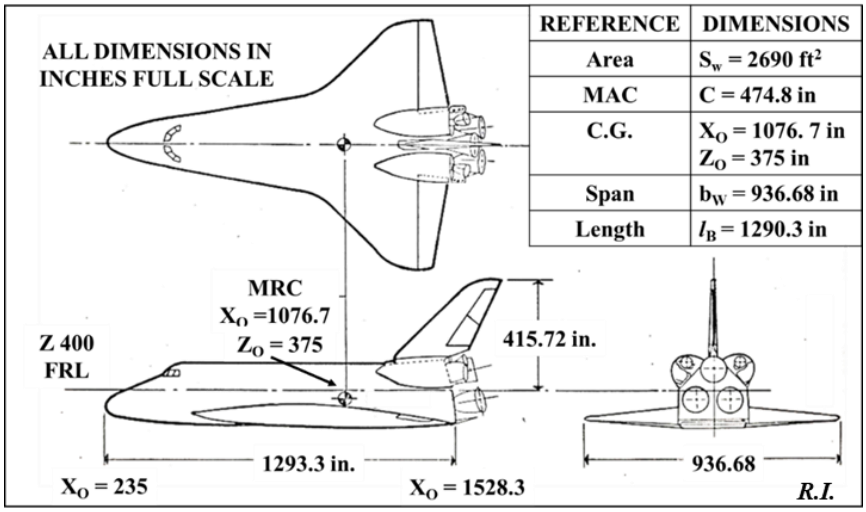

Figure 2.1 Orbiter Configuration 140 A/B [15]

2.1 HYPERSONIC REGIME

Based on the state-of-the-art, the flow regime was divided into two major categories: non-continuum and continuum flow. The non-continuum flow regime consists of (1) free-molecular flow, (2) transitional flow, and (3) slip flow. Though interesting from an academic viewpoint, the dynamic pressures are too low to produce meaningful aerodynamic forces. Thus, the Orbiter is controlled in roll, pitch, and yaw with aft-mounted, side-firing reaction control system (RCS) jets from approximately 400,000 ft. The aft RCS roll jets are deactivated when the Orbiter's ailerons become effective at a dynamic pressure of 10 lb/ft2. At a dynamic pressure of 20 lb/ft^2, the Orbiter's elevons become effective, and the aft RCS pitch jets are deactivated.

The major continuum flow regimes are described as follows, and the change in dynamic pressure as a function of altitude and velocity (Mach number) is illustrated in Figure 2.2.

1. High Mach number/low Reynolds number (aka viscous interaction/real gas) regime: altitudes from approximately 350,000 ft. (107 km) to 210,000 ft. (64 km), and for Mach numbers greater than 18.

2. Inviscid shock layer dominant flow field/real gas regime: altitudes from 210,000 (64 km) to 175,000 ft. (53 km), and for Mach numbers greater than 12.

3. Mach number dependence regime, inviscid shock layer: Altitudes from 175,000 (53 km) to 120,000 ft. (37 km) and for Mach numbers greater than 5.

The change in Reynolds number and altitude with velocity (Mach number) is shown in Figures 2.3 and 2.4.

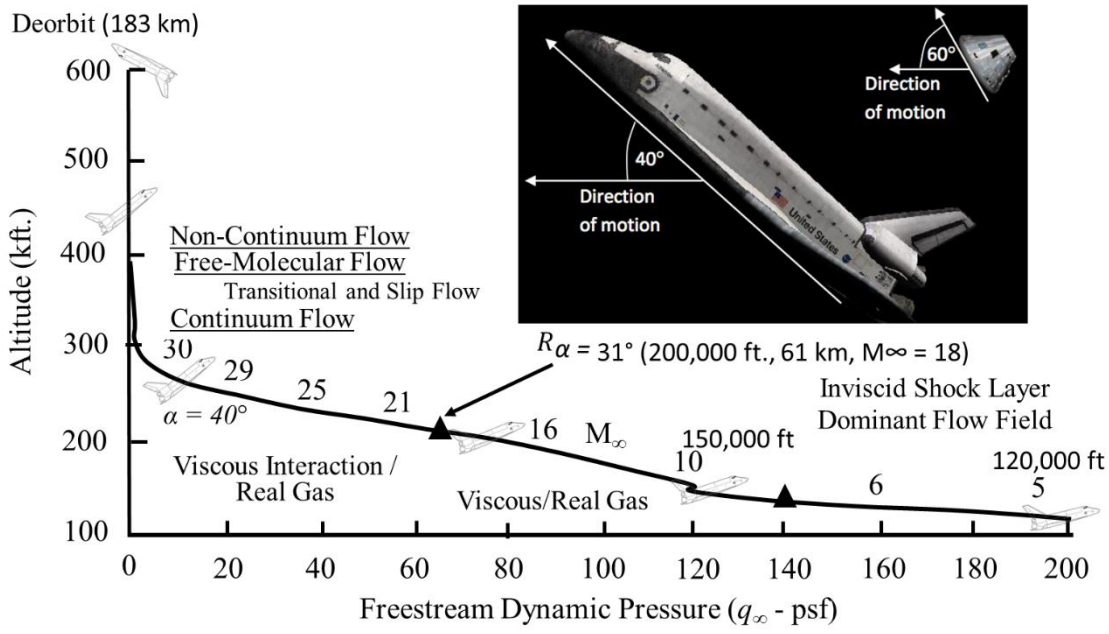

Figure 2.2 140 A/B Orbiter reentry freestream Mach number change with altitude and dynamic pressure

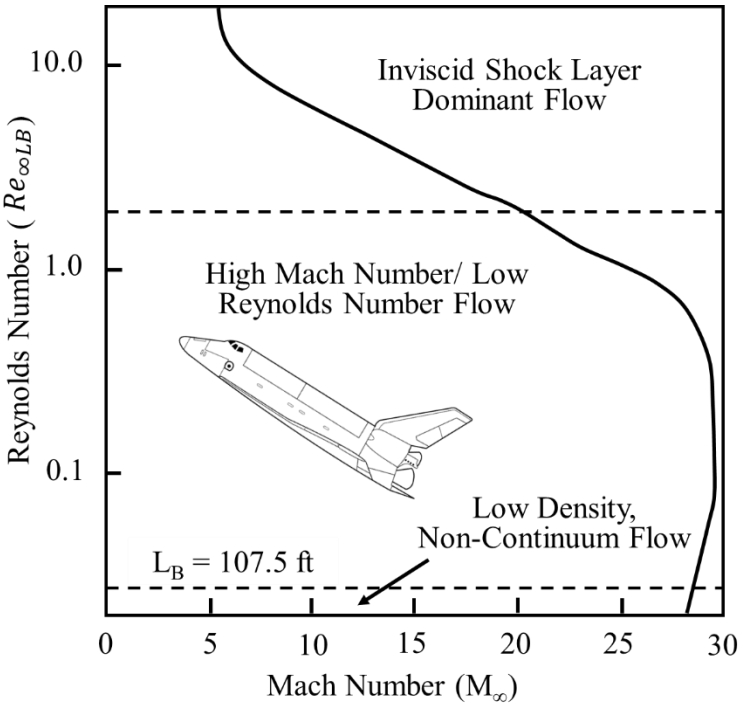

Figure 2.3 140 A/B Orbiter reentry freestream Reynolds number change with Mach number

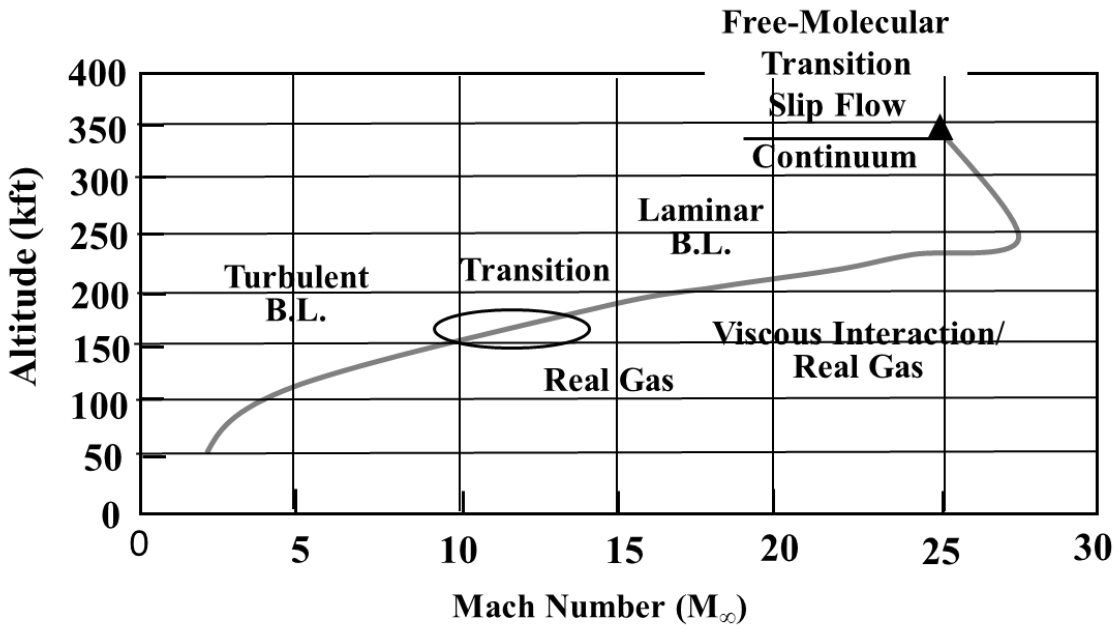

Figure 2.4 140 A/B Orbiter reentry Mach number changes with altitude

The above three figures show how dynamic pressure and Reynolds number increase with descending altitude and decreasing velocity (Mach number) from 300,000 feet to 125,000 feet—hypersonic regime.

2.2 VISCOUS PARAMETER

The high Mach number/low Reynolds number regime ranges in altitude from approximately 350,000 ft. (107 km) down to 210,000 ft. (64 km) and ranges in Mach number from 28 down to 18. During this high Mach number/low Reynolds number flight, the boundary layer expands outwards towards the shock wave. Under the most severe conditions ($\bar{V}_\infty' > 0.06$), the boundary layer grows thicker and can merge with the shock wave.

The viscous parameter, $\bar{V}_\infty'$, was selected as the correlating parameter—based on a sharp flat plate and ideal gas assumptions. The viscous parameter is defined as [16, 17]:

$$\bar{V}'_{\infty} = \frac{M_{\infty}\sqrt{C'_{\infty}}}{\sqrt{Re_{\infty\,L}}}, \tag{2.1}$$

where M_{∞} is the freestream Mach number, $Re_{\infty\,L}$ is the freestream Reynolds number based on Orbiter length, and C'_{∞} is the linear viscosity-temperature relation defined by:

$$C'_{\infty} = \frac{\mu'}{\mu_{\infty}}\frac{T_{\infty}}{T'} = \left[\frac{T'}{T_{\infty}}\right]^{K}\left[\frac{T_{\infty} + 122.1x10^{-(5/T_{\infty})}}{T' + 122.1x10^{-(5/T')}}\right]^{J}, \tag{2.2}$$

where K = 0.5 and J = 1.0 for air. Monaghan's empirical temperature relationship, based on freestream properties, is:

$$\frac{T'}{T_{\infty}} = \left[\left(1 - 0.468Pr^{1/3}\right)\frac{T_W}{T_{\infty}} + 0.468Pr^{1/3} + \left(0.468Pr^{1/3} - 0.273Pr^{1/2}\right)Pr^{1/2}\left(\frac{T_t}{T_{\infty}} - 1\right)\right], \tag{2.3}$$

where T_W is the wall temperature, T_{∞} is the freestream static temperature, and

$$\frac{T_t}{T_{\infty}} - 1 = \frac{\gamma_{\infty} - 1}{\gamma_{\infty}}M_{\infty}^2, \tag{2.4}$$

where γ_{∞} is the freestream ratio of specific heat of the gas.

Figure 2.5 shows how the viscous parameter based on freestream conditions, Equation 2.1, changes with altitude for the Orbiter as the altitude decreases from 350,000 ft. (107 km) to 210,000 ft. (64 km), and $\bar{V}'_{\infty}$ decreases from approximately 0.50 to 0.008. Figure 2.6 shows how the angle of attack changes with the viscous parameter.

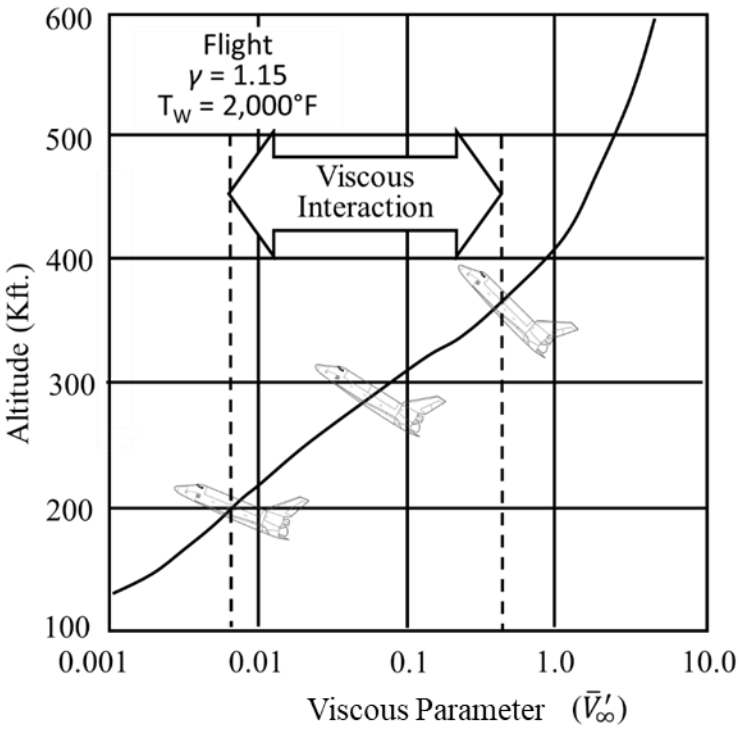

Figure 2.5 The 140 A/B Orbiter viscous interaction regime as a function of altitude

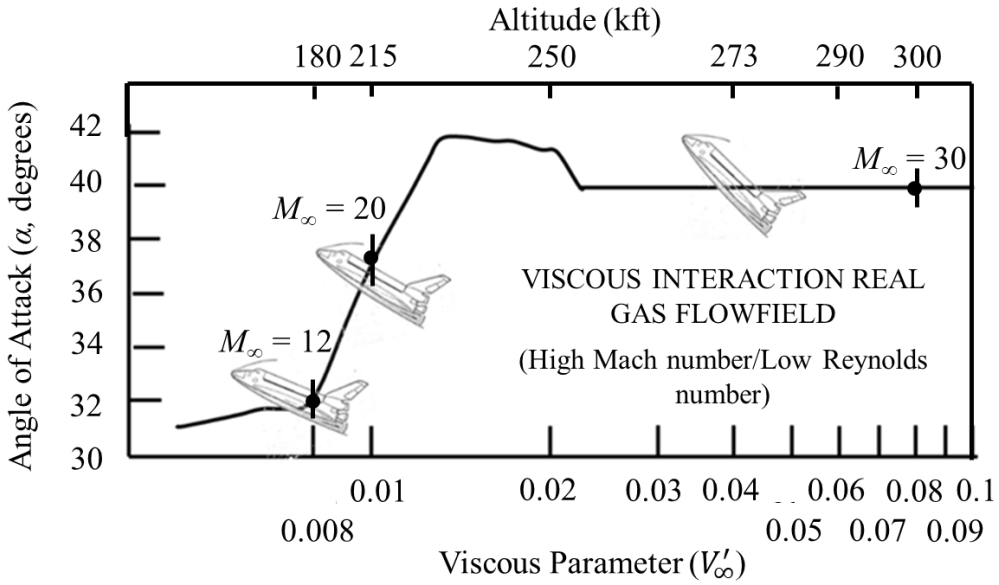

Figure 2.6 The 140 A/B Orbiter angle of attack as a function of viscous parameter and Mach number

NEXT CHAPTER DESCRIPTION

The next chapter, Chapter 3, describes the Orbiter's hypersonic wind tunnel test programs. The wind tunnel simulation flight conditions, model description, test facility description, and instrumentation description are described. The wind tunnel facilities provided most of the facilities and instrumentations' descriptions.

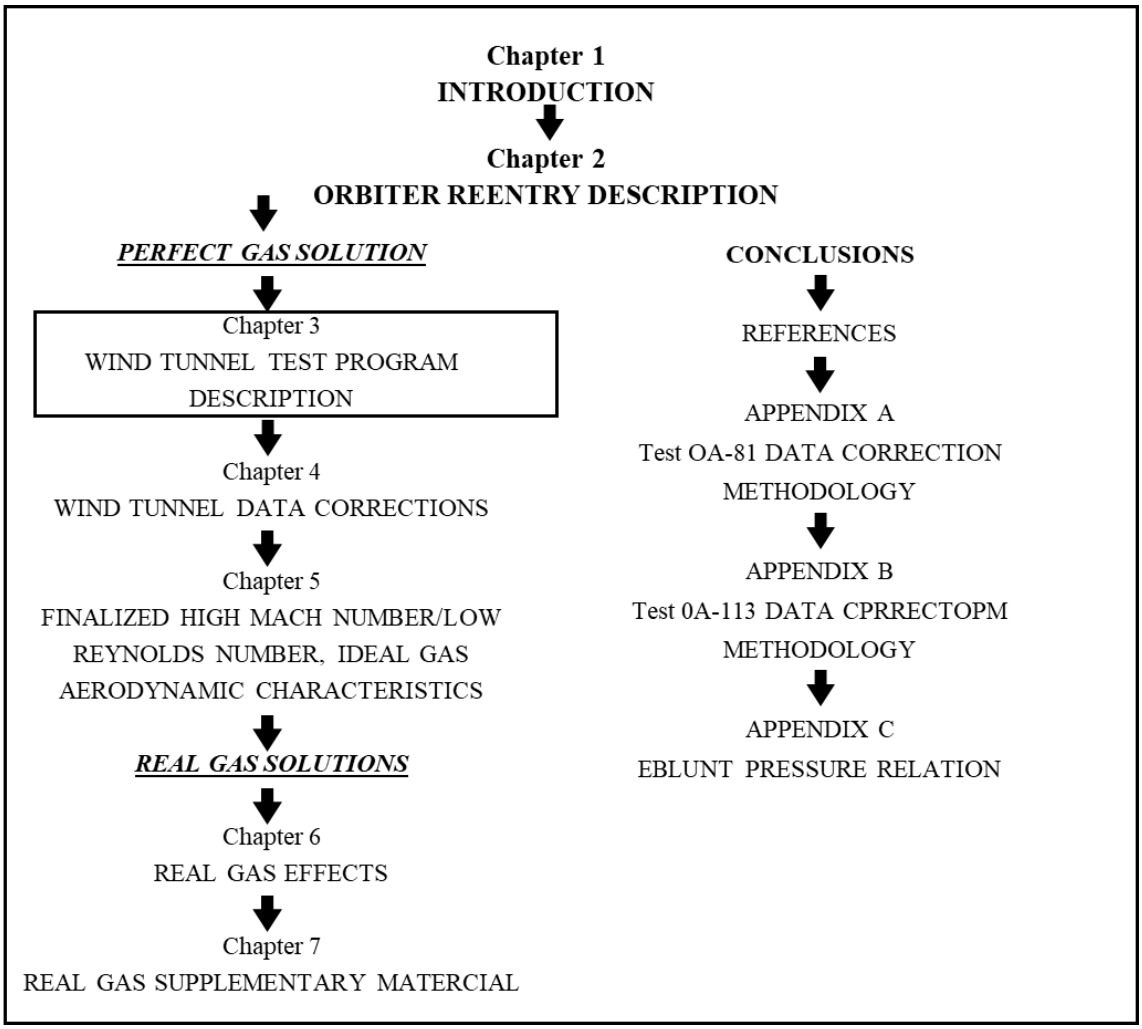

CHAPTER 3

WIND TUNNEL TEST PROGRAM DESCRIPTION

The 140 A/B Orbiter configuration's hypersonic aerodynamic characteristics were derived from four ground facilities: (1) NASA/Ames Research Center's 3.5-ft hypersonic blowdown tunnel (Mach 5, 7, and 10); (2) USAF Arnold Engineering Development Center's (AEDC) VKF (von Karman Facility) Continuous Wind Tunnels B (Mach 6 and 8) and C (Mach 10); (3) AEDC VKF Hotshot Tunnel F (Mach 16 and 20); and (4) CALSPAN Corporation's 48-in shock tunnel (Mach 10 and 16). In addition, tests were conducted in NASA/Langley Research Center's Air, Nitrogen, Helium, and Freon tunnels. Though potentially promising, the data quality was so questionable that it was discarded for use in developing the Orbiter hypersonic aerodynamics.

3.1 WIND TUNNEL SIMULATION OF FLIGHT CONDITIONS

The AEDC Tunnel F (Test OA-81) was conducted between November 26 and December 27, 1973, and the CALSAPN Shock Tunnel (Test OA-113) was conducted between August 10 and October 4, 1974. These were the two high Mach number/low Reynolds number test facilities used to develop the aerodynamic database in the viscous interaction regime for ideal gas. The test results were obtained over a Mach number range from 10 to 20, an angle of attack range from 20° to 50°, and a Reynolds number range from

6 x 10^5 to 1 x10^4 based on model length; see Figure 3.1 and Table In addition, various elevon and body flap deflection angles were tested to determine control effectiveness. Though rudder and speed breaks were investigated, their effects were unmeasurable at a high angle of attack and, thus, were not included in this research.

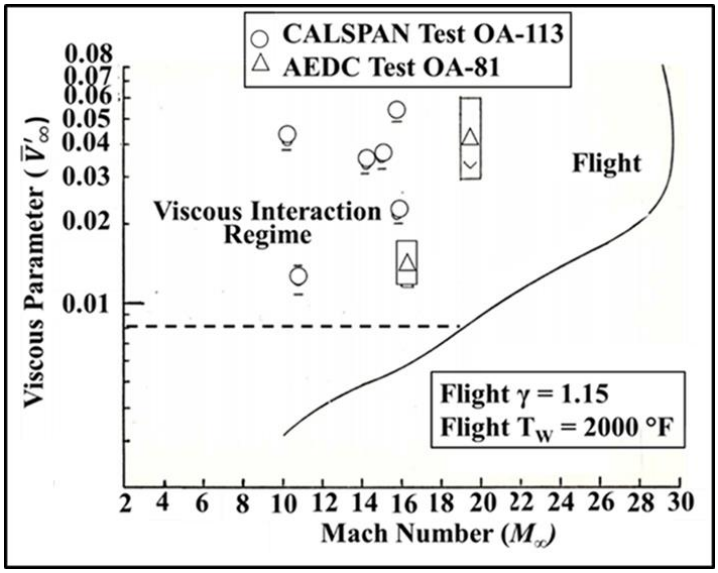

Figure 3.1 The 140 A/B Orbiter viscous parameter as a function of Mach number

Table 3.1 High Mach number/low Reynolds number test conditions in AEDC and CALSPAN

TEST CONDITIONS	M_∞	$Re_{\infty L}$ x 10^6	V'_∞
AEDC Tunnel F Test OA-81			
1	16	1.180	0.015
3	20	0.270	0.035
4	20	0.080	0.050
CALSPAN Shock Tunnel Test OA-113			
1	10.6	0.518	0.0125
2	9.8	0.035	0.0400
3	14.2	0.070	0.0365
4A	15.0	0.087	0.0360
5	15.9	0.043	0.0560
10A	15.65	0.266	0.0220

3.2 MODEL DESCRIPTION

Figure 3.2 shows the Orbiter key parameters, and Figure 3.3 provides the model descriptions used in AEDC Test OA-81 and CALSPAN Test OA-113.

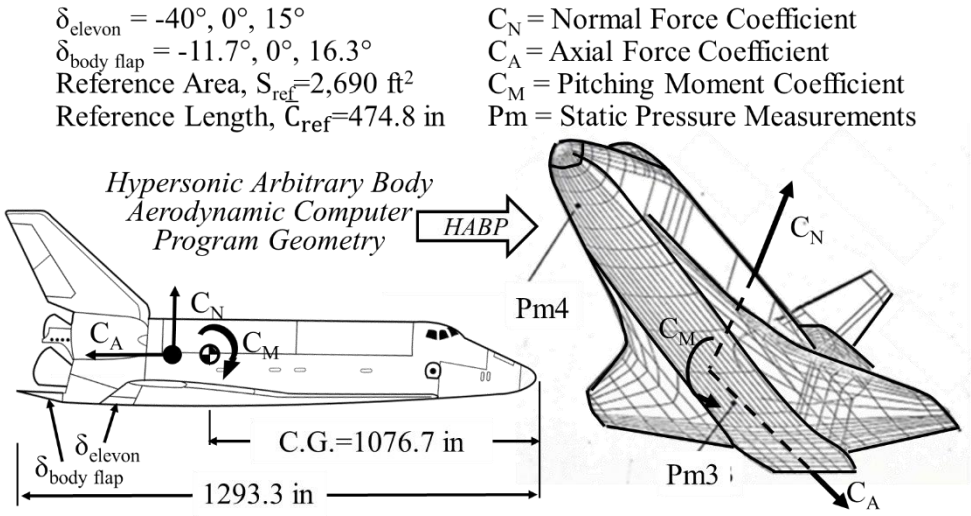

Figure 3.2 Orbiter key aerodynamic parameters and theoretical geometry configuration

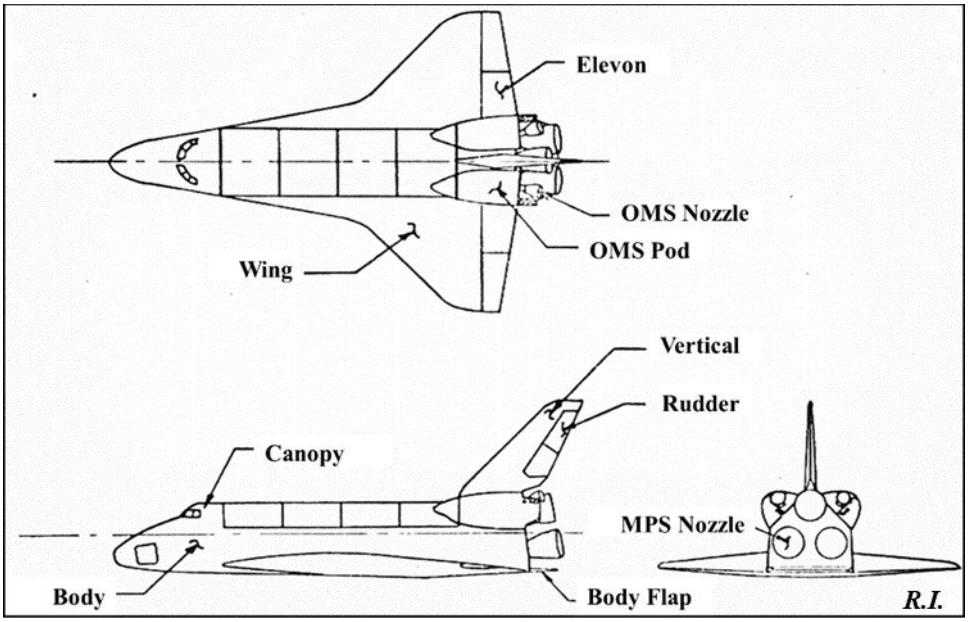

Figure 3.3 Orbiter model component description [15]

The AEDC VKF facility fabricated the model from a master provided by Rockwell International/Huntsville. The 0.01-scale 51-0 Model was constructed of magnesium, with every effort to keep the model weight to a minimum. The wings were equipped with positional elevons with the deflection angles changed by inserting angle plates machined to provide the desired angles. The elevon deflection angles used were -40°, 0°, 12.5°, and 15°, with the extremes representing the limits of elevon travel for the 140A/B configuration. Individual body flaps were machined to the proper deflection. Body flap angles were -11.7°, 0°, and 16.3°. The vertical stabilizer component had a fixed 0° rudder, and the speed brake was 55° for AEDC Test OA-81 and 0° for CALSPAN Test OA-113. The model attitude and control surface deflection descriptions are shown in Figure 3.4.

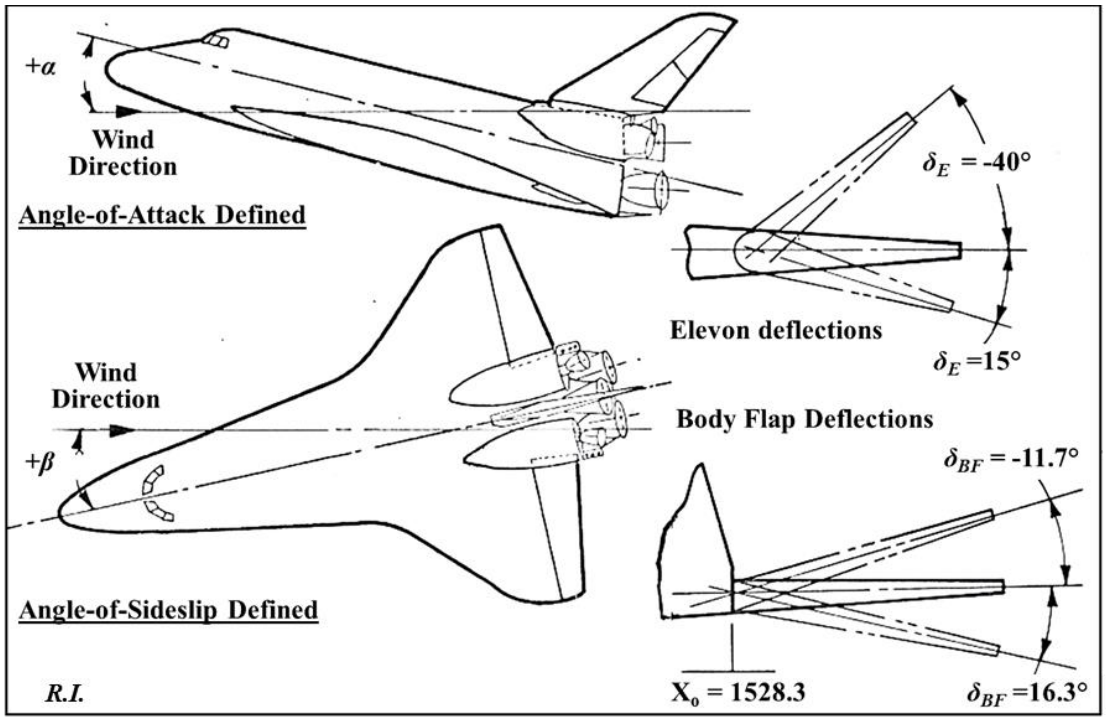

Figure 3.4 Orbiter model attitude and control surface description [15]

3.3 TEST FACILITY DESCRIPTION [16-20]

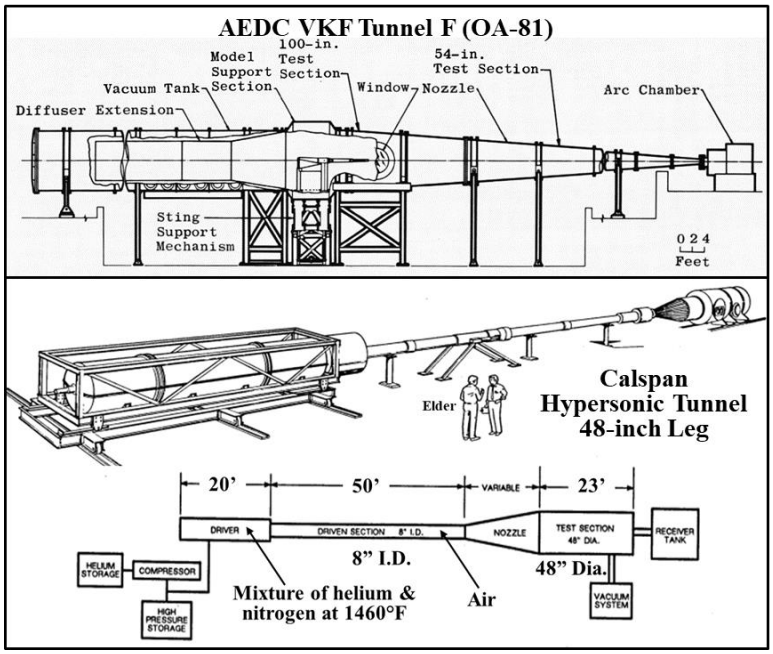

Figure 3.5 The two high Mach number/low Reynolds number tunnels

AEDC Test OA-81: The AEDC VKF Tunnel F is an arc-driven wind tunnel of the hotshot type capable of providing Mach numbers from 8 to 20. Test section diameters of 108 in diameter (M = 14 to 20) and 54 in (M = 10 to 17) are available using a 4° half-angle conical nozzle obtained using various throat diameters. Nitrogen is the test gas used for aerodynamic studies. The test gas is confined to either a 1.0-, 2.5- or 4.0-ft^3 arc chamber, which is heated and compressed by an electric arc discharge; increased pressure results in rupturing the diaphragm with the subsequent flow expansion through the nozzle. Test times are typically from 40 to 200 msec. Shadowgraph and Schlieren coverage is available.

CALSPAN Test OA-113: The CALSPAN 48-in tunnel employs a constant-area shock tube with an eight-inch inner diameter. The driver tube is 20 ft long and is externally heated by a resistance heater to temperatures of 1460 °F. The driven tube is 50 ft long.

The driver gas is generally a mixture of helium and nitrogen with a maximum helium purity of 100 percent, while the driven gas is generally air. Steady flow test times to permit accurate measurements of the various parameters of interest are achieved with the tailored interface technique. Three axisymmetric nozzles are available to expand the test gas from Mach 5.5 to 20.0. The contoured nozzle provides parallel flow with no pressure gradients in the streamwise direction for several feet. This is very important since the presence of a streamwise pressure gradient can have significant effects on model test results. The nozzles employ replaceable throat inserts of different diameters, so the test Mach number can vary with the particular nozzle. Test air passes downstream of the test section into a receiver tank of a size sufficient to maintain the desired flow for durations from 5 to 13 milliseconds. The test section has two 16-in diameter Schlieren windows mounted a short distance from the nozzle.

Because of both facilities' relatively short test times, the model wall temperature remains essentially invariant from the initial room temperature value.

3.4 INSTRUMENTATION DESCRIPTION [16-20]

AEDC Test OA-81: The aerodynamic forces were measured using a six-component force balance developed by AEDC VKF for hotshot-type tunnels. The balance load cells were instrumented with semiconductor strain gauges. Semiconductor accelerometers compensate for model inertia loads resulting from vibrations of the model and its support hardware. Base pressure measurements were made using Invar® pressure transducers ranging from 0.001 to 0.1 psi. They were mounted on the sting at the model's base with the gauge orifice pointing downstream and protruding approximately 1/16 in. aft the model base.

The arc chamber/test section pitot pressures and probe stagnation/cylindrical section heat transfer rates were monitored to determine tunnel flow conditions. The pitot pressures were measured with 15 psi, and strain gauge transducers were calibrated at the specific pressure level occurring during each test. The stagnation heat transfer rates used in determining the tunnel flow conditions were inferred from measurements made on the cylindrical sections of the two 1.0 in. diameter hemisphere cylinder probes, using ten mil resistance thermometer slug calorimeters. Coaxial thermocouple gauges located at the stagnation points of the probes were used as flow contamination monitors. The arc chamber reservoir pressure was measured using two strain gauge transducers, each having a full-scale calibrated range of 5000-, 10000-, and 25000-psi.

CALSPAN Test OA-113: The aerodynamic force measurement system consisted of the CALSPAN 1.312 in. diameter, a six-component "E" balance, and an accelerometer balance for inertial compensation. The "E" balance, mounted internally in Model 51-0, consists of six piezoelectric load cells mounted to a non-metric platform integral to the sting support. The accelerometer balance consisted of six accelerometers (i.e., equal in number to the number of force and moment components) whose locations were selected for maximum imposed acceleration (i.e., at the model extremities for pitch, roll, and yaw). An analog computer combined the signals from the balance of six force beams (three normal, two side, and one axial) and the accelerometer balance system to yield inertial compensated force beam output directly in forces and moments.

Pressure instrumentation consisted of five CALSPAN transducers mounted in the model. One measured balance cavity pressure, two measured lower wing surface pressures, and two measured lower fuselage centerline pressures.

The model, model cavity, and pitot pressures were measured by a system developed to meet the particular requirements of shock tunnel testing. The pressure transducers employ piezoelectric crystals, and their small size permits installation within the model. The transducers have a dual-element feature that reduces acceleration effects to an indicated pressure of 0.00015 psi/g. These transducers can accurately measure pressures as low as 0.001 psi. Proper shielding of the elements precludes temperature effects in the short test time.

3.4.1 Test Conditions [16-20]

AEDC Test OA-8: Computations for freestream test conditions consisted of using the timewise measurements of the test section pitot pressure and hemisphere cylinder shoulder heat transfer rates, inferred to stagnation, with the Fay-Riddle stagnation point heat transfer theory to compute the reservoir enthalpy. The test section freestream conditions were calculated, assuming quasi-steady isentropic flow, from the resulting total enthalpy combined with measured reservoir and pitot pressures. The uncertainties in the pressure data are estimated to be $\pm$4 percent for the pitot and $\pm$5 percent for the reservoir, based on an average of two measurements. The transfer rate uncertainty is $\pm$5 percent based on an average of four measurements. Using the Taylor error propagation method, these values were used to estimate uncertainties in the tunnel flow parameters. Accordingly, the determination of freestream static pressure is considered accurate to within $\pm$6 percent and freestream Mach number to within $\pm$1.5 percent.

CALSPAN Test OA-113: The stagnation enthalpy and the test section freestream conditions were calculated using the thermodynamic properties of real gas, the incident shock wave velocity, and the nozzle supply pressure. The speed of the incident shock wave

was measured to be within ±1 percent. Based on the agreement of pressure transducers, the nozzle supply pressure is considered accurate to be within ±3.5 percent. The dynamic pressure was determined from a linear correlation of measured model pressures and forces. The most probable error in the dynamic pressure is calculated as ±5.8 percent. The test section Mach number, dependent on the ratios of pitot-to-reservoir and dynamic pressure-to-reservoir pressures, is estimated to be accurate to ±2 percent.

3.4.2 Data Precision Description [16-20]

NOTE: *The following data precision description is based on what the test facilities provided pretest. However, the extensive data scatter obtained during the tests implies that the facility estimations must be suspect. Detailed explanations are provided in Chapter 4 and Appendix A and B.*

AEDC Test OA-81: The uncertainties in calculated force data were estimated using the Taylor error propagation method combined with the uncertainties in each measurement occurring in the calculations. In general, it is estimated that for nominal loads, the uncertainty in the force measurements is ±6 percent for each balance component. This uncertainty includes calibration linearity and repeatability, instrumentation system error, and errors introduced by dynamic effects resulting from the impulsive operating nature of the facility. The uncertainty of ±6 percent of each balance component measurement, combined with a ±4 percent in the dynamic pressure, gives an uncertainty in the normal force coefficient of ±6 percent. This uncertainty in the normal force coefficient applies to both the Mach 16 and Mach 20 data.

An uncertainty of ±6 percent of the measured axial force coefficient for Mach 16 data and ±15 percent for the Mach 20 data, combined with the ±4 percent uncertainty in dynamic pressure, gives an uncertainty of ±7 and ±16 percent data, respectively. The more considerable uncertainty for the Mach 20 data reflects the additional uncertainty resulting from flow contamination.

The Taylor error propagation method determined the absolute uncertainties in the pitching moment and center-of-pressure location. The absolute uncertainty in the pitching moment coefficient depends on the angle of attack because of the variation in the normal force coefficient with the angle of attack. The absolute uncertainty in center-of-pressure is a constant for all conditions. These uncertainties are listed in Table 3.2 and apply to both Mach 16 and Mach 20 data. The uncertainties are primarily a function of the normal force component measurements and the axial force component of a minor influence.

Table 3.2 Pitching moment and center-of-pressure uncertainties

MACH 16 and Mach 20 Test Conditions		
Absolute Uncertainties		
α (degrees)	**C_M**	**X_{CP}/L**
20	**±0.0088**	**±0.0076**
30	**±0.0163**	**±0.0076**

The model attitude was set before each run. The pitch and roll angles are estimated to be accurate within ±0.10 degrees. The estimated uncertainties for the model base pressure measurements are ±10 percent.

CALSPAN Test OA-113: Based on calibration repeatability and the consistency/repeatability of the pressure data, it is estimated that pressure data have a most probable error of ±5 percent.

Force coefficient uncertainties arise from dynamic pressure, reference area, and balance load errors. If one assumes a negligible error in the reference area, then the overall accuracy of the force data is a knowledge of the precision of measuring the balance. However, on the balanced output, there is an incremental error based on the capability of the balance to read a given load. This type of uncertainty is independent of the angle of attack. The incremental errors are obtained by calculating the standard deviation between applied and calculated calibration loads. The calculated loads were determined using the calibration constants and the balance output data produced by the applied loads. The results are presented in Table 3.3.

Table 3.3 Incremental errors between applied and calculated calibration loads

Components	3-Sigma
Normal Force	±0.696 pounds
Axial Force	±0.198 pounds
Side Force	±2.325 pounds
Pitching Moment	±1.254 inch-pounds
Yawing Moment	±2.010 inch-pounds
Rolling Moment	±0.198 inch-pounds

NEXT CHAPTER DESCRIPTION

The next chapter, Chapter 4, describes the AEDC Tunnel F and CALSPAN 48-in tunnels' poor quality data that required "significant corrections" to salvage their usefulness.

The causes included contaminated flow by copper, tungsten, and beryllium dust particles; incorrect dynamic pressure measurements; misalignment of nozzle parts; nozzle non-uniformities; source flow; and flow irregularities. A rigorous effort was thus made to correlate the hypersonic viscous interaction aerodynamic data obtained on the 0.01-scale (51-0) 140A/B model from AEDC Test OA-81 and CALSPAN Test OA-113. Chapter 4 describes the magnitude of how defectively the data measurements were, provides examples of corrected wind tunnel aerodynamic data, and shows how the data was faired to obtain the res—Appendixes A and B detail how the correction methodologies were developed and used to correct the data.

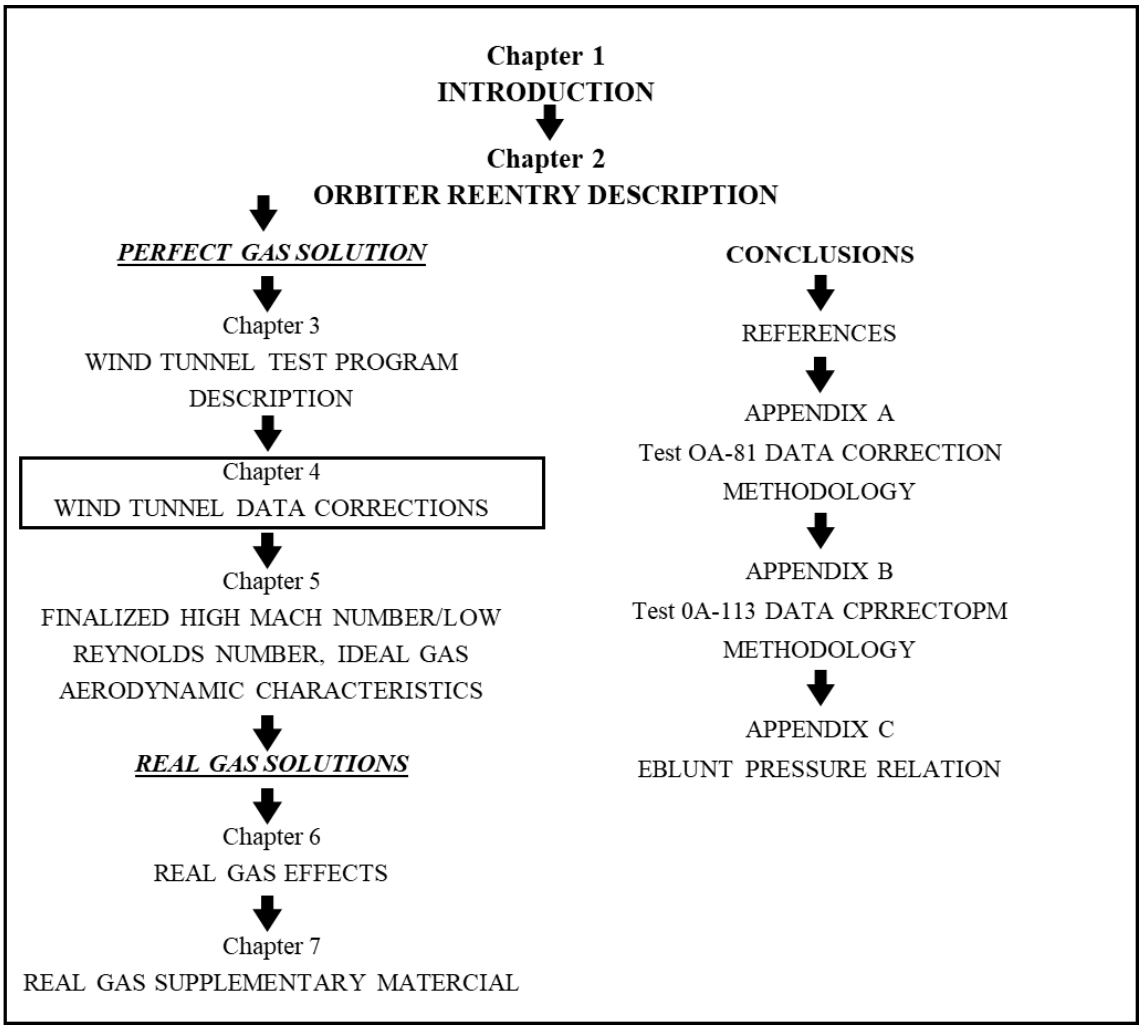

CHAPTER 4

WIND TUNNEL DATA CORRECTIONS

A rigorous effort was made to correlate the hypersonic viscous interaction aerodynamic data obtained on the 0.01-scale (51-0) 140A/B model from AEDC Test OA-81 and CALSPAN Test OA-113; Figure 4.1.

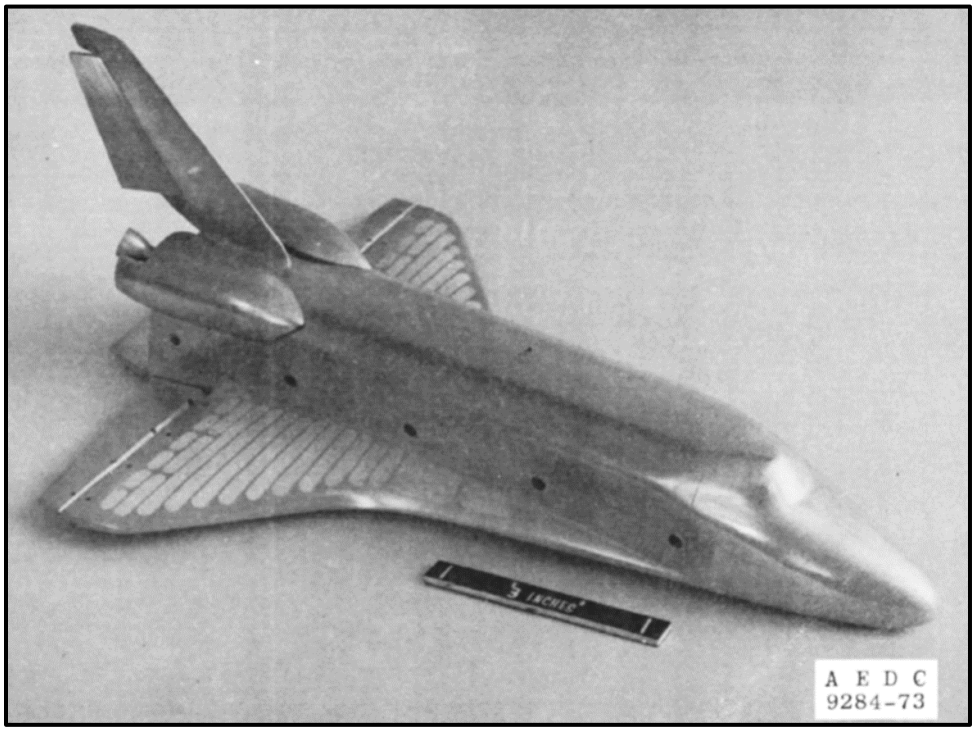

Figure 4.1 0.01-scale (51-0) 140A/B Orbiter model

The test results were obtained over an angle of attack range from 20° to 50° for a Mach number range from 10 to 20. Based on model length, a Reynolds number range from

$6x10^5$ to $1x10^4$ was investigated to determine high Mach number/low Reynolds number aerodynamics (i.e., perfect gas viscous interaction effects). Various elevon and body flap deflection angles were tested to determine control effectiveness. Note that a second entry into the AEDC Tunnel F facility (AEDC Test OA-160) was conducted to substantiate AEDC Test OA-81 and CALSPAN Test OA-113 data. Still, it played only a minor role in the analyses.

Table 4.1 provides the reference dimensions for the aerodynamic coefficients obtained from AEDC Test OA-77, OA-78, OA-81, OA-160, and CALSPAN Test OA-113.

Table 4.1 Orbiter reference dimensions

Reference Area, $S_{ref} = C_w$	**2,690 ft^2**
Reference Length, $\bar{C}_{ref}$	**474.8 in**
Vehicle Length, L_B	**1,290 in**

Flow anomalies influenced the inaccuracies of the test data. Detailed investigations were performed to determine the cause and effects of these flow anomalies. This resulted in the need to make significant adjustments to the measured data to compensate for the data uncertainties and to salvage their usefulness:

- AEDC VKF Tunnel F's (Test OA-81) flowfield was contaminated by fine dust particles produced by the vaporization of small amounts of copper, tungsten, and beryllium during electrical discharge in the tunnel's arc chamber. In addition, source flow and flow non-uniformities in the nozzle further contributed to the poor data quality. A joint and cooperative effort with VKF engineers developed two methods to correct the data—one by this researcher and one by VKF engineers.

Figure 4.2 shows an example of the difference between corrected and uncorrected data. Appendix A provides the details of how the data was corrected.

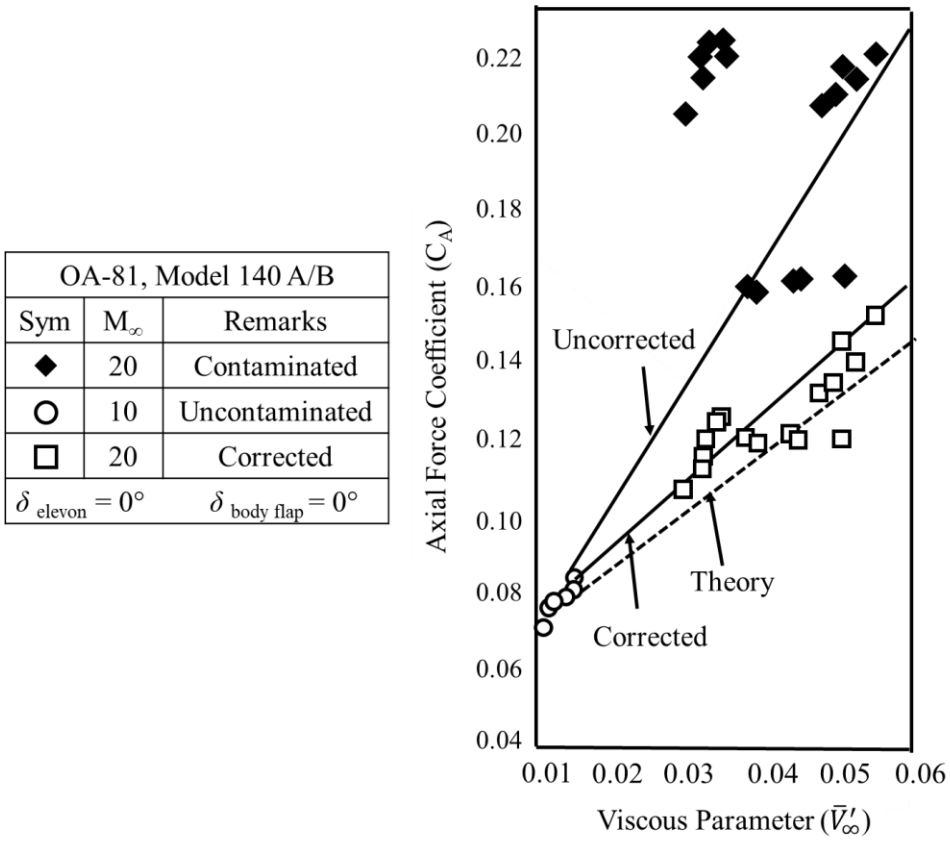

Figure 4.2 Comparison of uncorrected and corrected AEDC test data

- The CALSPAN (Test OA-113) pitot probe—used to measure dynamic pressure in the 48-inch shock tunnel to compute aerodynamic force and moment coefficients—was mounted too far from the model and close to the tunnel boundary layer to provide reliable values of dynamic pressure. It was also believed that improper alignment of parts in the nozzle and irregularities downstream of the throat contributed to larger-than-normal errors. A solo effort by this researcher developed a method to correct the data. Figure 4.3 shows an example of the

difference between corrected and uncorrected data. Appendix B provides the details of how the data was corrected.

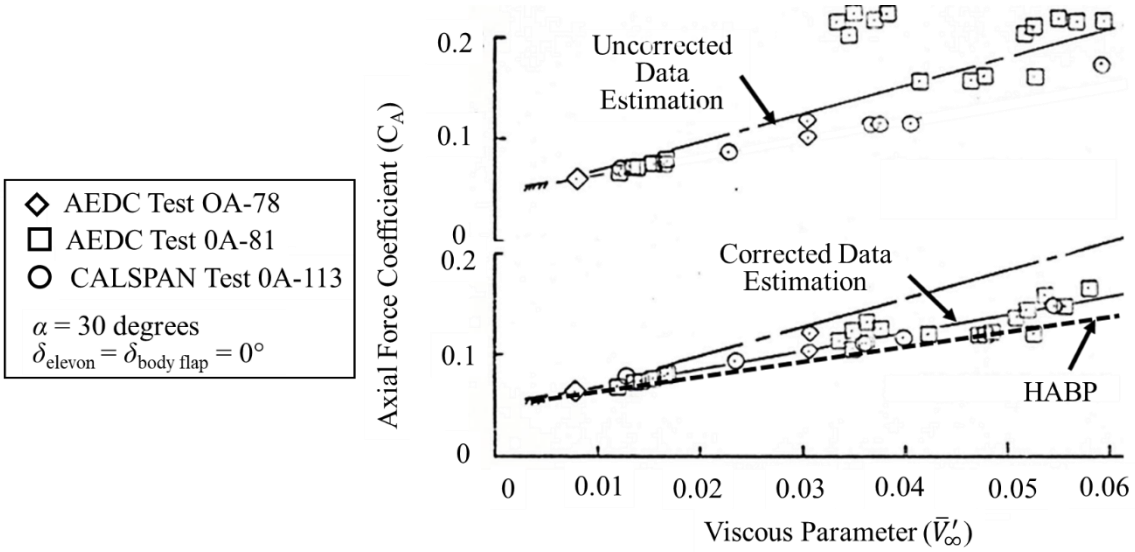

Figure 4.3 Comparison of uncorrected and corrected AEDC and CALSPAN data

Since axial force is the primary parameter in determining the presence of the viscous interaction regime, Figure 4.3 shows the problem confronted in determining realistic values as a function of the viscous parameter. It can be seen that a significant difference (i.e., greater than 25 percent) exists between the two sets before corrections. The large scatter due to AEDC Test OA-81 contamination is noticeable compared to CALSPAN Test OA-113. However, the two data sets collapsed together after the adjustments were applied. Furthermore, after the adjustments are used, the difference between the two data sets is less than $\pm$8 percent which is inside the quoted $\pm$15 percent uncertainty of the AEDC Test OA-81 before testing. This fact holds for both the CALSPAN Test OA-113 unadjusted or adjusted data. The results from both CALSPAN Test OA-113 unadjusted and adjusted data substantiate the AEDC Test OA-81 corrected axial force data and confirmed the scheme developed for correcting the contaminated flow.

It can also be seen from Figure 4.2 that the contamination scheme used in AEDC Test OA-81 changes both the magnitudes and trends of the axial force data. On the other hand, no fundamental change to the data trends is made with the correction scheme in CALSPAN Test OA-113, as shown in Figure 4.3. Instead, a collapsing of the data scatter is achieved. Hence, it must be stressed that utilizing the correction scheme for CALSPAN Test OA-113 did not tamper with the final data trends and results. Because of this, a higher degree of confidence was placed on the OA-113 data over that of the AEDC OA-81 data, which required significant magnitude and trend changes.

Developing the correction factors, applying them to the measured aerodynamic characteristics, replotting the data, and getting approval from NASA and RI impacted the test completion schedule by over 1-1/2 years.

4.1 EXAMPLES OF CORRECTED WIND TUNNEL AERODYNAMIC DATA

The following four examples (Figures 4.4 through 4.7) show an overview of the rigorous effort to correct the aerodynamic test data as a function of Mach number, viscous parameter, and angle of attack for zero control surface deflections. Appendices A and B show the correction methods developed to salvage facility data. The coefficient data are referenced to the body axis system, and the pitching moment coefficient data are given for the forward center-of-gravity location based on body length, $X_{C.G.}/L = 0.65$.

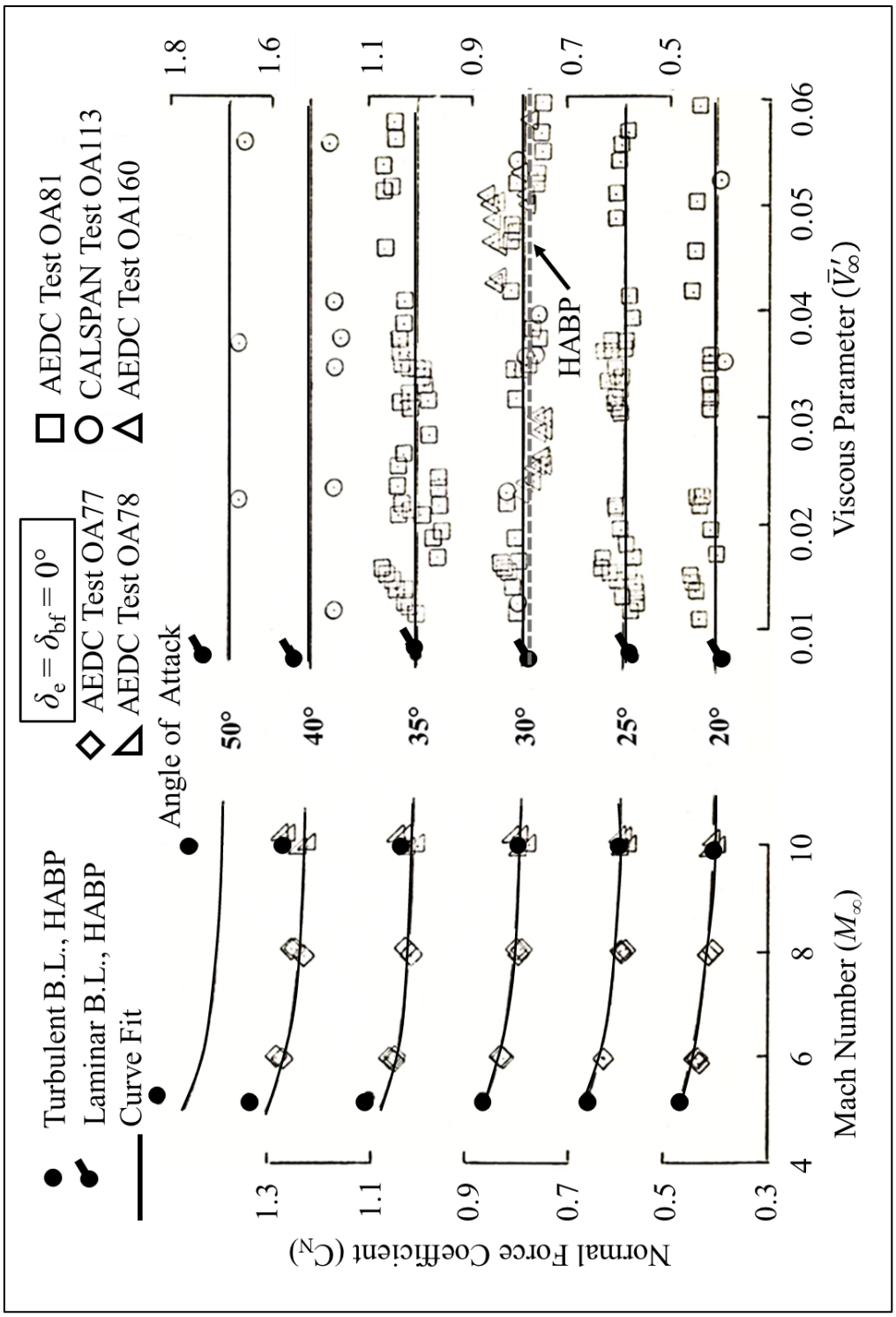

Figure 4.4 Normal force coefficient as a function of M_∞ and $\bar{V}'_\infty$ ($\delta_{BF} = \delta_E = 0°$)

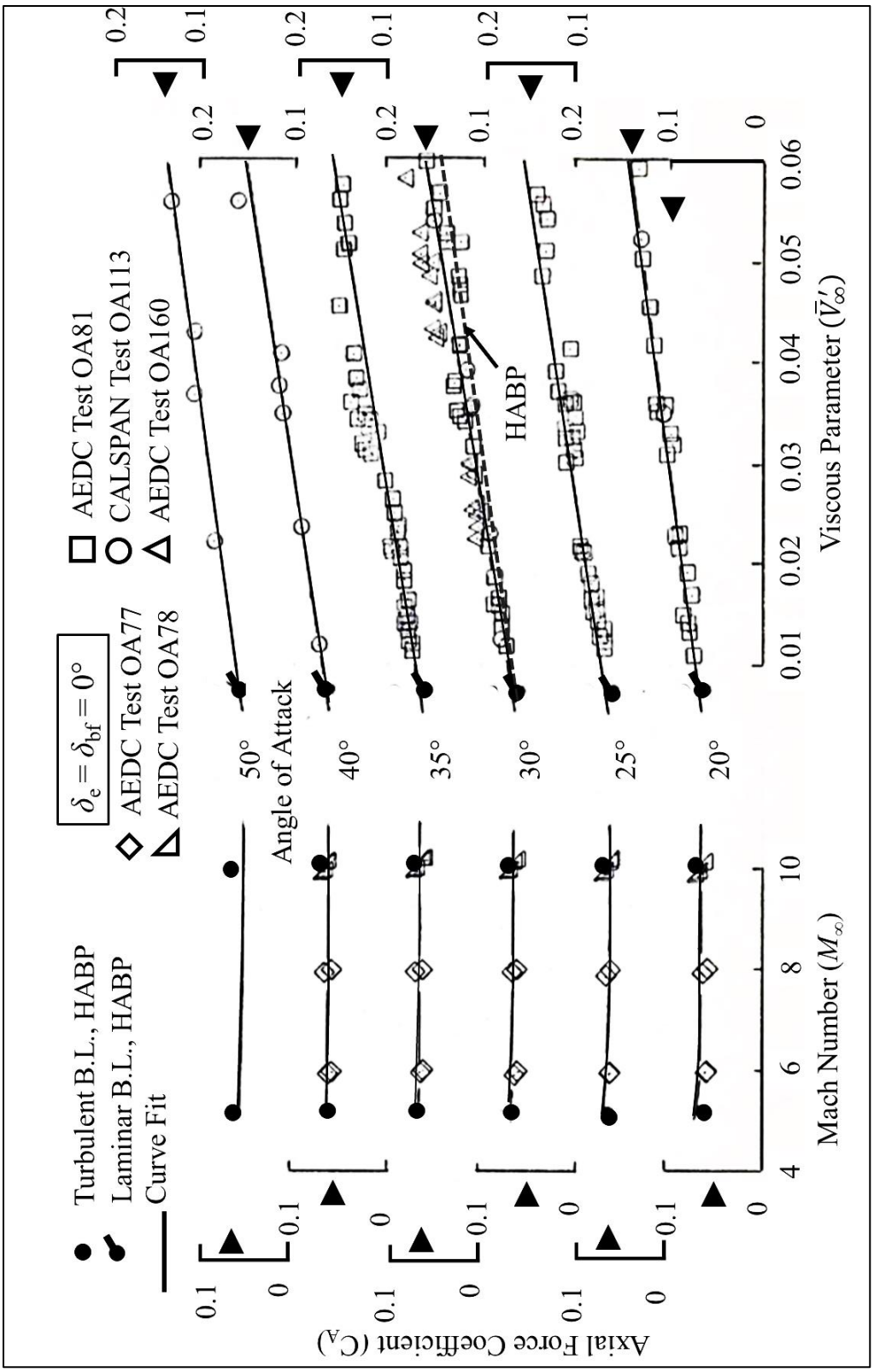

Figure 4.5 Axial force coefficient as a function of M_∞ and $\bar{V}'_\infty$ ($\delta_{BF} = \delta_E = 0°$)

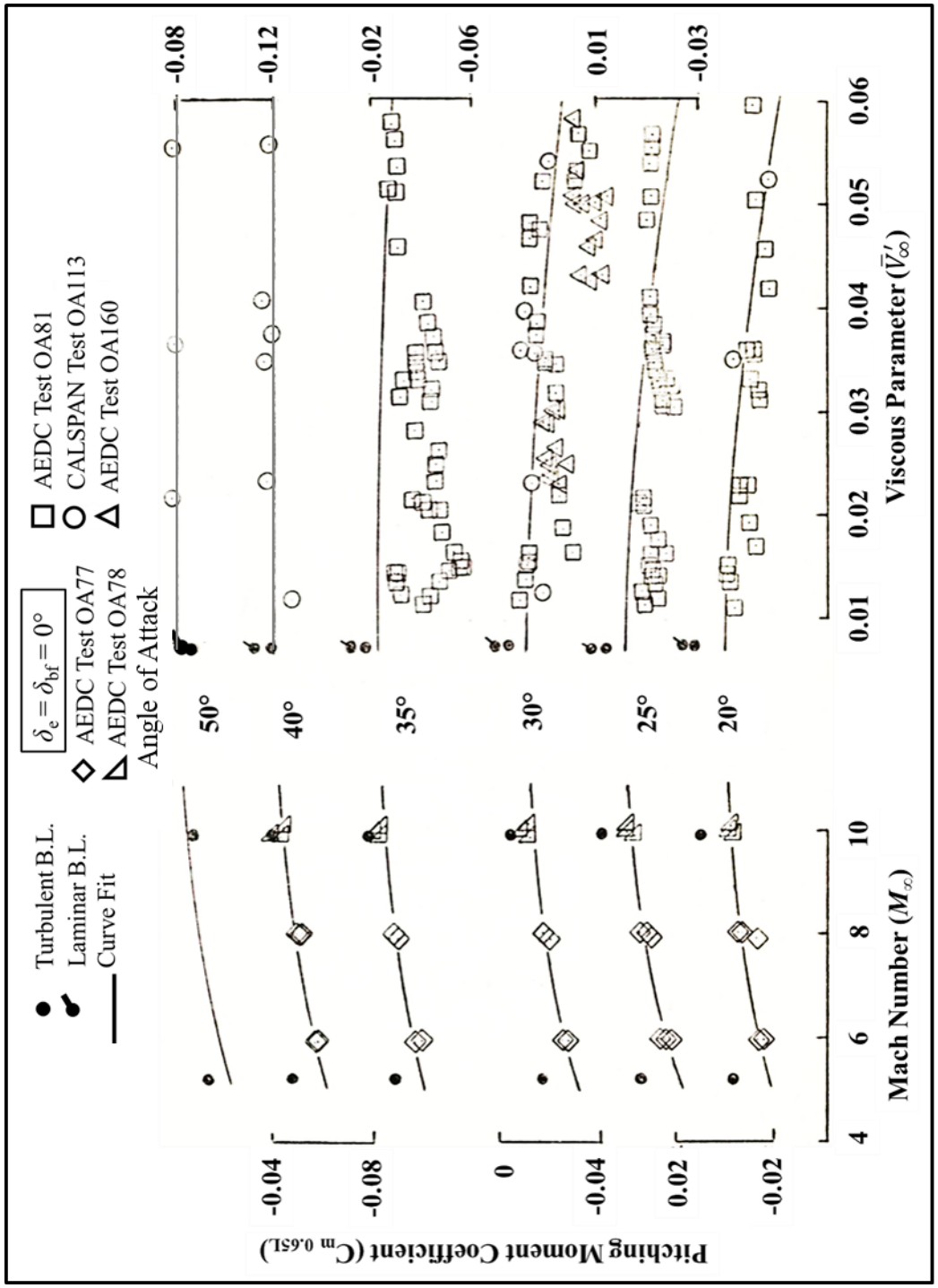

Figure 4.6 Pitching moment coefficient as a function of M_∞ and $\bar{V}'_\infty$($\delta_{BF} = \delta_E = 0°$)

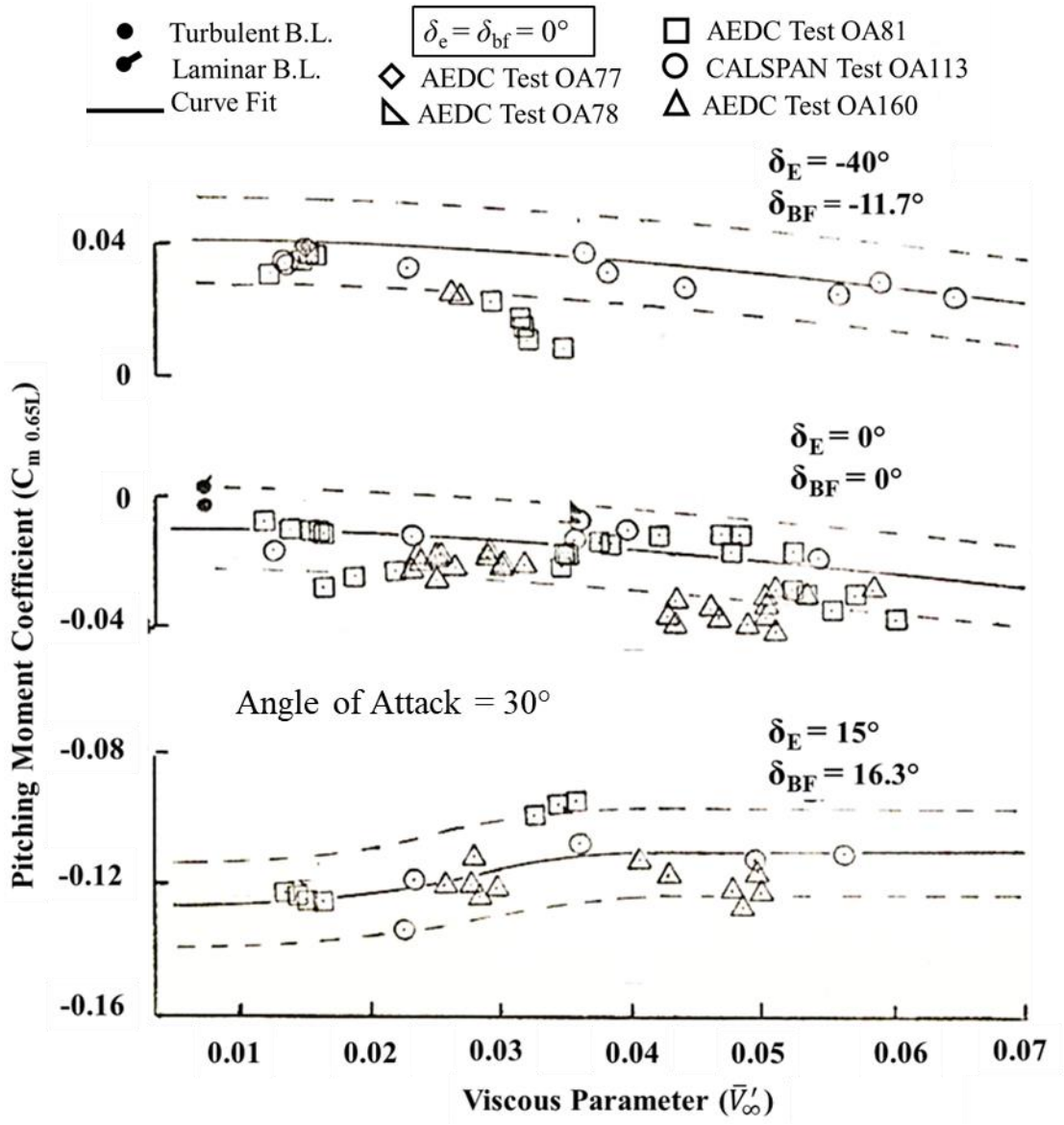

Figure 4.7 Control surface effectiveness as a function of $\bar{V}'_\infty$

The body flap and elevon control effectiveness at maximum positive and negative deflection, as shown in Figure 4.7, is the maximum the Orbiter can change its attitude in pitch. The theory agrees well with the corrected wind tunnel measurement for normal and axial forces and somewhat agrees with the pitching moment.

4.2 EXAMPLES OF WIND TUNNEL AERODYNAMIC DATA FAIRING

- Figures 4.8 through 4.10 present corrected longitudinal normal force, axial force and pitching moment coefficients, and center-of-pressure locations as a function of the viscous parameter, angle of attack of 30°, 40°, and 50°, and a control surface deflection of 0°. Most of the data were obtained at a 30° angle of attack. The more recent AEDC Test OA-160 data tends to be on the high side of the mean, whereas the AEDC Test OA-81 is on the low side. A similar trend exists for the pitching moment data. The fairing through the data tends to favor the CALSPAN Test OA-113 data. The angle of attack of 20°, 25°, and 35° are provided in Chapter 5.

- Figures 4.11 through 4.13 present corrected longitudinal normal force, axial force, pitching moment coefficients, and center-of-pressure location as a function of the viscous parameter, angles of attack of 30°, 40°, and 50°, body flap deflection of -11.7° and elevon deflection of -40°. The data for this configuration is predominately CALSPAN Test OA-113. The incremental viscous interaction effects equal the zero degrees control surface deflection configuration (Figures 4.1 through 4.3). The angle of attack of 20°, 25°, and 35° are provided in Chapter 5.

- Figures 4.14 through 4.16 present corrected longitudinal normal force, axial force and pitching moment coefficients, and center-of-pressure location as a function of the viscous parameter, angle of attack of 30°, 40°, and 50°, body flap deflection of 16.3°, and an elevon deflection 15°. Though the pitching moment data scatter is significant, the CALSPAN Test OA-113 data tends to lay along the mean of the data. The center-of-pressure travel displays an unusual trend in that it moves forward as predicted but then levels out and remains constant with increasing

viscous parameter. This may suggest that a laminar boundary layer separation region has been established and then stabilizes to become independent of the viscous parameter. Verifying perfect gas center-of-pressure travel is dependent on real gas estimates. Angles of attack of 20°, 25°, and 35° are provided in Chapter 5.

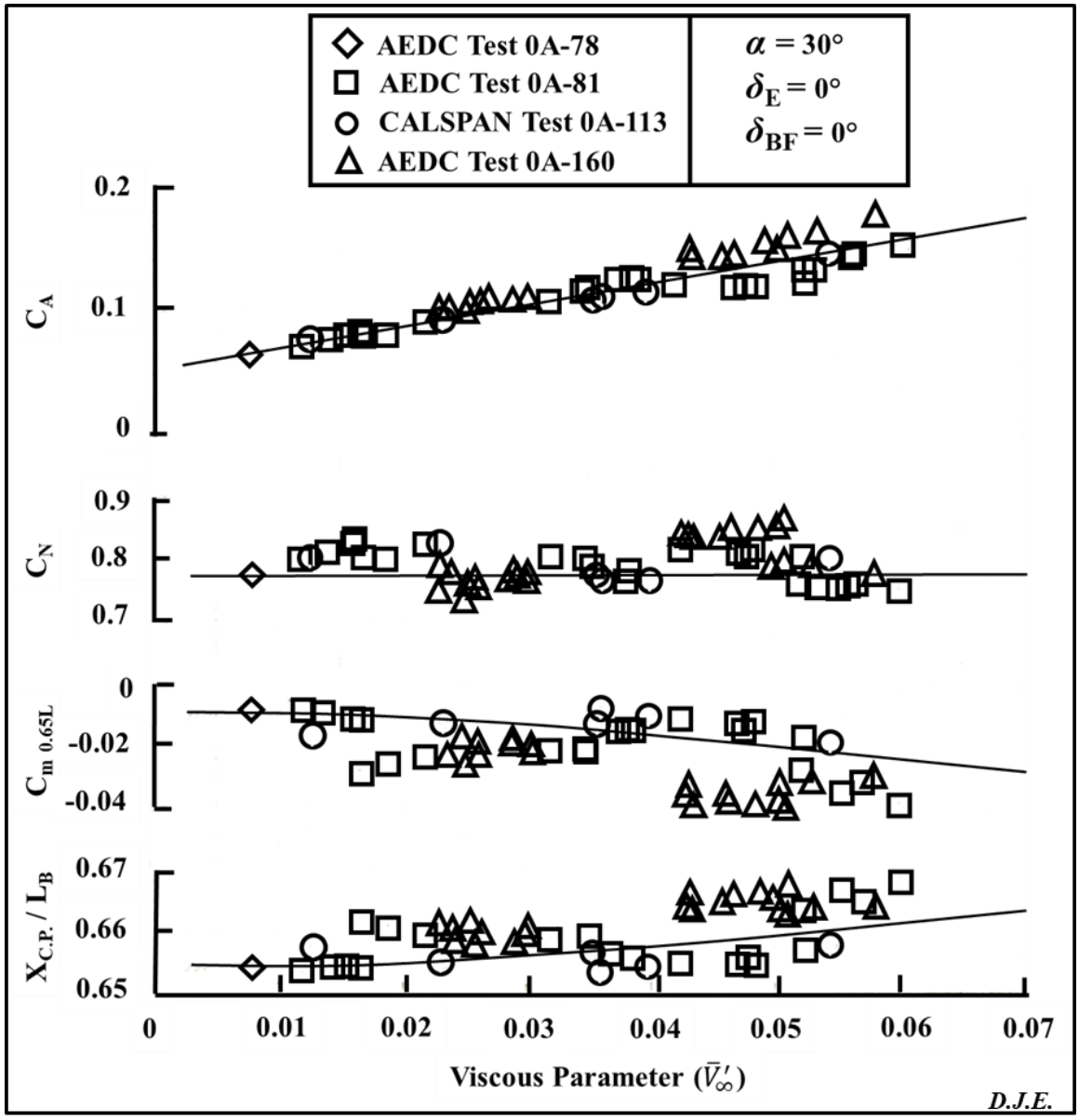

Figure 4.8 Corrected wind tunnel longitudinal aerodynamic coefficients as a function of $\bar{V}'_\infty$ ($\alpha = 30°$, $\delta_{BF} = 0°$, $\delta_E = 0°$)

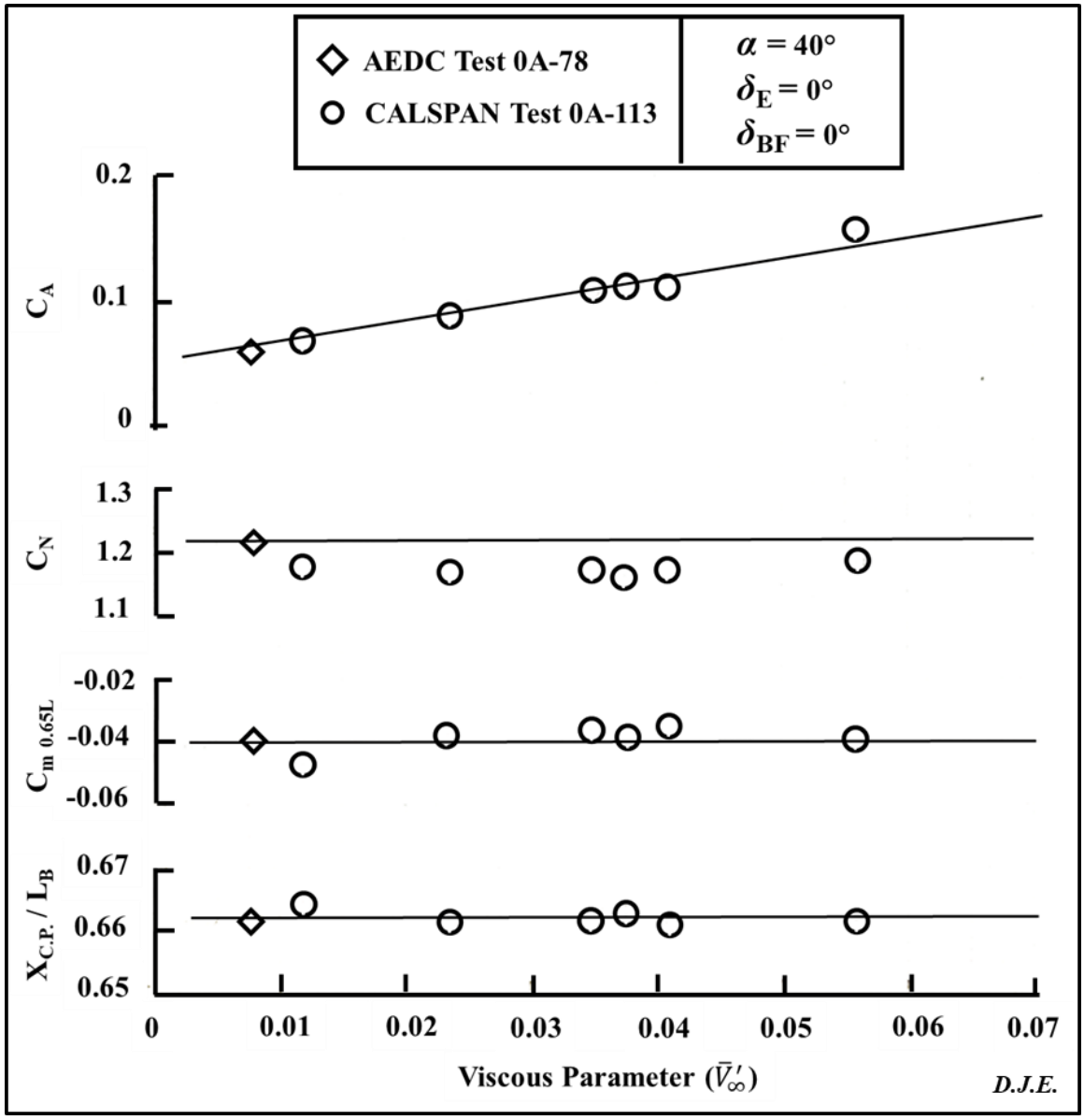

Figure 4.9 Corrected wind tunnel longitudinal aerodynamic coefficients as a function of $\bar{V}'_\infty$ ($\alpha = 40°$, $\delta_{BF} = 0°$, $\delta_E = 0°$)

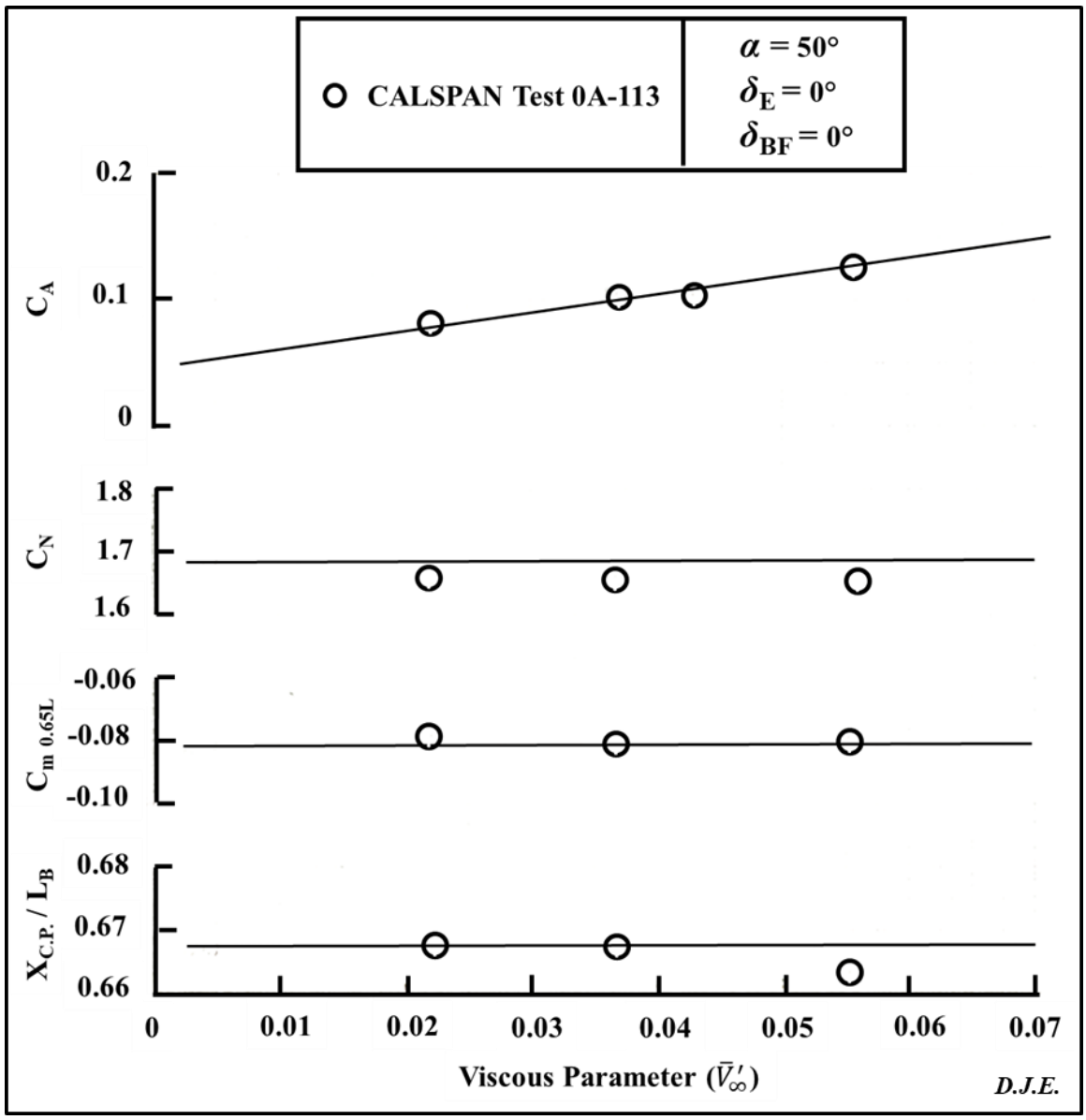

Figure 4.10 Corrected wind tunnel longitudinal aerodynamic coefficients as a function of $\bar{V}'_\infty$ ($\alpha = 50°$, $\delta_{BF} = 0°$, $\delta_E = 0°$)

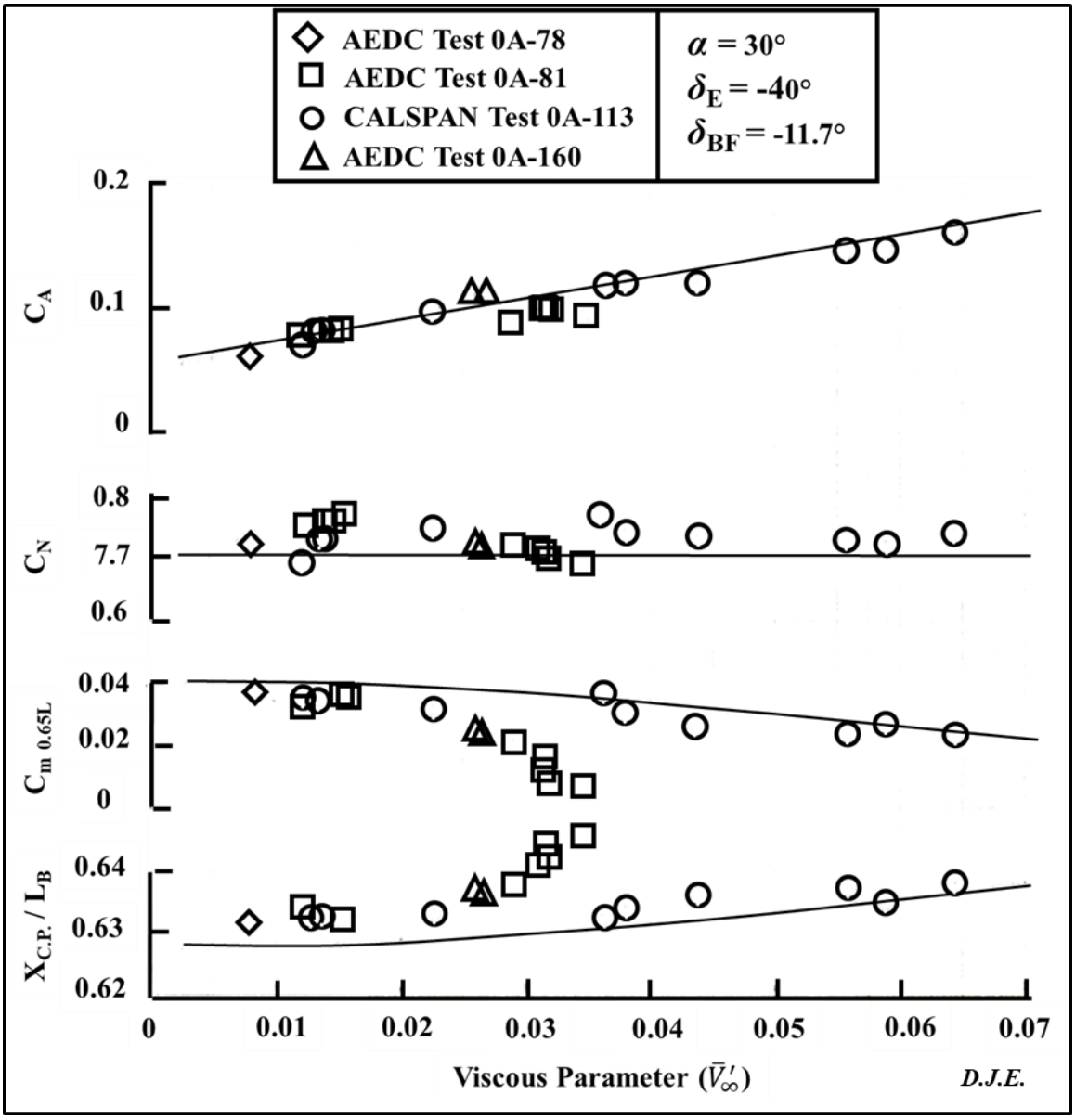

Figure 4.11 Corrected wind tunnel longitudinal aerodynamic coefficients as a function of $\bar{V}'_\infty$ ($\alpha = 30°$, $\delta_{BF} = -11.7°$, $\delta_E = -40°$)

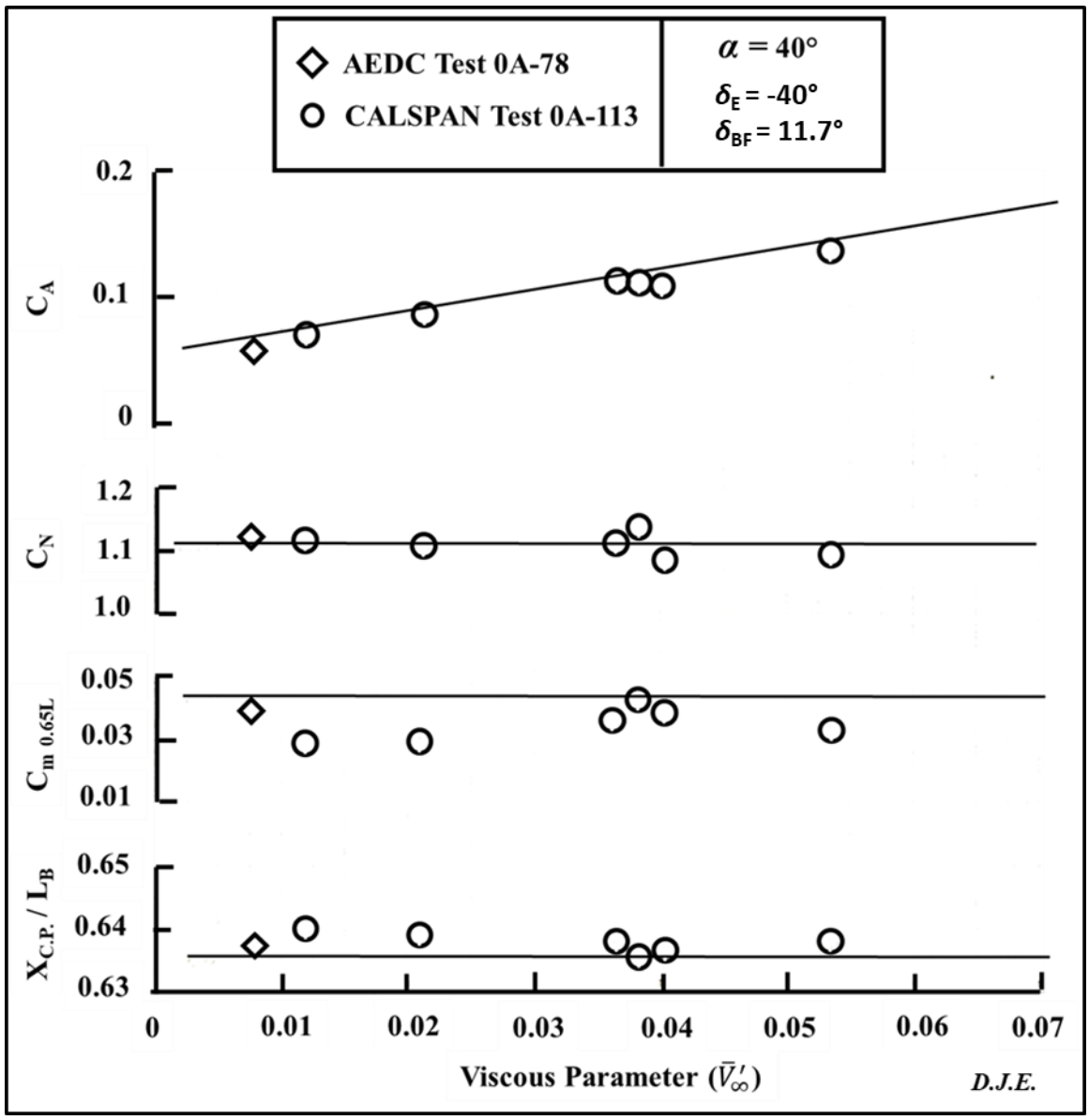

Figure 4.12 Corrected wind tunnel longitudinal aerodynamic coefficients as a function of $\bar{V}'_\infty$ ($\alpha = 40°$, $\delta_{BF} = -11.7°$, $\delta_E = -40°$)

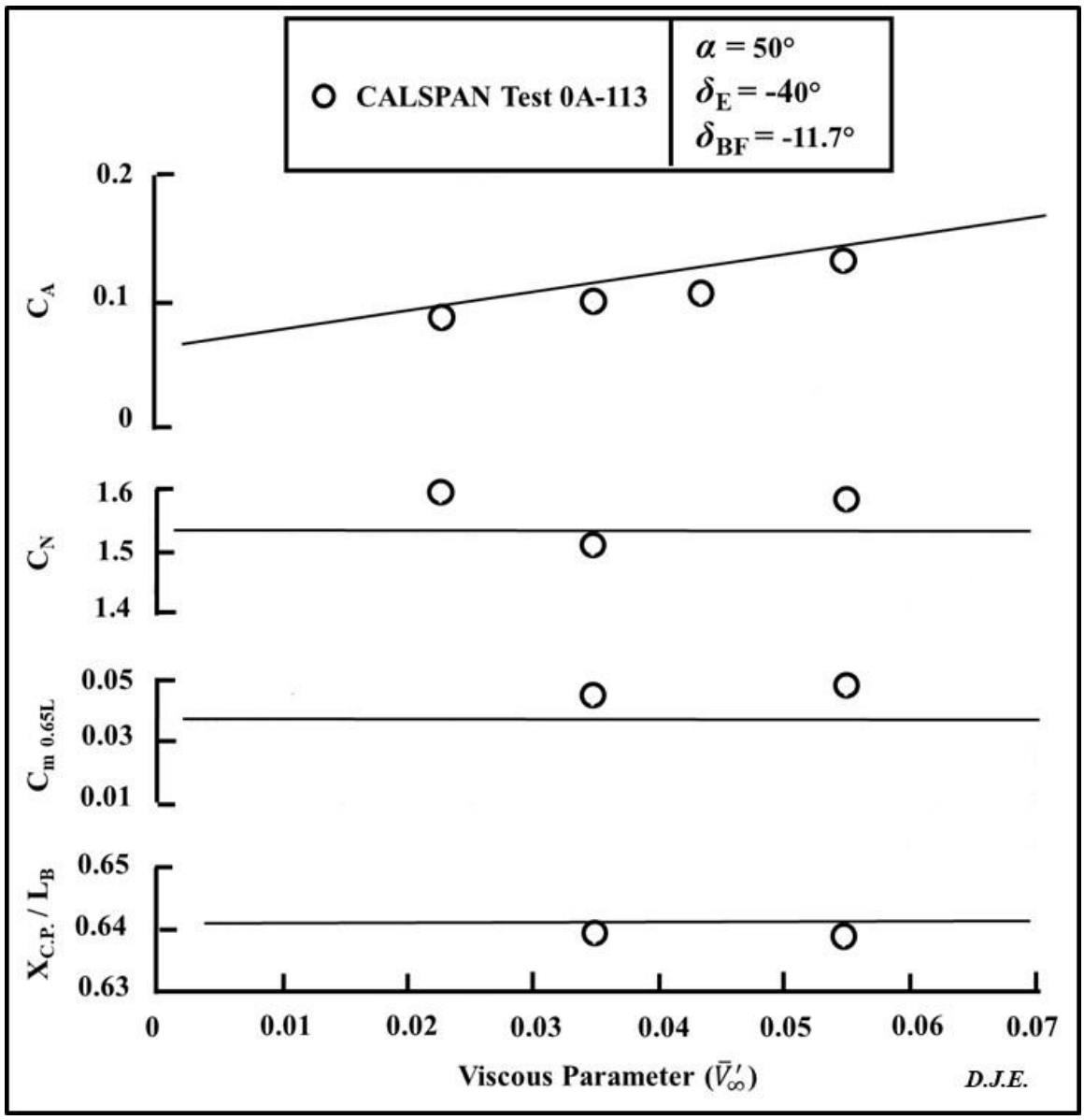

Figure 4.13 Corrected wind tunnel longitudinal aerodynamic coefficients as a function of $\bar{V}'_\infty$ ($\alpha = 50°$, $\delta_{BF} = -11.7°$, $\delta_E = -40°$)

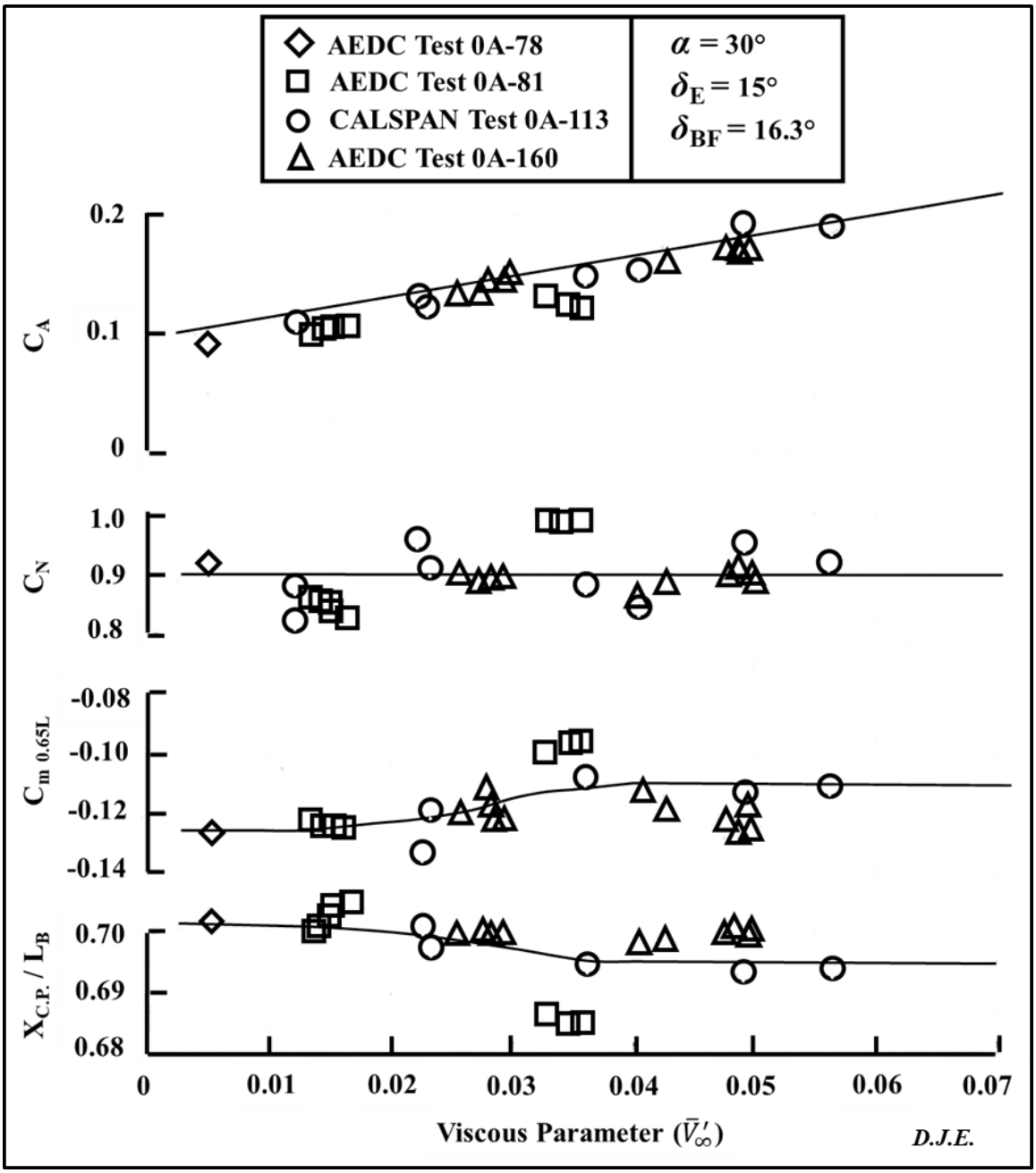

Figure 4.14 Corrected wind tunnel longitudinal aerodynamic coefficients as a function of $\bar{V}'_\infty$ ($\alpha = 30°$, $\delta_{BF} = 16.3°$, $\delta_E = 15°$)

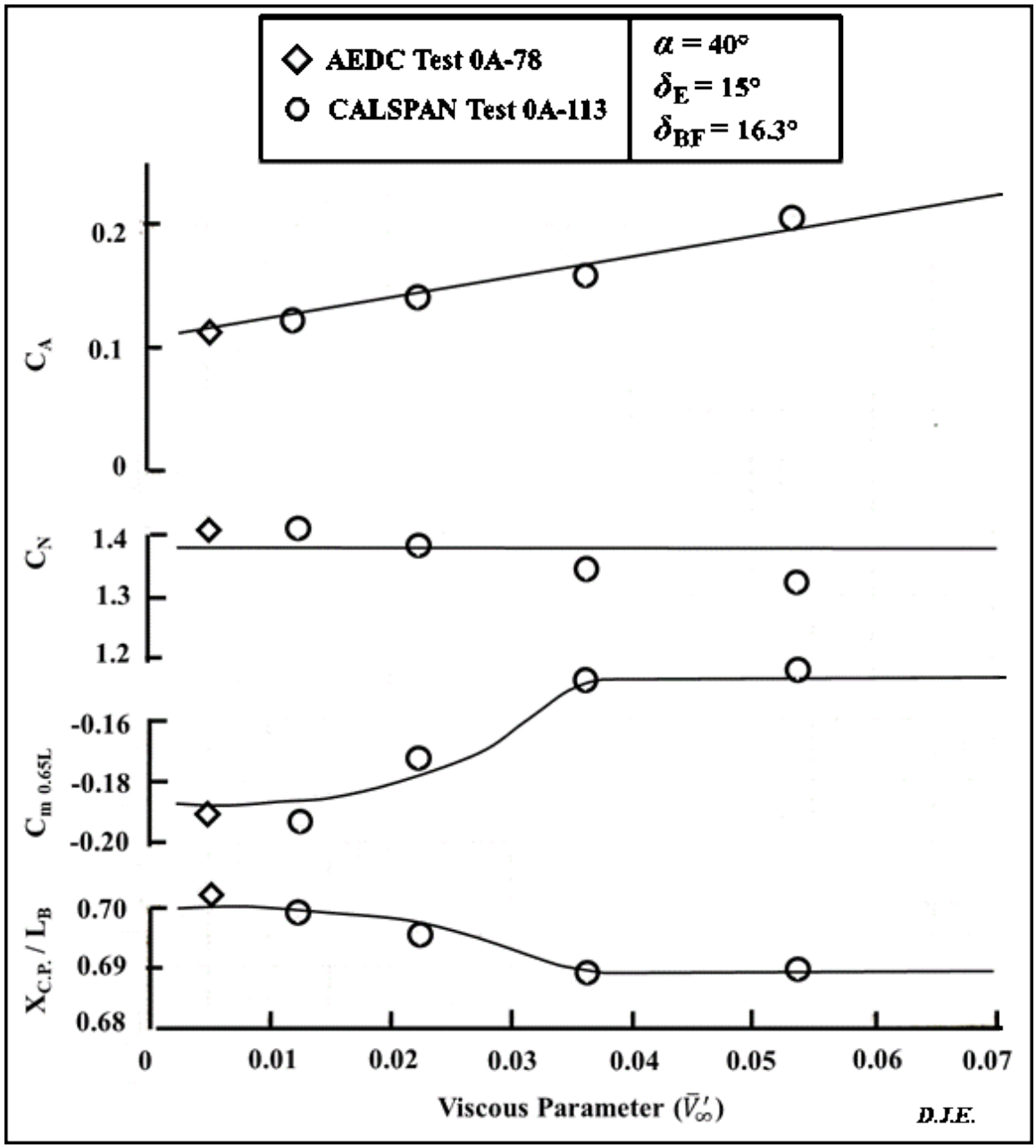

Figure 4.15 Corrected wind tunnel longitudinal aerodynamic coefficients as a function of $\bar{V}'_\infty$ ($\alpha = 40°$, $\delta_{BF} = 16.3°$, $\delta_E = 15°$)

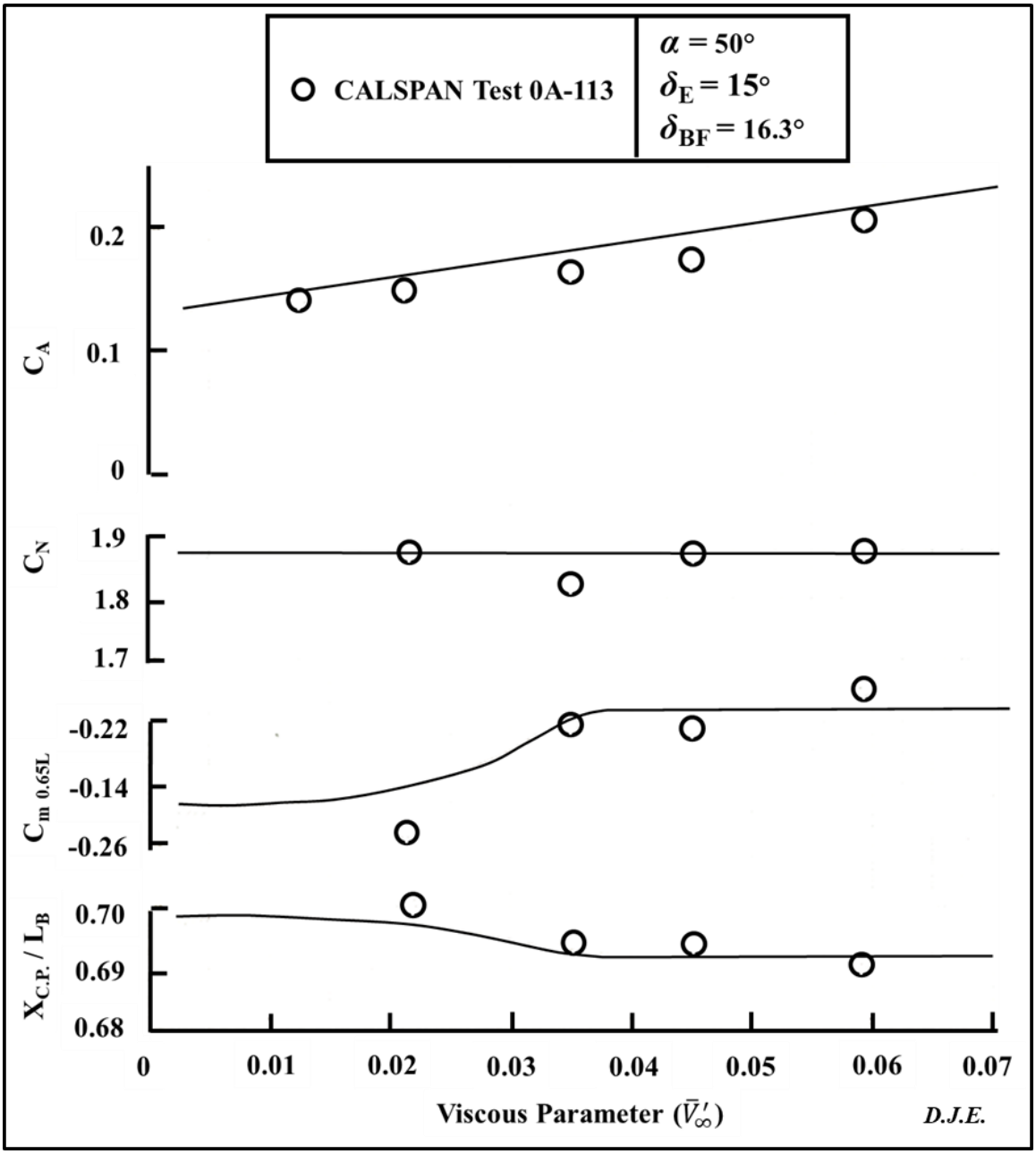

Figure 4.16 Corrected wind tunnel longitudinal aerodynamic coefficients as a function of $\bar{V}'_\infty$ ($\alpha = 50°$, $\delta_{BF} = 16.3°$, $\delta_E = 15°$)

NEXT CHAPTER DESCRIPTION

The next chapter, Chapter 5, provides the finalized perfect gas aerodynamic characteristics, which Rockwell International/Space Division distributed in their

"Aerodynamic Design Data Book, Orbiter Vehicle – Volume 1" [15]. Real gas effects on the Orbiter are presented later in Chapter 6.

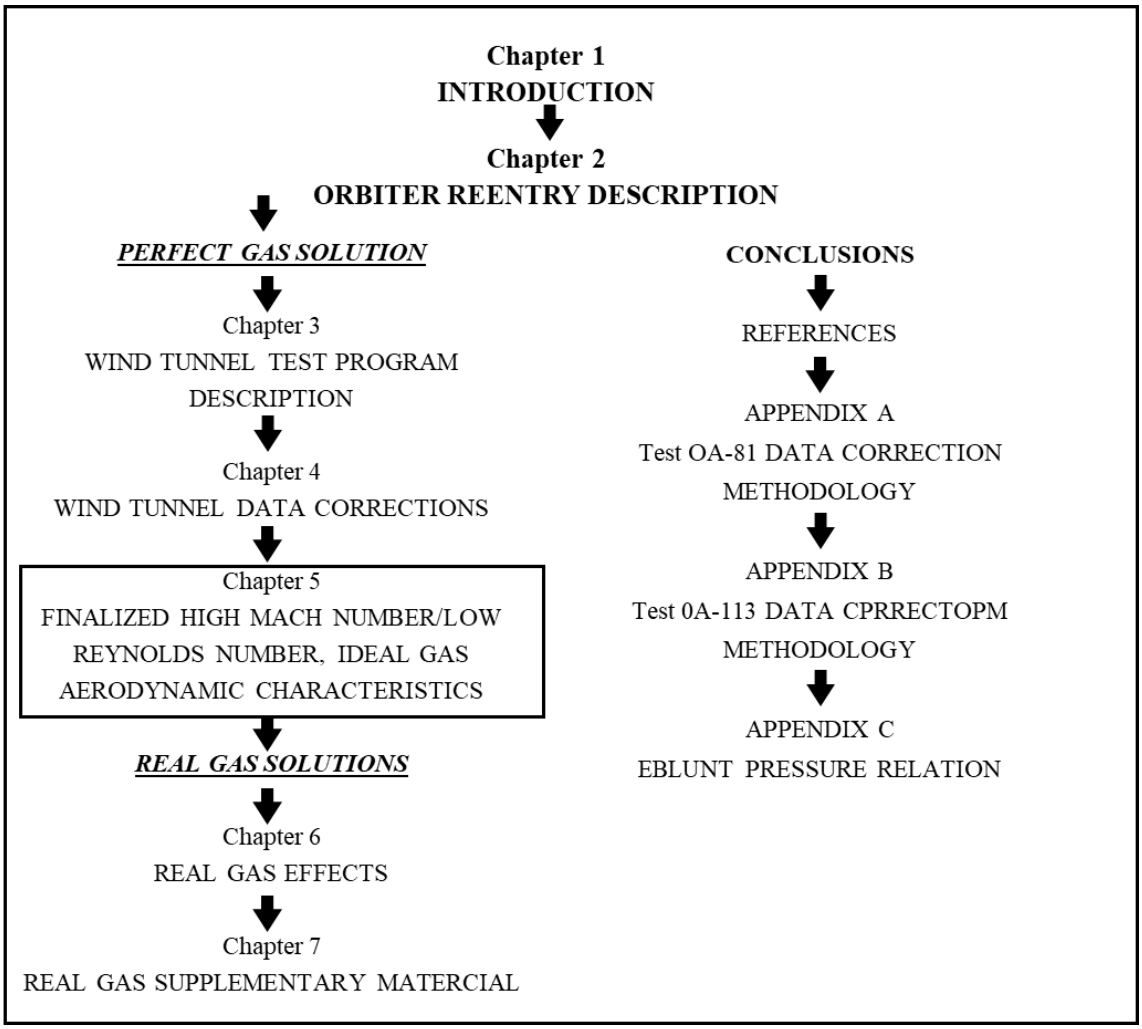

CHAPTER 5

FINALIZED HIGH MACH NUMBER/LOW REYNOLDS NUMBER, IDEAL GAS AERODYNAMIC CHARACTERISTICS

The complete hypersonic, perfect aerodynamic characteristic database for the Orbiter, including the effects of viscous interaction, is presented for the high Mach number/low Reynolds number regime. Real gas effects are presented in Chapter 6.

The coefficient data are referenced to the body axis system. The data are presented as a function of (1) viscous parameter, $0.005 \leq \bar{V}_\infty' \leq 0.08$; (2) angle of attack, $20° \leq \alpha \leq 50°$; (3) elevon control surface deflections, δ_E = -40°, 0 and 15; (4) body flap control surface deflections, δ_{BF} = -11.7°, 0 and 16.3; and (5) center-of-gravity locations based on body length, $X_{C.G.}$ /L= 0.65 and 0.675.

Figures 5.1 through 5.11 present total and incremental longitudinal normal force, axial force coefficients, and pitching moment coefficients. In addition, Tables 5.1 through 5.11 present the results in tabular form to facilitate the input requirements for reentry trajectory computations. The tables follow the corresponding figures; e.g., Table 5.1 follows Figure 5.1, Table 5.2 follows Figure 5.2, etc. Finally, the trim boundaries as a function of altitude and Mach number are presented in Figure 5.12.

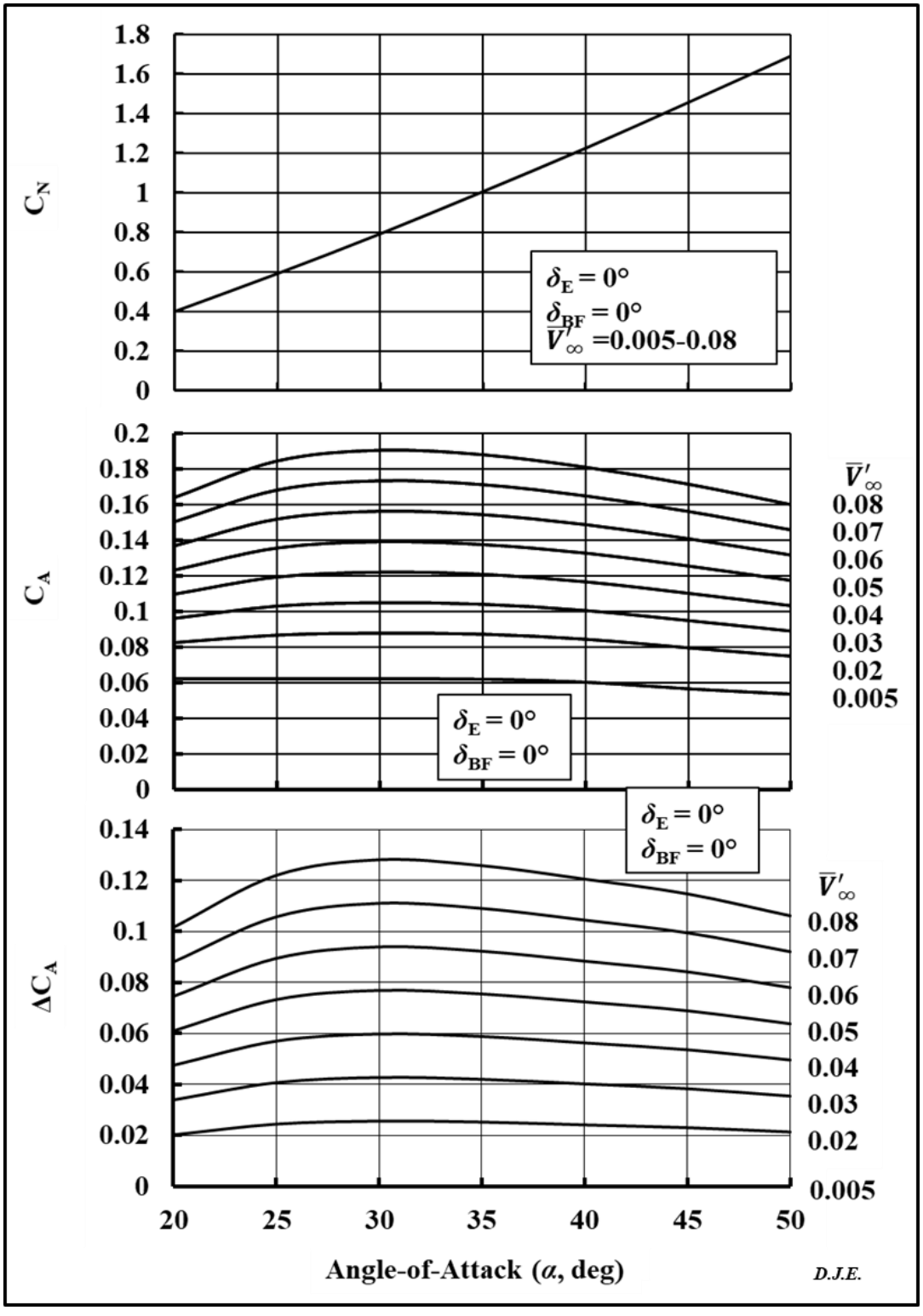

Figure 5.1 Normal, axial, and incremental axial force coefficients as a function of α and $\bar{V}'_\infty$ for $\delta_{BF} = 0°$ and $\delta_E = 0°$

Table 5.1 Normal, axial, and incremental axial force coefficients as a function of α and $\bar{V}'_\infty$ for $\delta_{BF} = 0°$ and $\delta_E = 0°$

Normal Force Coefficient (C_N)	
AOA degrees	**Body Flap = Elevon = 0°**
20	0.4
25	0.591
30	0.792
35	1.005
40	1.224
45	1.455
50	1.69

Axial Force Coefficient (C_A)								
Body Flap = Elevon = 0°								
AOA	**Viscous Parameter, $\bar{V}'_\infty$**							
degrees	0.005	0.02	0.03	0.04	0.05	0.06	0.07	0.08
20	0.0623	0.0826	0.0962	0.1098	0.1233	0.1369	0.1504	0.164
25	0.0624	0.0868	0.1031	0.1194	0.1357	0.1519	0.1682	0.1845
30	0.0623	0.0879	0.105	0.1221	0.1392	0.1563	0.1734	0.1905
35	0.0621	0.0873	0.1041	0.1209	0.1376	0.1544	0.1712	0.188
40	0.0604	0.0845	0.1006	0.1167	0.1328	0.1488	0.1649	0.181
45	0.0567	0.0797	0.095	0.1103	0.1256	0.1409	0.1562	0.1715
50	0.0537	0.075	0.0891	0.1033	0.1175	0.1317	0.1458	0.16

Incremental Axial Force Coefficient (ΔC_A)								
Body Flap = Elevon = 0°								
AOA	**Viscous Parameter, $\bar{V}'_\infty$**							
degrees	0.005	0.02	0.03	0.04	0.05	0.06	0.07	0.08
20	0	0.0202	0.0339	0.0475	0.061	0.0746	0.0881	0.1017
25	0	0.0244	0.0407	0.057	0.0733	0.0895	0.1058	0.1221
30	0	0.0256	0.0427	0.0598	0.0769	0.094	0.1111	0.1282
35	0	0.0252	0.042	0.0588	0.0755	0.0923	0.1091	0.1259
40	0	0.0241	0.0402	0.0563	0.0724	0.0884	0.1045	0.1206
45	0	0.023	0.0383	0.0536	0.0689	0.0842	0.0995	0.1148
50	0	0.0213	0.0354	0.0496	0.0638	0.078	0.0921	0.1062

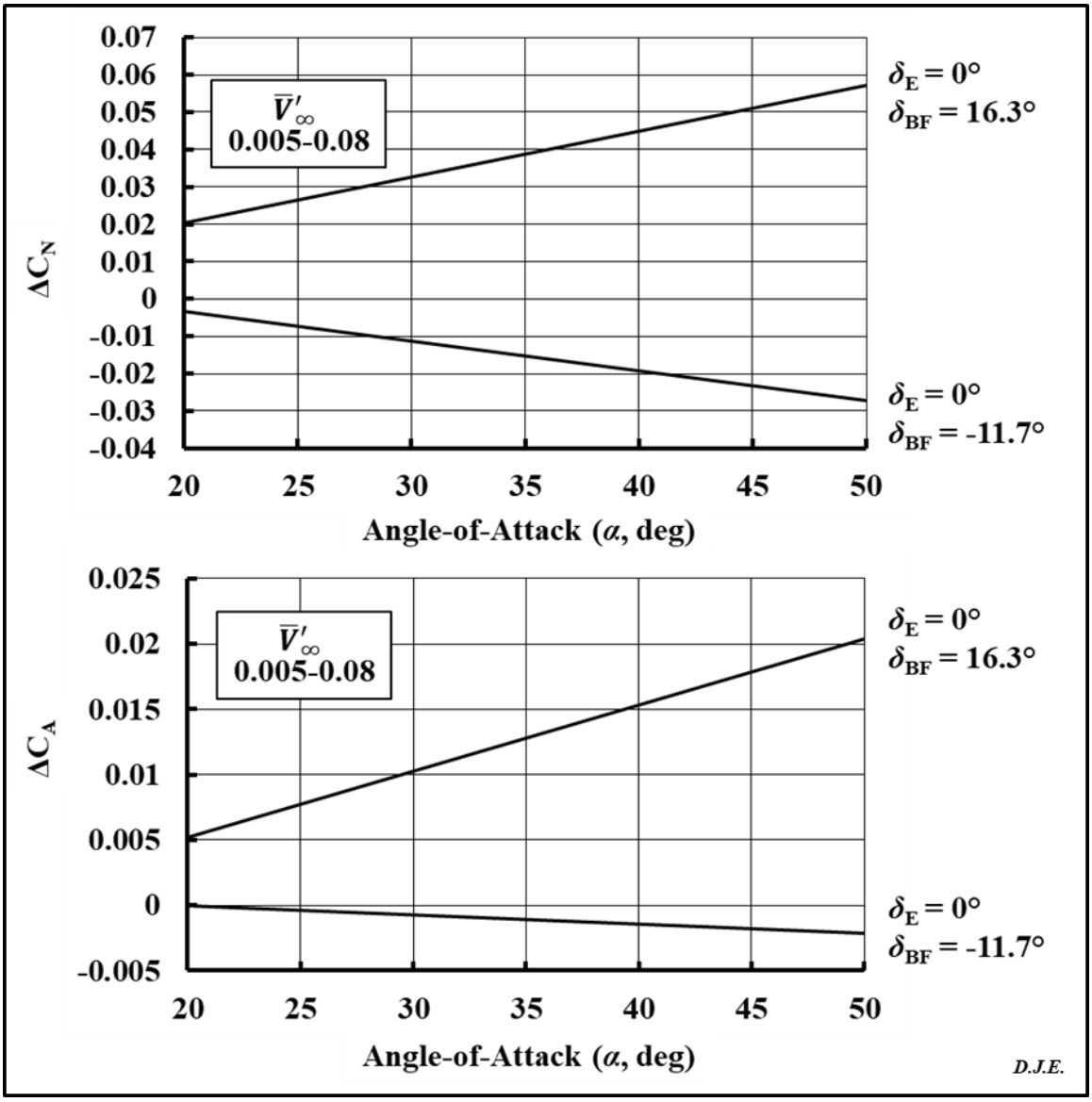

Figure 5.2 Incremental normal and axial Force coefficients as a function of α and $\bar{V}'_\infty$ for δ_{BF} = -11.7° and 16.3°, and δ_E = 0° (Body Flap Effectiveness)

Table 5.2 Incremental normal and axial Force coefficients as a function of α and $\bar{V}'_{\infty}$ for δ_{BF} = -11.7° and 16.3°, and δ_E= 0° (Body Flap Effectiveness)

AOA	Incremental Normal Force Coefficient (ΔC_N)	
deg	Body Flap = -11.7°	Body Flap = 16.3°
20	-0.0052	0.0188
25	-0.0074	0.0258
30	-0.0094	0.0336
35	-0.0136	0.0397
40	-0.018	0.0466
45	-0.024	0.0513
50	-0.0285	0.055

AOA	Incremental Axial Force Coefficient (ΔC_A)	
deg	Body Flap = -11.7°	Body Flap = 16.3°
20	-0.0002	0.0049
25	-0.0004	0.0081
30	-0.0003	0.0101
35	-0.0012	0.0131
40	-0.0012	0.0151
45	-0.0021	0.018
50	-0.002	0.0202

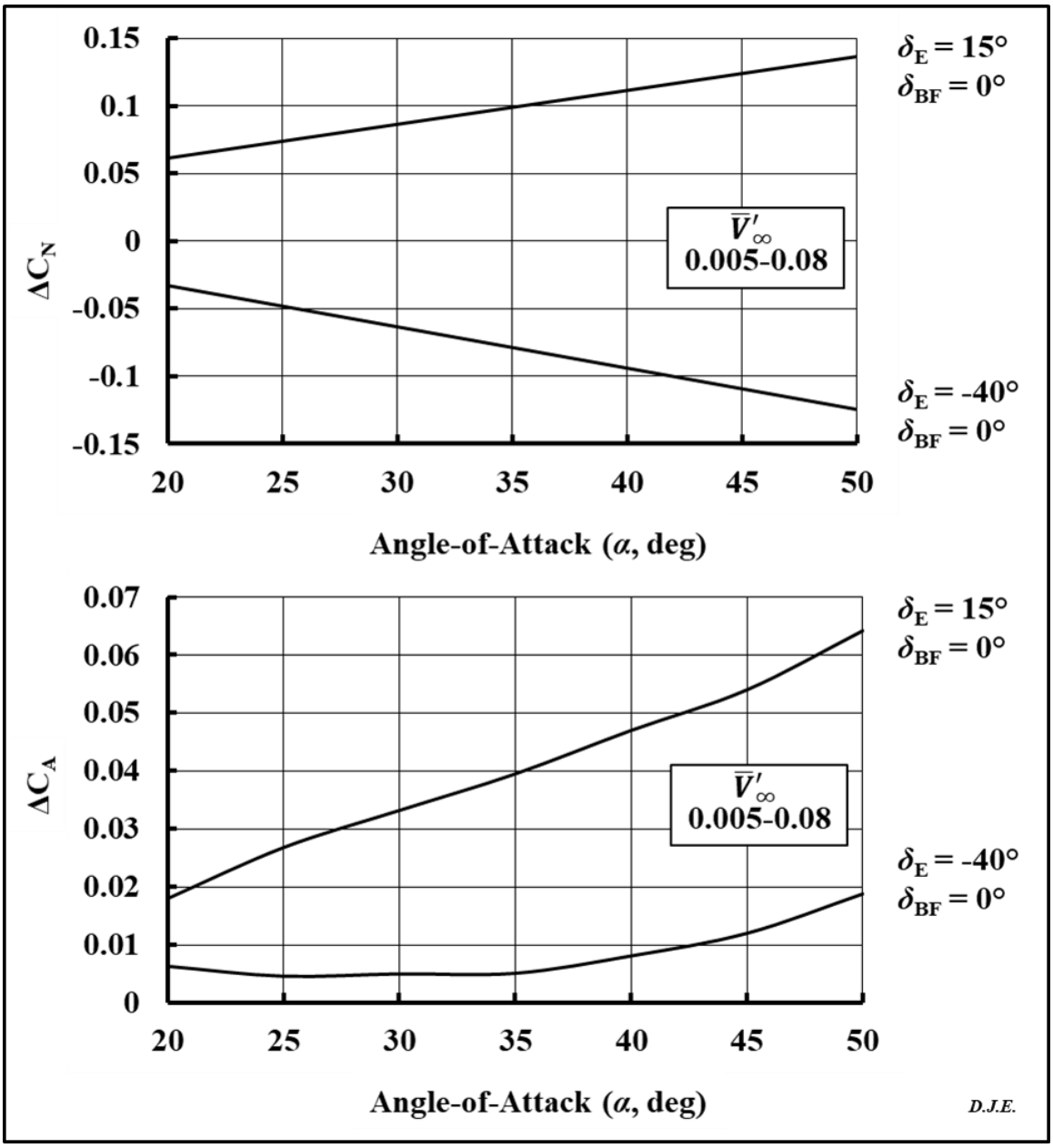

Figure 5.3 Incremental normal and axial force coefficients as a function of α and $\bar{V}'_{\infty}$ for δ_E = -40° and 15°, and δ_{BF}= 0° (Elevon Effectiveness)

Table 5.3 Incremental normal and axial force coefficients as a function of α and $\bar{V}'_{\infty}$ for δ_E = -40° and 15°, and δ_{BF}= 0° (Elevon Effectiveness)

AOA	Incremental Normal Force Coefficient (ΔC_N)	
deg	Elevon = -40°	Elevon = 15°
20	-0.0349	0.0587
25	-0.0476	0.0726
30	-0.0606	0.0885
35	-0.077	0.1002
40	-0.0937	0.1135
45	-0.1096	0.1223
50	-0.1254	0.1341

AOA	Incremental Axial Force Coefficient (ΔC_A)	
deg	Elevon = -40°	Elevon = 15°
20	0.0063	0.018
25	0.0046	0.0268
30	0.005	0.0332
35	0.0051	0.0395
40	0.0081	0.047
45	0.012	0.054
50	0.0188	0.0642

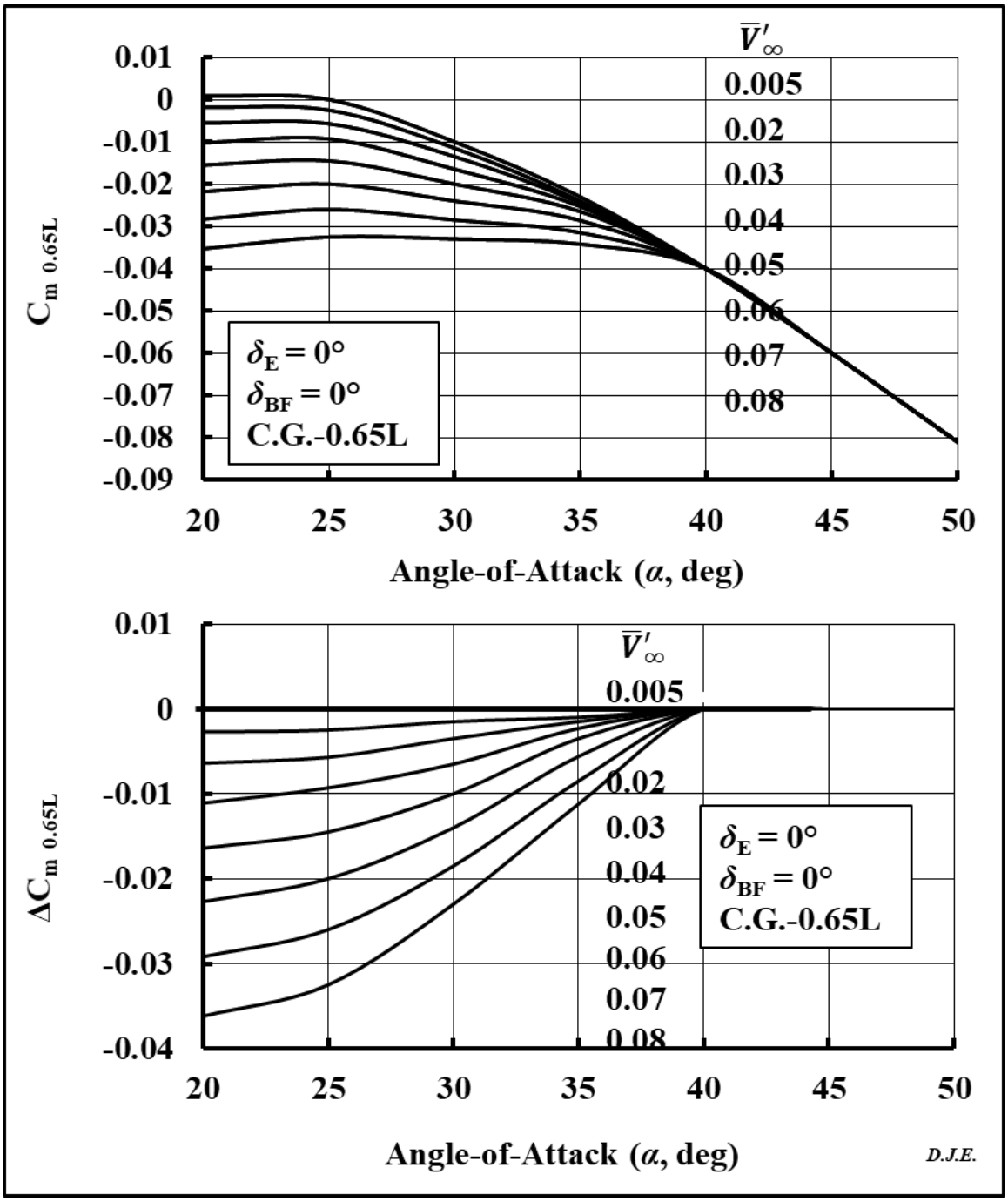

Figure 5.4 Pitching moment and incremental pitching moment coefficients as a function of α and $\bar{V}'_\infty$ for $\delta_{BF} = 0°$, $\delta_E = 0°$, and c.g.= 0.65L

Table 5.4 Pitching moment and incremental pitching moment coefficients as a function of α and $\bar{V}'_\infty$ for $\delta_{BF} = 0°$, $\delta_E = 0°$, and c.g.= 0.65L

Pitching Moment Coefficient Coefficient (C_M)								
Body Flap = Elevon = 0°, C.G.=0.65L								
AOA	**Viscous Parameter, $\bar{V}'_\infty$**							
deg	0.005	0.02	0.03	0.04	0.05	0.06	0.07	0.08
20	0.0009	-0.0018	-0.0055	-0.0102	-0.0155	-0.0218	-0.0283	-0.0353
25	0	-0.0025	-0.0057	-0.0093	-0.0145	-0.02	-0.026	-0.0325
30	-0.01	-0.0115	-0.0135	-0.0165	-0.02	-0.024	-0.0285	-0.033
35	-0.023	-0.024	-0.0245	-0.0253	-0.0265	-0.0286	-0.0315	-0.0342
40	-0.04	-0.04	-0.04	-0.04	-0.04	-0.04	-0.04	-0.04
45	-0.06	-0.06	-0.06	-0.06	-0.06	-0.06	-0.06	-0.06
50	-0.081	-0.081	-0.081	-0.081	-0.081	-0.081	-0.081	-0.081

Incremental Pitching Moment Coefficient (ΔC_M)								
Body Flap = Elevon = 0°, C.G.=0.65L								
AOA	**Viscous Parameter, $\bar{V}'_\infty$**							
deg	0.005	0.02	0.03	0.04	0.05	0.06	0.07	0.08
20	0	-0.0027	-0.0064	-0.0111	-0.0164	-0.0227	-0.0292	-0.0362
25	0	-0.0025	-0.0057	-0.0093	-0.0145	-0.02	-0.026	-0.0325
30	0	-0.0015	-0.0035	-0.0065	-0.01	-0.014	-0.0185	-0.023
35	0	-0.001	-0.0015	-0.0023	-0.0035	-0.0056	-0.0085	-0.0112
40	0	0	0	0	0	0	0	0
45	0	0	0	0	0	0	0	0
50	0	0	0	0	0	0	0	0

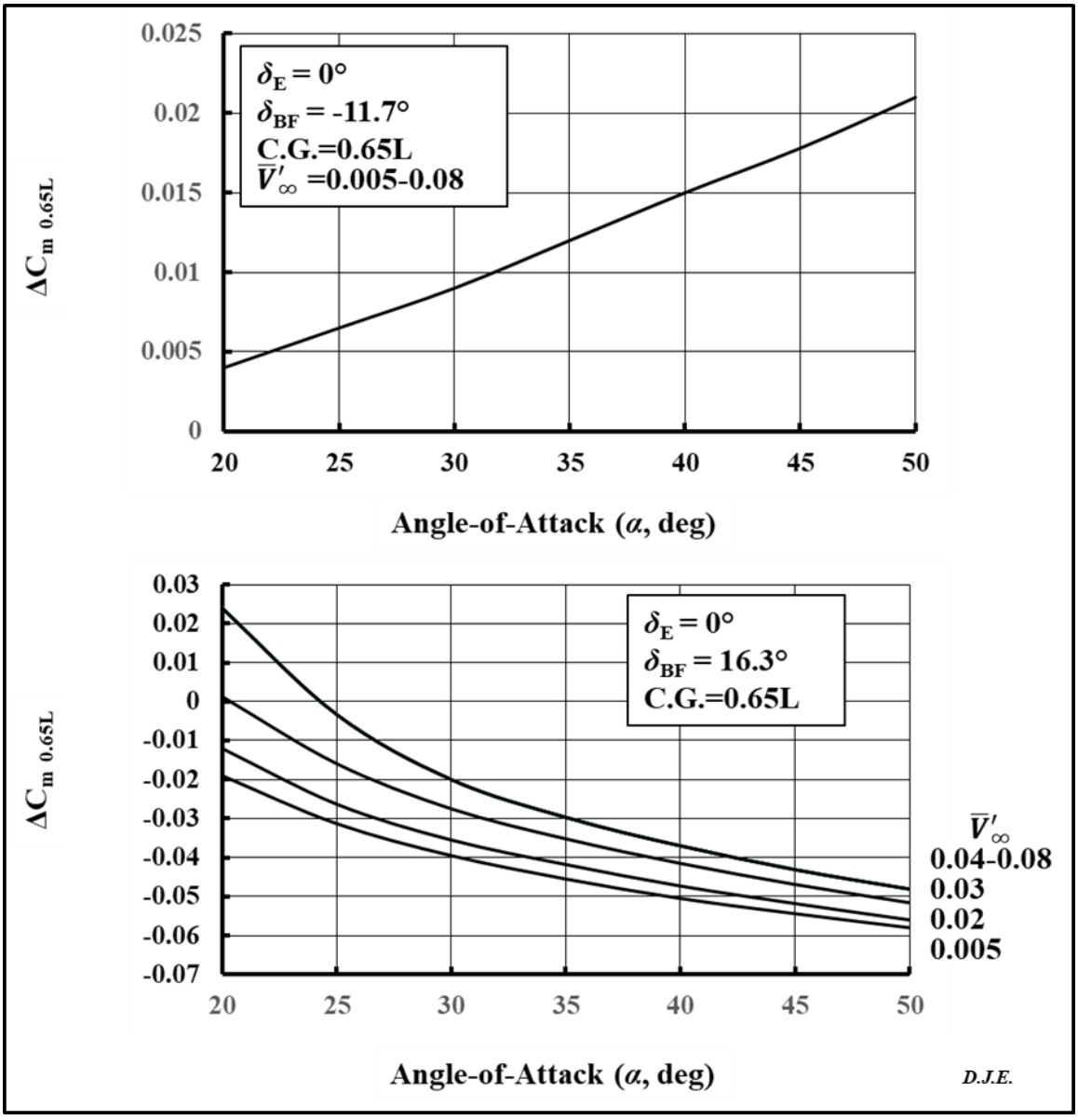

Figure 5.5 Pitching moment coefficient as a function of α and $\bar{V}'_\infty$ for δ_{BF} = -11.7° and 16.3°, δ_E= 0°, and c.g.= 0.65L (body flap effectiveness)

Table 5.5 Pitching moment coefficient as a function of α and $\bar{V}'_{\infty}$ for δ_{BF} = -11.7° and 16.3°, δ_E= 0°, and c.g.= 0.65L (body flap effectiveness)

Incremental Pitching Moment Coefficient (ΔC_M)	
AOA	C.G.=0.65L
degrees	
Body Flap = -11.7°	
20	0.004
25	0.0065
30	0.009
35	0.012
40	0.015
45	0.0178
50	0.021

Incremental Pitching Moment Coefficient (ΔC_M)								
Body Flap = 16.3°, C.G.=0.65L								
AOA	Viscous Parameter, $\bar{V}'_{\infty}$							
deg	0.005	0.02	0.03	0.04	0.05	0.06	0.07	0.08
20	-0.019	-0.012	0.0013	0.024	0.024	0.024	0.024	0.024
25	-0.0313	-0.0263	-0.0159	-0.0033	-0.0033	-0.0033	-0.0033	-0.0033
30	-0.0395	-0.0355	-0.0275	-0.02	-0.02	-0.02	-0.02	-0.02
35	-0.0455	-0.0418	-0.0352	-0.0297	-0.0297	-0.0297	-0.0297	-0.0297
40	-0.0505	-0.0473	-0.0415	-0.037	-0.037	-0.037	-0.037	-0.037
45	-0.0544	-0.0518	-0.0469	-0.0431	-0.0431	-0.0431	-0.0431	-0.0431
50	-0.058	-0.056	-0.0516	-0.0481	-0.0481	-0.0481	-0.0481	-0.0481

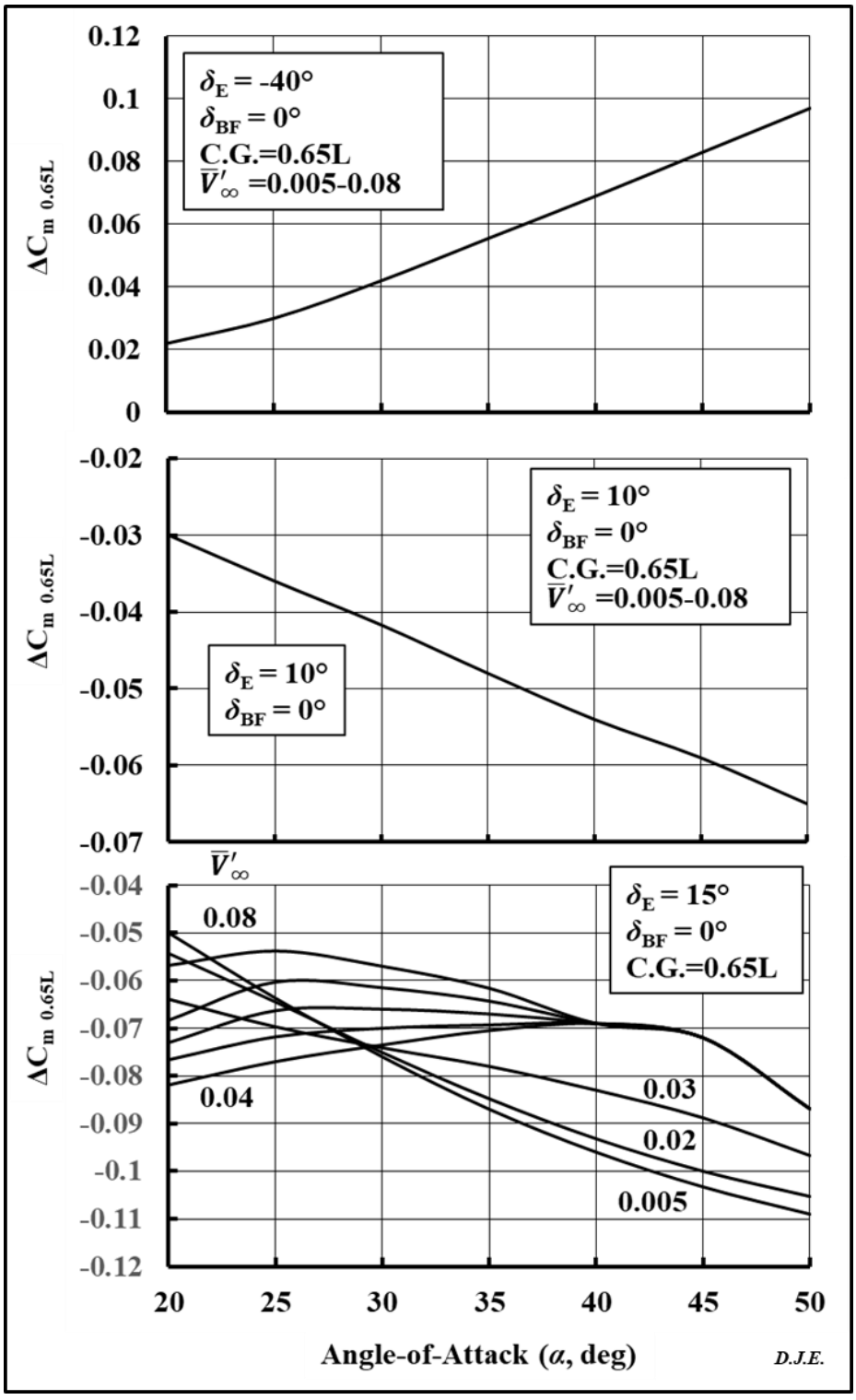

Figure 5.6 Pitching moment coefficient as a function of α and $\bar{V}'_\infty$ for δ_E = -40° and 15°, δ_{BF}= 0°, and c.g.= 0.65L (elevon effectiveness)

Table 5.6 Pitching moment coefficient as a function of α and $\bar{V}'_{\infty}$ for δ_E = -40° and 15°, δ_{BF}= 0°, and c.g.= 0.65L (elevon effectiveness)

Incremental Pitching Moment Coefficient (ΔC_M)	
AOA degrees	C.G.=0.65L
Elevon = -40°	
20	0.022
25	0.03
30	0.042
35	0.0555
40	0.069
45	0.083
50	0.097

Incremental Pitching Moment Coefficient (ΔC_M)	
AOA degrees	C.G.=0.65L
Elevon = 10°	
20	-0.03
25	-0.036
30	-0.0417
35	-0.048
40	-0.054
45	-0.059
50	-0.065

Incremental Pitching Moment Coefficient (ΔC_M)								
Elevon = 15°, C.G.=0.65L								
AOA	Viscous Parameter, $\bar{V}'_{\infty}$							
deg	0.005	0.02	0.03	0.04	0.05	0.06	0.07	0.08
20	-0.05	-0.0543	-0.0639	-0.0819	-0.0766	-0.073	-0.0683	-0.0568
25	-0.0637	-0.0645	-0.0697	-0.077	-0.0718	-0.0663	-0.0603	-0.0538
30	-0.076	-0.0751	-0.0741	-0.0735	-0.07	-0.066	-0.0615	-0.057
35	-0.087	-0.0848	-0.078	-0.0705	-0.0693	-0.067	-0.0643	-0.0616
40	-0.096	-0.0932	-0.083	-0.069	-0.069	-0.069	-0.069	-0.069
45	-0.1033	-0.1	-0.0888	-0.072	-0.072	-0.072	-0.072	-0.072
50	-0.109	-0.1053	-0.0967	-0.0869	-0.0869	-0.0869	-0.0869	-0.0869

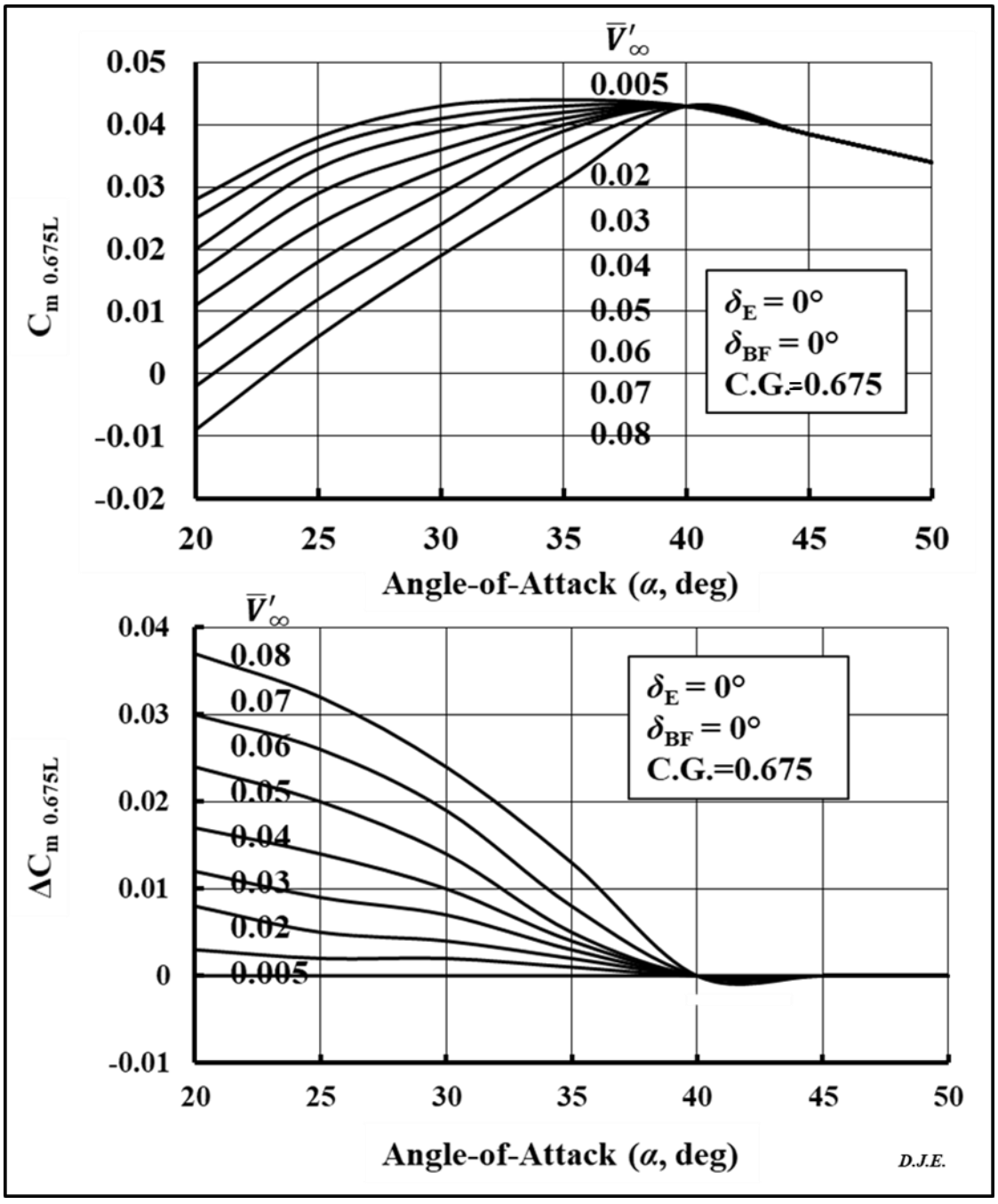

Figure 5.7 Pitching moment and incremental pitching moment coefficients as a function of α and $\bar{V}'_\infty$ for $\delta_{BF} = 0°$, $\delta_E = 0°$, and c.g.= 0.675L

Table 5.7 Pitching moment and incremental pitching moment coefficients as a function of α and $\bar{V}'_\infty$ for $\delta_{BF} = 0°$, $\delta_E = 0°$, and c.g.= 0.675L

Pitching Moment Coefficient Coefficient (C_M)								
Body Flap = Elevon = 0°, C.G.=0.675L								
AOA	Viscous Parameter, $\bar{V}'_\infty$							
deg	0.005	0.02	0.03	0.04	0.05	0.06	0.07	0.08
20	0.028	0.025	0.02	0.016	0.011	0.004	-0.002	-0.009
25	0.038	0.036	0.033	0.029	0.024	0.018	0.012	0.006
30	0.043	0.041	0.039	0.036	0.033	0.029	0.024	0.019
35	0.044	0.043	0.042	0.041	0.04	0.039	0.036	0.031
40	0.043	0.043	0.043	0.043	0.043	0.043	0.043	0.043
45	0.0385	0.0385	0.0385	0.0385	0.0385	0.0385	0.0385	0.0385
50	0.034	0.034	0.034	0.034	0.034	0.034	0.034	0.034

Incremental Pitching Moment Coefficient (ΔC_M)								
Body Flap = Elevon = 0°, C.G.=0.675L								
AOA	Viscous Parameter, $\bar{V}'_\infty$							
deg	0.005	0.02	0.03	0.04	0.05	0.06	0.07	0.08
20	0	0.003	0.008	0.012	0.017	0.024	0.03	0.037
25	0	0.002	0.005	0.009	0.014	0.02	0.026	0.032
30	0	0.002	0.004	0.007	0.01	0.014	0.019	0.024
35	0	0.001	0.002	0.003	0.004	0.005	0.008	0.013
40	0	0	0	0	0	0	0	0
45	0	0	0	0	0	0	0	0
50	0	0	0	0	0	0	0	0

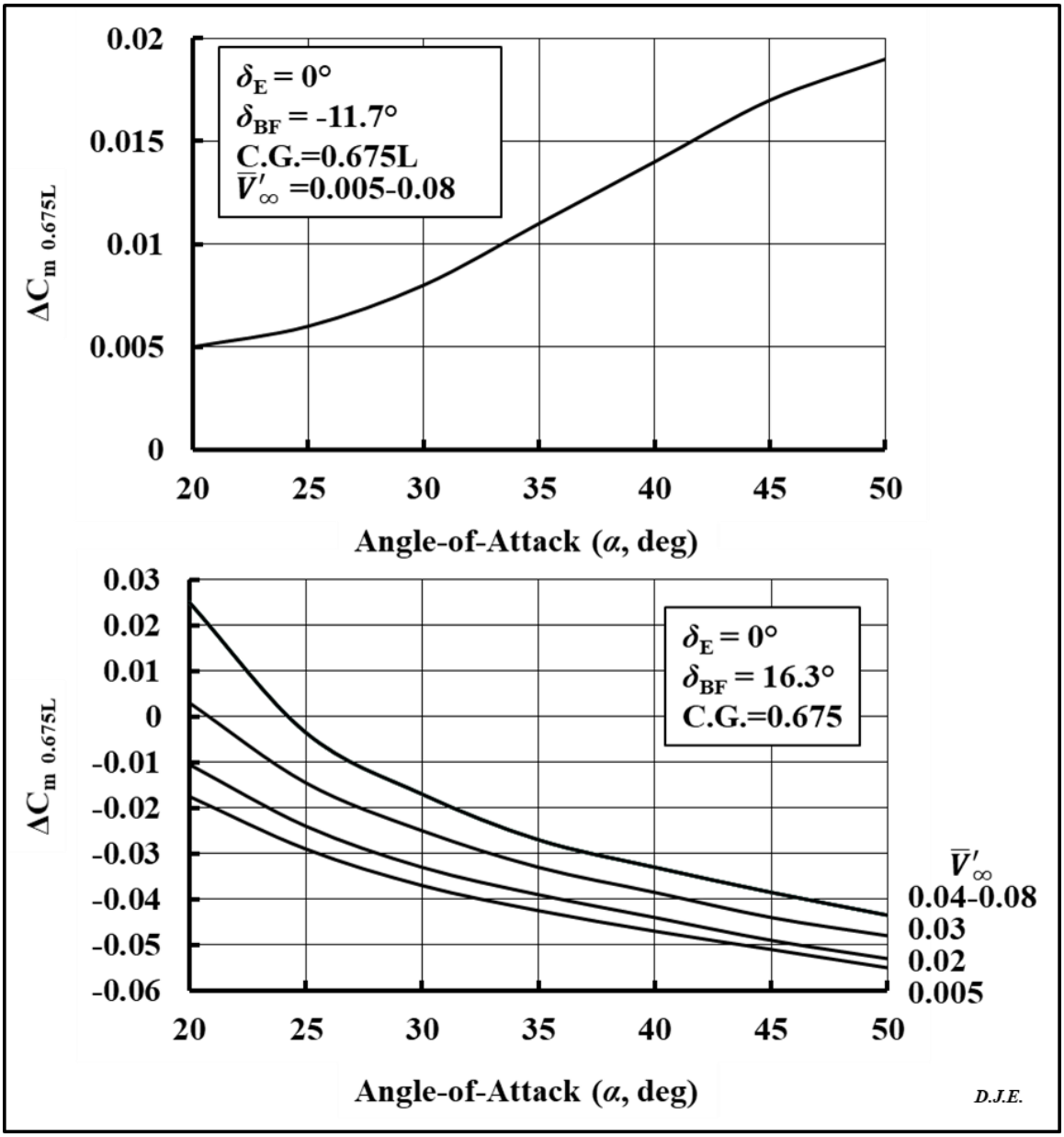

Figure 5.8 Pitching moment coefficient as a function of α and $\bar{V}'_\infty$ for δ_{BF} = -11.7° and 16.3°, δ_E= 0°, and c.g.= 0.675L (body flap effectiveness)

Table 5.8 Pitching moment coefficient as a function of α and $\bar{V}'_\infty$ for δ_{BF} = -11.7° and 16.3°, δ_E= 0°, and c.g.= 0.675L (body flap effectiveness)

Incremental Pitching Moment Coefficient (ΔC_M)	
AOA	C.G.=0.675L
degrees	
Body Flap = -11.7°	
20	0.005
25	0.006
30	0.008
35	0.011
40	0.014
45	0.017
50	0.019

Incremental Pitching Moment Coefficient (ΔC_M)								
Body Flap = 16.3°, C.G.=0.675L								
AOA	Viscous Parameter, $\bar{V}'_\infty$							
deg	0.005	0.02	0.03	0.04	0.05	0.06	0.07	0.08
20	-0.0175	-0.0105	0.003	0.025	0.025	0.025	0.025	0.025
25	-0.029	-0.024	-0.0145	-0.0035	-0.0035	-0.0035	-0.0035	-0.0035
30	-0.037	-0.033	-0.025	-0.017	-0.017	-0.017	-0.017	-0.017
35	-0.0425	-0.039	-0.033	-0.027	-0.027	-0.027	-0.027	-0.027
40	-0.047	-0.044	-0.0385	-0.033	-0.033	-0.033	-0.033	-0.033
45	-0.051	-0.049	-0.044	-0.0385	-0.0385	-0.0385	-0.0385	-0.0385
50	-0.055	-0.053	-0.048	-0.0435	-0.0435	-0.0435	-0.0435	-0.0435

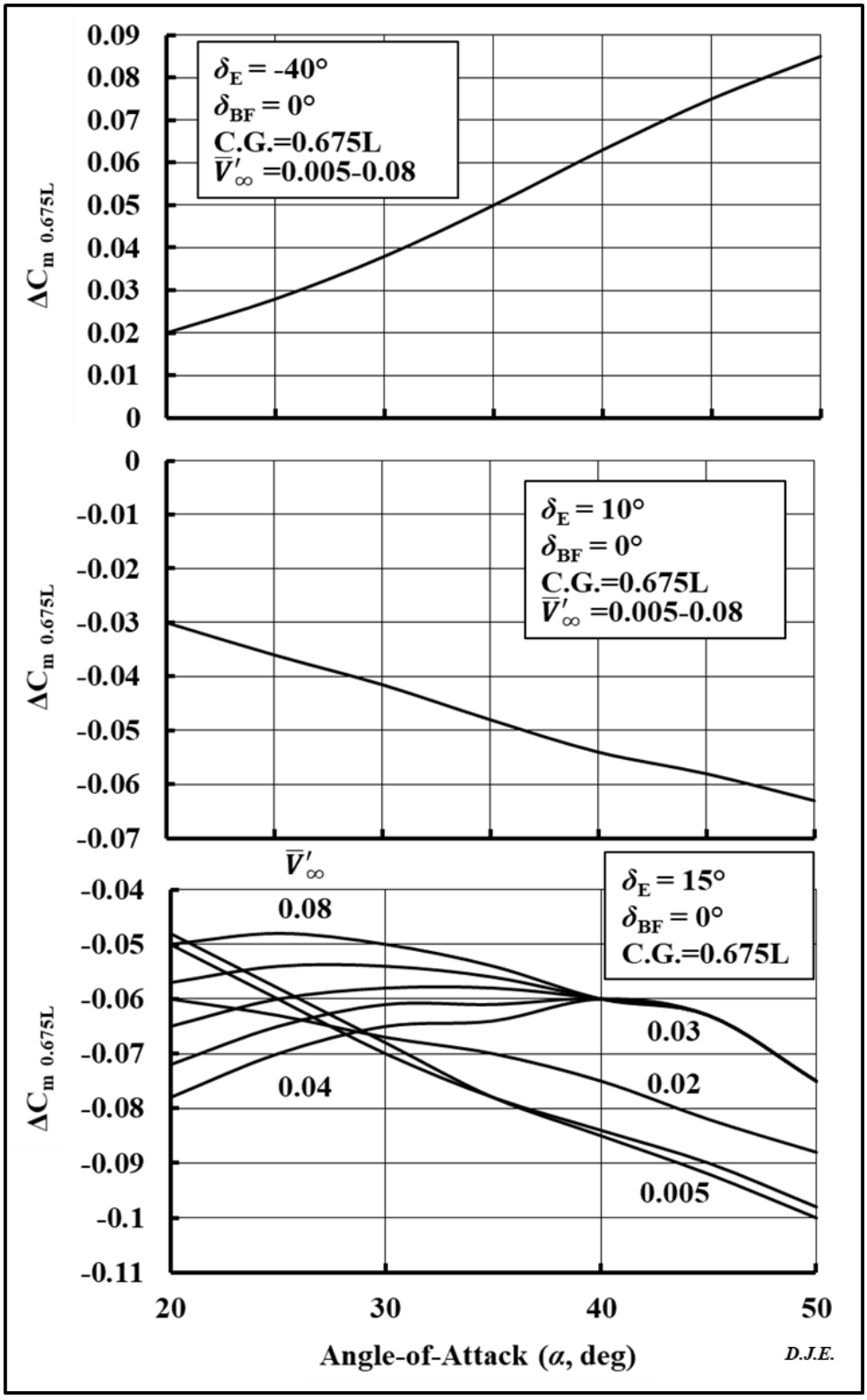

Figure 5.9 Pitching moment coefficient as a function of α and $\bar{V}'_\infty$ for δ_E = -40°, 10°, and 15°, δ_{BF}= 0°, and c.g.= 0.675L (elevon effectiveness)

Table 5.9 Pitching moment coefficient as a function of α and $\bar{V}'_{\infty}$ for δ_E = -40°, 10°, and 15°, δ_{BF}= 0°, and c.g.= 0.675L (elevon effectiveness)

Incremental Pitching Moment Coefficient (ΔC_M)	
AOA degrees	C.G.=0.675L
Elevon = -40°	
20	0.02
25	0.028
30	0.038
35	0.05
40	0.063
45	0.075
50	0.085

Incremental Pitching Moment Coefficient (ΔC_M)	
AOA degrees	C.G.=0.675L
Elevon = 10°	
20	-0.03
25	-0.036
30	-0.0415
35	-0.048
40	-0.054
45	-0.058
50	-0.063

Incremental Pitching Moment Coefficient (ΔC_M)								
Elevon = 15°, C.G.=0.675L								
AOA	Viscous Parameter, $\bar{V}'_{\infty}$							
deg	0.005	0.02	0.03	0.04	0.05	0.06	0.07	0.08
20	-0.048	-0.05	-0.06	-0.078	-0.072	-0.065	-0.057	-0.05
25	-0.058	-0.06	-0.063	-0.07	-0.065	-0.06	-0.054	-0.048
30	-0.068	-0.07	-0.067	-0.065	-0.061	-0.058	-0.054	-0.05
35	-0.078	-0.078	-0.07	-0.064	-0.061	-0.058	-0.056	-0.054
40	-0.085	-0.084	-0.075	-0.06	-0.06	-0.06	-0.06	-0.06
45	-0.092	-0.09	-0.082	-0.063	-0.063	-0.063	-0.063	-0.063
50	-0.1	-0.098	-0.088	-0.075	-0.075	-0.075	-0.075	-0.075

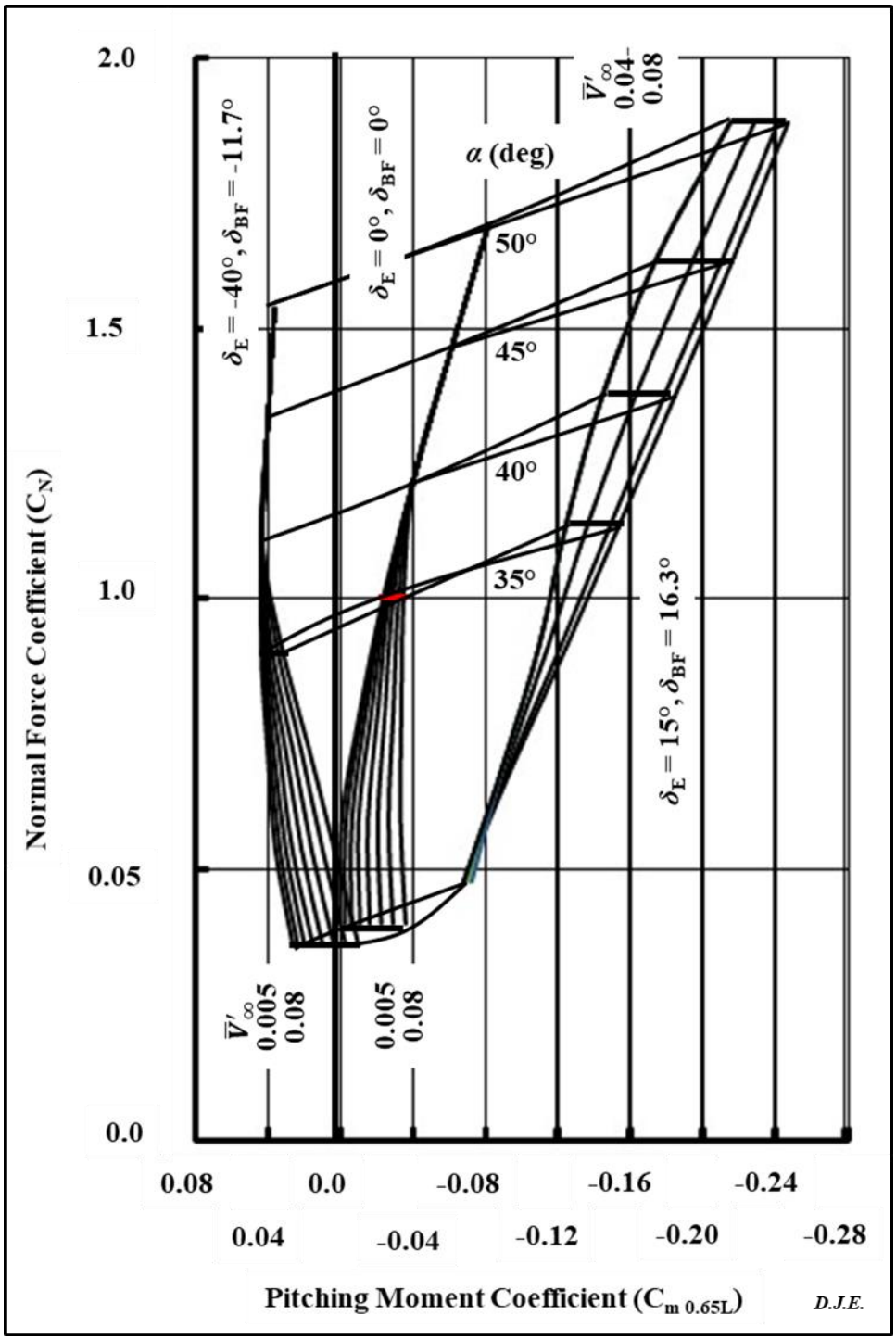

Figure 5.10 Maximum control surface deflections stability characteristics as a function of α and $\bar{V}'_\infty$ for c.g.= 0.65L

Table 5.10 Maximum control surface deflections stability characteristics as a function of α and $\bar{V}'_{\infty}$ for c.g.= 0.65L

Stability Characteristics									
Body Flap = -11.7°, Elevon = -40° , C.G.= 0.65L									
AOA	**CN**	**CM**	**CM**	**CM**	**CM**	**CM**	**CM**	**CM**	**CM**
deg	**Viscous Parameter, $\bar{V}'_{\infty}$**								
		0.005	0.02	0.03	0.04	0.05	0.06	0.07	0.08
20	0.3599	0.0269	0.0242	0.0205	0.0158	0.0105	0.0042	-0.0023	-0.0093
25	0.536	0.0365	0.034	0.0308	0.0272	0.022	0.0165	0.0105	0.004
30	0.722	0.041	0.0395	0.0375	0.0345	0.031	0.027	0.0225	0.018
35	0.9144	0.0445	0.0435	0.043	0.0422	0.041	0.0389	0.036	0.0333
40	1.1123	0.044	0.044	0.044	0.044	0.044	0.044	0.044	0.044
45	1.3214	0.0408	0.0408	0.0408	0.0408	0.0408	0.0408	0.0408	0.0408
50	1.5361	0.037	0.037	0.037	0.037	0.037	0.037	0.037	0.037
Body Flap = 0°, Elevon = 0° , C.G.= 0.65L									
20	0.4	0.0009	-0.0018	-0.0055	-0.0102	-0.0155	-0.0218	-0.0283	-0.0353
25	0.591	0	-0.0025	-0.0057	-0.0093	-0.0145	-0.02	-0.026	-0.0325
30	0.792	-0.01	-0.0115	-0.0135	-0.0165	-0.02	-0.024	-0.0285	-0.033
35	1.005	-0.023	-0.024	-0.0245	-0.0253	-0.0265	-0.0286	-0.0315	-0.0342
40	1.224	-0.04	-0.04	-0.04	-0.04	-0.04	-0.04	-0.04	-0.04
45	1.455	-0.06	-0.06	-0.06	-0.06	-0.06	-0.06	-0.06	-0.06
50	1.69	-0.081	-0.081	-0.081	-0.081	-0.081	-0.081	-0.081	-0.081
Body Flap = 16.3°, Elevon = 15° , C.G.= 0.65L									
20	0.4775	-0.0681	-0.0681	-0.0681	-0.0681	-0.0681	-0.0708	-0.0726	-0.0681
25	0.6894	-0.095	-0.0933	-0.0913	-0.0896	-0.0896	-0.0896	-0.0896	-0.0896
30	0.9141	-0.1255	-0.1221	-0.1151	-0.11	-0.11	-0.11	-0.11	-0.11
35	1.1449	-0.1555	-0.1506	-0.1377	-0.1255	-0.1255	-0.1253	-0.1255	-0.1255
40	1.3841	-0.1865	-0.1805	-0.1645	-0.146	-0.146	-0.146	-0.146	-0.146
45	1.6286	-0.2177	-0.2118	-0.1957	-0.1751	-0.1751	-0.1751	-0.1751	-0.1751
50	1.8791	-0.248	-0.2423	-0.2293	-0.216	-0.216	-0.216	-0.216	-0.216

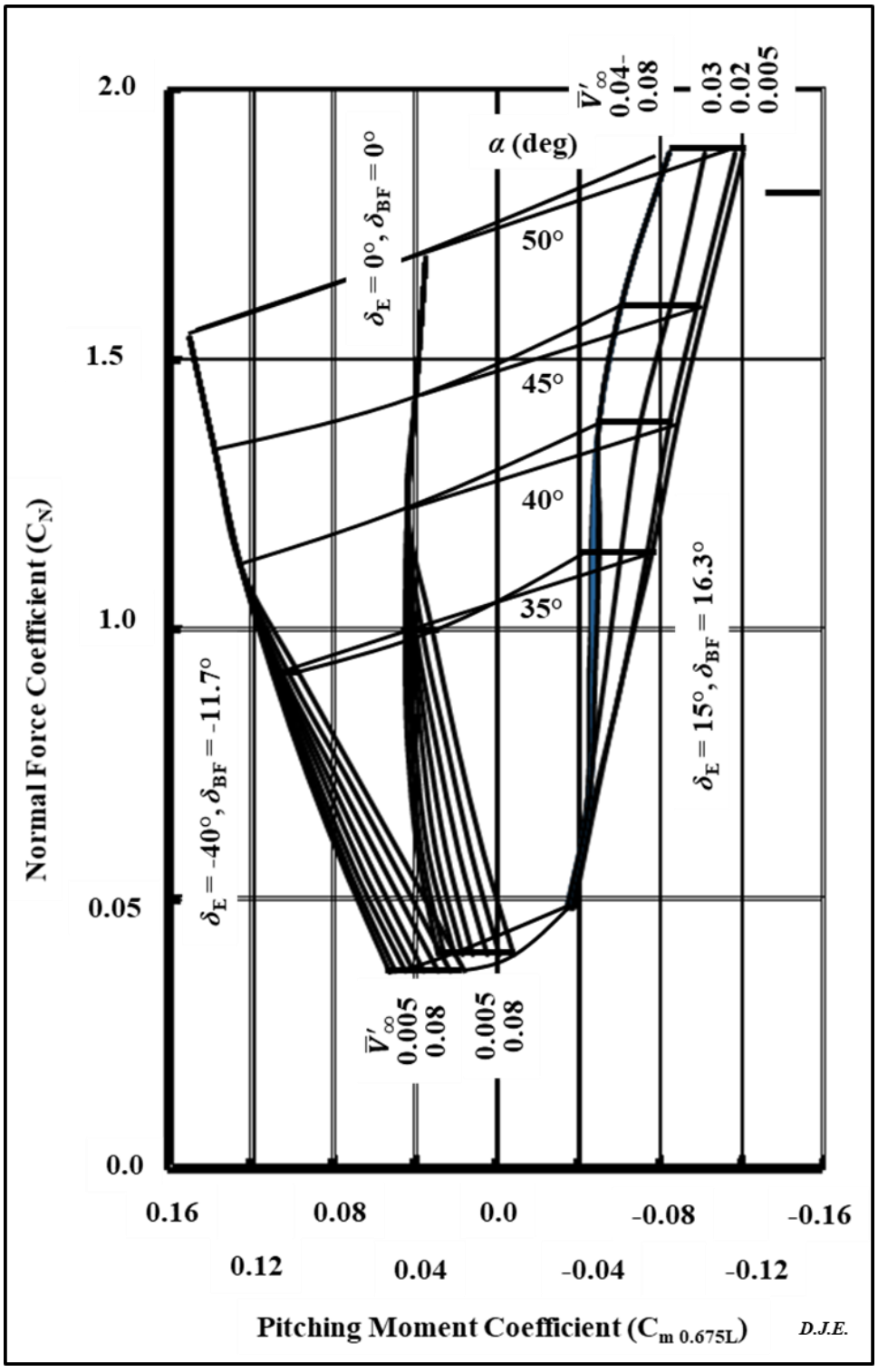

Figure 5.11 Maximum control surface deflections stability characteristics as a function of α and $\bar{V}'_\infty$ for c.g.= 0.675L

Table 5.11 Maximum control surface deflections stability characteristics as a function of α and $\bar{V}'_{\infty}$ for c.g.= 0.675L

Stability Characteristics									
Body Flap = -11.7°, Elevon = -40° , C.G.= 0.675L									
AOA	**CN**	**CM**	**CM**	**CM**	**CM**	**CM**	**CM**	**CM**	**CM**
deg	**Viscous Parameter, $\bar{V}'_{\infty}$**								
		0.005	0.02	0.03	0.04	0.05	0.06	0.07	0.08
20	0.3599	0.054	0.051	0.046	0.042	0.037	0.03	0.024	0.017
25	0.536	0.0745	0.0725	0.0695	0.0655	0.0605	0.0545	0.0485	0.0425
30	0.722	0.094	0.092	0.09	0.087	0.084	0.08	0.075	0.07
35	0.9144	0.1115	0.1105	0.1095	0.1085	0.1075	0.1065	0.1035	0.0985
40	1.1123	0.127	0.127	0.127	0.127	0.127	0.127	0.127	0.127
45	1.3214	0.1393	0.1393	0.1393	0.1393	0.1393	0.1393	0.1393	0.1393
50	1.5361	0.152	0.152	0.152	0.152	0.152	0.152	0.152	0.152
Body Flap = 0°, Elevon = 0° , C.G.= 0.675L									
20	0.4	0.028	0.025	0.02	0.016	0.011	0.004	-0.002	-0.009
25	0.591	0.038	0.036	0.033	0.029	0.024	0.018	0.012	0.006
30	0.792	0.043	0.041	0.039	0.036	0.033	0.029	0.024	0.019
35	1.005	0.044	0.043	0.042	0.041	0.04	0.039	0.036	0.031
40	1.224	0.043	0.043	0.043	0.043	0.043	0.043	0.043	0.043
45	1.455	0.0385	0.0385	0.0385	0.0385	0.0385	0.0385	0.0385	0.0385
50	1.69	0.034	0.034	0.034	0.034	0.034	0.034	0.034	0.034
Body Flap = 16.3°, Elevon = 15° , C.G.= 0.675L									
20	0.4775	-0.0375	-0.0355	-0.037	-0.037	-0.036	-0.036	-0.034	-0.034
25	0.6894	-0.049	-0.048	-0.0445	-0.0445	-0.0445	-0.0455	-0.0455	-0.0455
30	0.9141	-0.062	-0.062	-0.053	-0.046	-0.045	-0.046	-0.047	-0.048
35	1.1449	-0.0765	-0.074	-0.061	-0.05	-0.048	-0.046	-0.047	-0.05
40	1.3841	-0.089	-0.085	-0.0705	-0.05	-0.05	-0.05	-0.05	-0.05
45	1.6286	-0.1045	-0.1005	-0.0875	-0.063	-0.063	-0.063	-0.063	-0.063
50	1.8791	-0.121	-0.117	-0.102	-0.0845	-0.0845	-0.0845	-0.0845	-0.0845

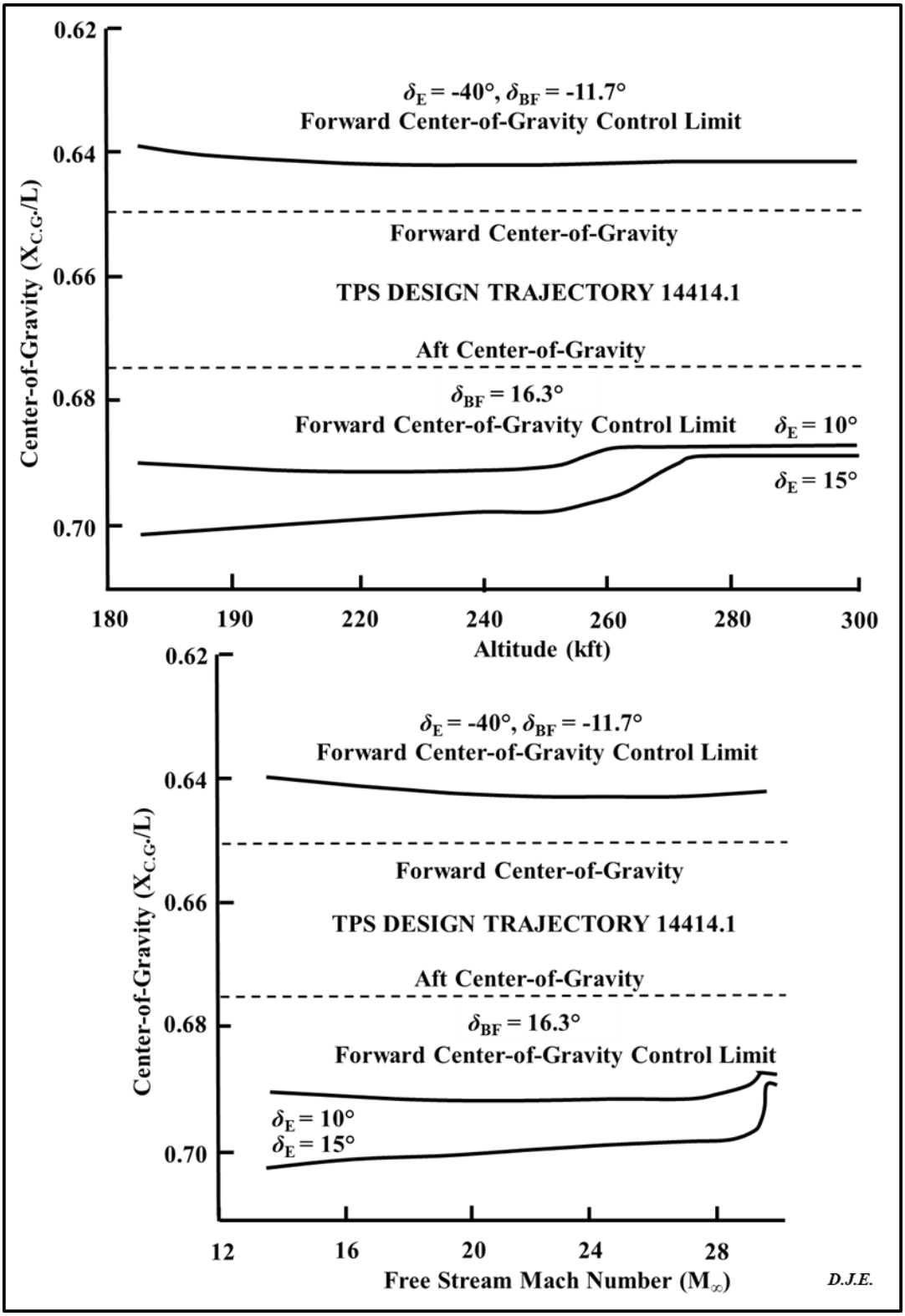

Figure 5.12 Trim boundaries as a function of altitude and M_∞

The resultant aerodynamic characteristics can be summed up as follows:

Normal and Axial Force Coefficients

- δ_{BF} = 0° and δ_E = *0*°: C_N increases with α but unaffected by $\bar{V}_\infty'$.
- δ_{BF} = 0° and δ_E = *0*°: C_A increases with $\bar{V}_\infty'$ (two times that for $M_\infty < 10$).
- Positive control surface deflections: ΔC_N and ΔC_A, increase with α, but independent of $\bar{V}_\infty'$.
- Negative control surface deflections: ΔC_N and ΔC_A decrease with α, but independent of $\bar{V}_\infty'$.
- Lift to drag decreased measurably with $\bar{V}_\infty'$.

Pitching Moment Coefficients

- δ_{BF} = 0° and δ_E = *0*°: C_M becomes more negative (nose-down) with increasing $\bar{V}_\infty'$ and α, but becomes unaffected for increasing $\bar{V}_\infty'$ for $\alpha \geq 40°$.
- δ_{BF} = -11.7° and δ_E = *0*°: ΔC_M increases with α.
- δ_{BF} = 16.3° and δ_E = *0*°: ΔC_M decreases with α, but increases with $\bar{V}_\infty'$.
- δ_{BF} = 0° and δ_E = *-40*°: ΔC_M increases with α.
- δ_{BF} = 0° and δ_E = *10*°: ΔC_M decreases with α, but unaffected by $\bar{V}_\infty'$.
- δ_{BF} = 0° and δ_E = *15*°: ΔC_M decreases with $20° < \alpha < 40°$, but increases with $\bar{V}_\infty'$.
- δ_{BF} = 0° and δ_E = *15*°: ΔC_M becomes more positive (nose-up) with increasing viscous parameters caused by elevon flow separation. The change in pitching moment and correspondingly no change in the forces implies that the pressure distribution was drastically affected by elevon flow separation. In contrast, the

integrated forces are compensated for giving the same values regardless of the separation magnitude. Further theoretical analyses are required to verify the effects of flow separation.

The wind tunnel results demonstrate that the control limits (δ_{BF} = -11.7° and δ_E = *-40*°, and δ_{BF} = 16.3° and δ_E = *15*°) are sufficient to provide stability. Understanding ideal gas and viscous interaction effects for zero and negative control surface deflection is considered well in hand, but further research is required for positive elevon control surface deflections δ_{BF} = -11.7° and δ_E = *-40*° and δ_{BF} = 16.3° and δ_E = *15*° for all

NEXT CHAPTER DESCRIPTION

The next chapter, Chapter 6, combines real gas and viscous interaction in the high-altitude regime. Viscous interaction mainly affects the axial force, whereas real gas affects the pressure distribution on the body at a high angle of attack.

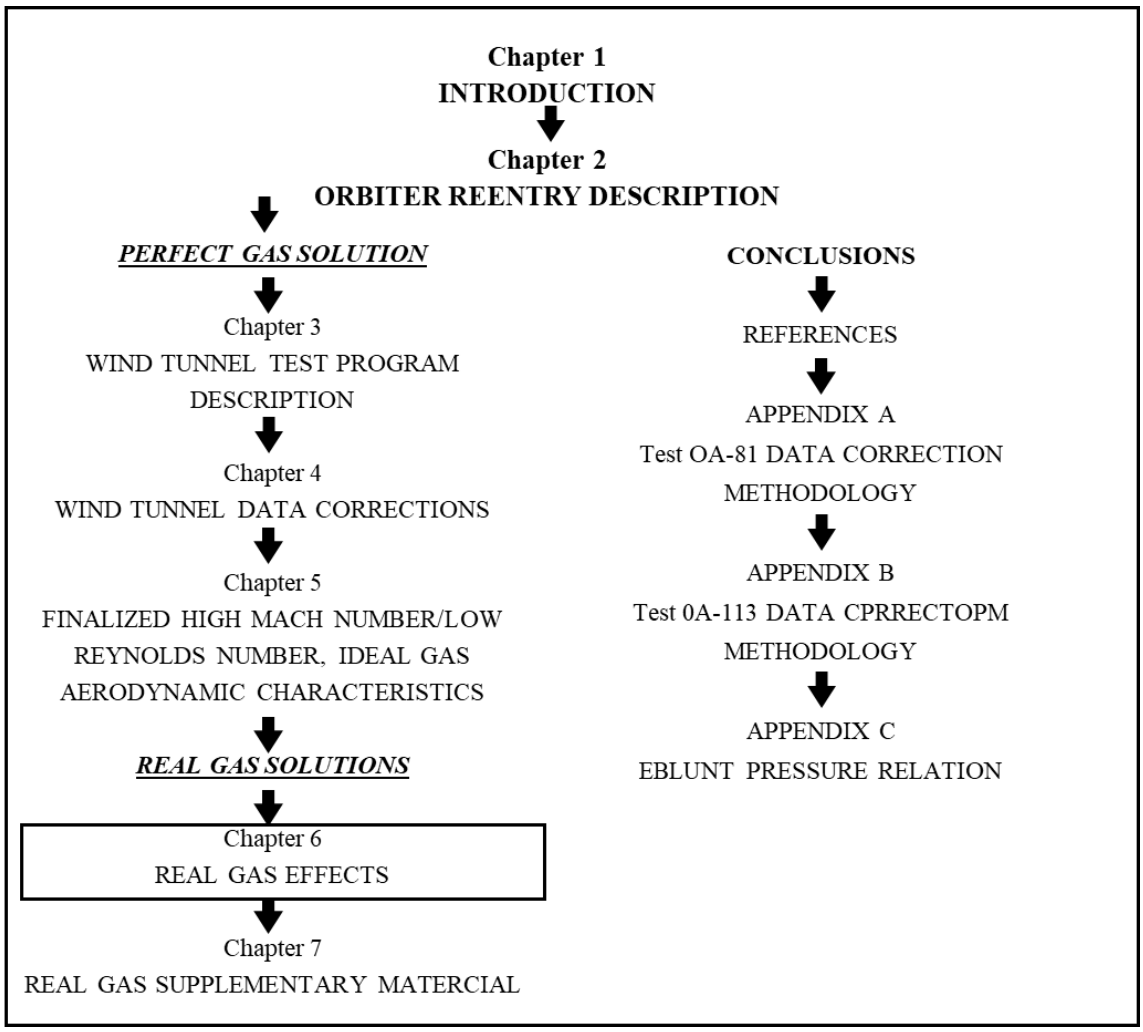
Chapter 1
INTRODUCTION
Chapter 2
ORBITER REENTRY DESCRIPTION
PERFECT GAS SOLUTION
Chapter 3
WIND TUNNEL TEST PROGRAM
DESCRIPTION
Chapter 4
WIND TUNNEL DATA CORRECTIONS
Chapter 5
FINALIZED HIGH MACH NUMBER/LOW
REYNOLDS NUMBER, IDEAL GAS
AERODYNAMIC CHARACTERISTICS
REAL GAS SOLUTIONS
Chapter 6
REAL GAS EFFECTS
Chapter 7
REAL GAS SUPPLEMENTARY MATERCIAL
CONCLUSIONS
REFERENCES
APPENDIX A
Test OA-81 DATA CORRECTION
METHODOLOGY
APPENDIX B
Test 0A-113 DATA CPRRECTOPM
METHODOLOGY
APPENDIX C
EBLUNT PRESSURE RELATION

CHAPTER 6

REAL GAS EFFECTS

As the Orbiter enters the atmosphere at a moderate to high angle of attack, critical heating on the windward surface occurs between 300,000 ft. and 200,000 ft. As a result, the molecules behind a high-velocity shock wave become vibrationally excited, partially or entirely dissociated depending on their bond energy, and perhaps partially ionized at very high speeds. These aspects of hypersonic flow are typically called "real gas" effects. In other words, the gas molecules within the shock layer are excited to higher vibrational, chemical, and ionization energy modes. At these altitudes, the flowfield experiences three states: frozen, non-equilibrium, and equilibrium flow. However, since no CFD analysis techniques were available in the early 1970s to compute the windward real gas flowfield, the following analytical approach was developed to assess the effects of real gas chemistry on the aerodynamic characteristics of the Orbiter. Since wind tunnel data would not be available to verify the analytical results, Rockwell International/Space Division chose not to include real gas effects in their Aerodynamic Design Data Book [15].

6.1 VISCOUS INTERACTION/REAL GAS PARAMETER STUDY

The general lack of knowledge about the relationship between viscous interaction and real gas effects produced an environment of no practical means, either experimental or

analytical, to study the combined effects of the complex Orbiter geometry at a high angle of attack.

A special NASA Hypersonic Ad Hoc Working Group was formed to investigate the effects of real gas.[2] A priority goal of the Ad Hoc Working Group concentrated on resolving the paradox of using a parameter (e.g., $\bar{V}_\infty'$) to correlate wind tunnel (perfect gas) aerodynamic characteristics and extrapolate to flight conditions with the expectation of replicating real gas effects. Their internal studies—not part of the Rockwell International hypersonic aerodynamic development program being performed by me—concluded that the state-of-the-art in wind tunnel testing and CFD could not conclusively determine the effects of high-temperature gas chemistry on specific vehicle stability and control. They further concluded that the magnitude of real gas aerodynamics fell within the tolerances and variations measured by the wind tunnel data and established in the ADDB. Their effort ended without much success. Coupling the two phenomena with one parameter was questionable since viscous interaction mainly affects skin friction along the surface, and real gas mainly affects pressure on the surface. This implied that wind tunnel-derived C_M might require an adjustment for real gas effects.

I also developed a viscous/gas parameter, but rather than freestream, it was based on sonic line conditions. A slight improvement was observed in correlating the data of AEDC Tunnel F (Test OA-81), the CALSAPN Shock Tunnel (Test OA-113), and the LaRC air, nitrogen, helium, and Freon wind tunnel data. Though potentially promising, it

[2] This researcher was a contributing member of the Ad Hoc Working Group.

was too late in the hypersonic aerodynamic database development to change from $\bar{V}_{\infty}'$. Still, it was an interesting study from an academic viewpoint.

6.2 REAL GAS APPROACH

Knowledge of the effects of real gas dynamics on trimmed performance, stability, and control for a blended, double-delta wing configuration was unsatisfactory in the mid-1970s since there were no practical means, either experimental or analytical, to develop the pitching moment characteristics in the high altitude regime. Therefore, this effort aimed to determine analytically, "Are real gas effects important in the high Mach number/low Reynolds number reentry regime regarding the stability of the Orbiter?" I first obtained insight into the potential real gas effects after evaluating the results from a research effort performed by NASA/LaRC.

Half-Sphere/Cone Geometry

In early 1975, I received from NASA/LaRC aerodynamic data computed by McDonnell Douglas [21 and 22]. The analysis defined the complete flowfield around a 40°, half-sphere/cone geometry, Figure 6.1, for ideal, equilibrium, and nonequilibrium gas cases. Inviscid (pressure) and viscous (skin friction) components of drag, normal force, and pitching moment coefficients were computed by using an inviscid/viscous-perfect/real gas solution coupled at the boundary layer edge by iterating on edge conditions until the mass flow in the boundary layer was equal to the inviscid mass flow between the wall and the inviscid flowfield having the properties corresponding to the edge conditions [20-23]. LaRC's goal was to determine if they could compute and correlate air, nitrogen, helium,

and Freon wind tunnel conditions and perfect, equilibrium, and nonequilibrium flow conditions having the same geometry.

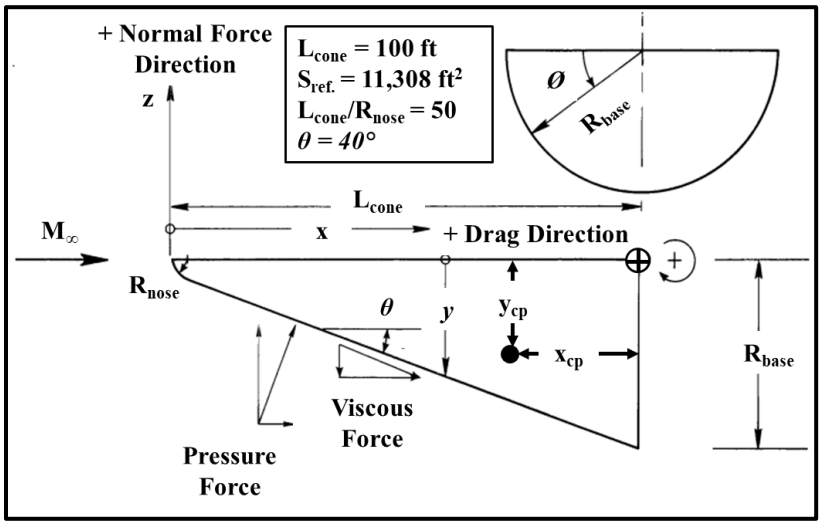

Figure 6.1 LaRC half-sphere/cone model

LaRC correlated viscous interaction and real gas aerodynamics using various correlation parameters. Figure 6.2 shows the pitching moment plotted against $\bar{V}'_\infty$.

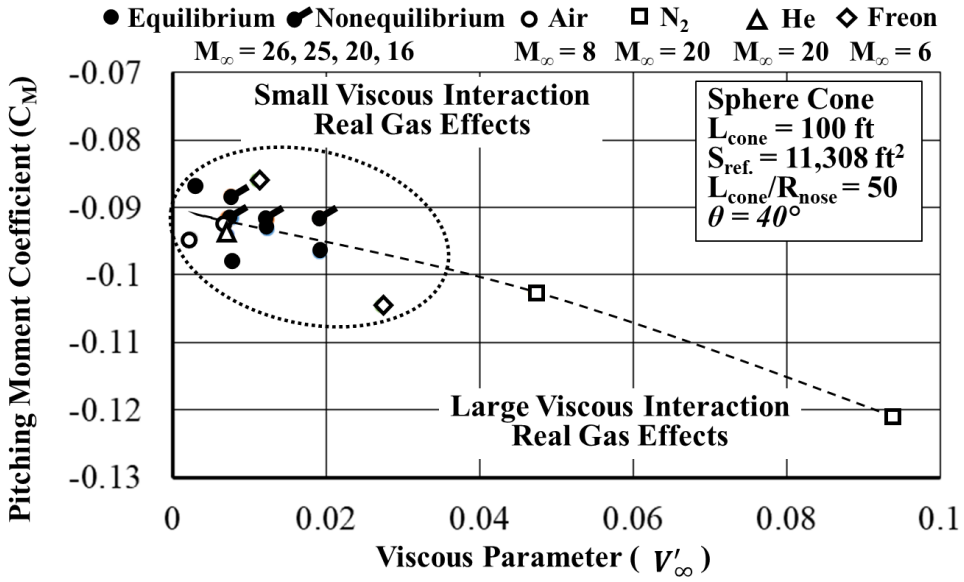

Figure 6.2 Pitching moment data plotted against viscous parameter

However, only a little can be ascertained from this figure regarding the effects of differing gases over a cone. LaRC's effort ended with little success, and they concluded that real gas was not crucial since the scatter of the data was within the scatter of the wind tunnel data.

On the other hand, I concluded that real gas analysis should be continued. Unlike LaRC, I discarded the four simulated wind tunnel computed data as I already determined that one correlation parameter would not correlate viscous interaction and real gas. Next, I changed the center of gravity to the Orbiter center-of-gravity location. Finally, I changed the reference length and reference area to the Orbiter values. Making these conversions, Figure 6.3 shows the resultant incremental pitching moment of the half-sphere/cone's real gas effects, i.e., the difference between ideal gas and real gas.

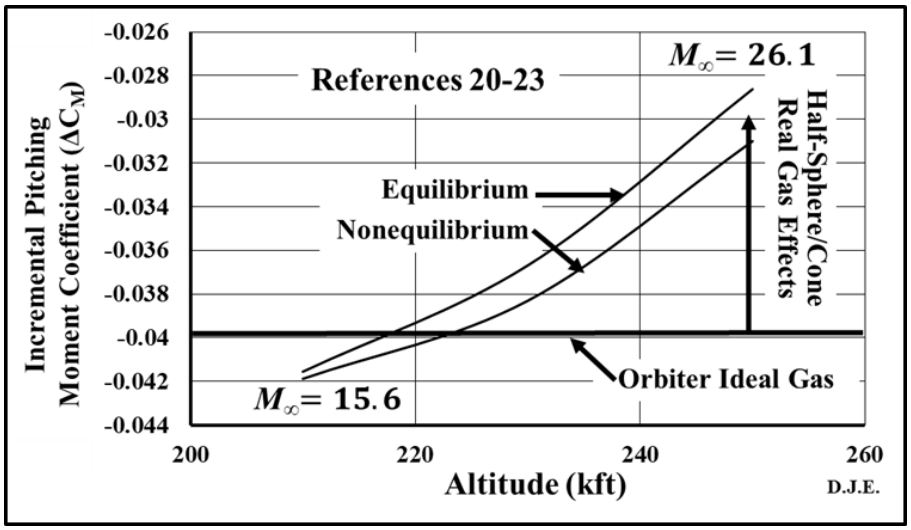

Figure 6.3 Real gas incremental pitching moment coefficients for the half-sphere/cone geometry

The half-sphere/cone data clearly shows a nose-up moment, which validated my first cursory estimate of real gas effects on the Orbiter. Thus, I continued my real gas study. My first assumption was that the incremental pitching moment coefficient changes

proportionally with density due to the difference between perfect gas and real gas effect. This meant there could only be one total vehicle pitching moment for one given altitude and Mach number.

Real Gas Considerations

Analysis of the flow properties over a blunt body in a uniform stream is performed by first solving the energy equation behind the shock. The gas was assumed to be perfect, the flow steady and inviscid, and therefore particle isentropic. The inverse of the density ratio, $\varepsilon = \rho_\infty/\rho$, was not necessarily small compared with unity. And results of the analysis approached the Newtonian values for the limit:

$$\begin{matrix} \gamma \to 1.0, \\ M_\infty \to \infty. \end{matrix} \tag{6.1}$$

For this limit, the gas parameter

$$\lambda = \frac{\gamma - 1}{\gamma + 1}, \tag{6.2}$$

and the inverse of the density ratio, ε, across a normal shock and at the sonic line [38, 39]

$$\varepsilon_{ns} = \lambda - \frac{1 - \lambda}{M_\infty^2}, \tag{6.3}$$

$$\varepsilon_{sl} = 1.6487\ \epsilon_{ns} \left[1 - \frac{\varepsilon_{ns}}{4}\left(2 + \frac{\lambda}{\varepsilon_{ns}}\right)\right], \tag{6.4}$$

approaches zero, the shock standoff distance approaches zero, the shock approaches the body's shape, and the sonic point on the surface approaches the stagnation point. The detailed derivation of solving the energy equation behind the shock for a blunt body is provided in Appendix C.

Real gas behavior deviates from that described by a thermally and calorically ideal gas. This is due to two primary effects: (1) added heat capacity due to excitation of the various degrees of freedom; and (2) change of the average molecular weight of the gas mixture because of dissociation and ionization. For perfect air, λ varies by:

$$0 < \lambda \leq 1/4. \tag{6.5}$$

The lower limit corresponds to an infinite number of internal degrees of freedom of the molecules, while the upper limit represents no internal degrees of freedom (monatomic gas). For a real gas, contributions to the internal energy (and hence λ) by dissociation and ionization were thus accounted for by assuming an "effective λ." Because such an effective λ is a moderate function of temperature and the temperature is almost constant in the subsonic region of the vehicle, then λ is also almost constant. It was thus reasonable to assume that γ would be less than 1.4 for real gas and λ be treated as a constant from the stagnation point to the sonic line.

Many researchers proposed using an ideal gas solution to obtain flowfield results when real gas effects exist. Using an ideal gas solution thus appeared to be adequate to get the stagnation and sonic conditions. For example, Lomax and Inouye [25] suggested that the isentropic exponent[3] for stagnation point calculations is an appropriate γ value for a perfect gas solution. Further, the results by McDonnell Douglas Astronautics Company and Grumman Aerospace Corporation for NASA/LaRC [21-37] indicate that the

[3] In thermal physics and thermodynamics, the heat capacity ratio, also known as the adiabatic index, the ratio of specific heats, or Laplace's coefficient, is the ratio of the heat capacity at constant pressure (C_P) to heat capacity at constant volume (C_V). It is sometimes also known as the isentropic expansion factor and is denoted by γ (gamma) for an ideal gas

differences between perfect gas (γ = 1.12) and equilibrium and nonequilibrium real gas were minor.

The derivation of exact values of γ required rate equations and lengthy numerical calculations. Predictions were generally uncertain since rate constants were imprecisely known at the time. Using all available references, an approximation of γ was derived by curve-fitting the following created database, Figure 6.4. This was not an ideal approach but acceptable for answering the question, "Are real gas effects important regarding the stability of the Orbiter?"

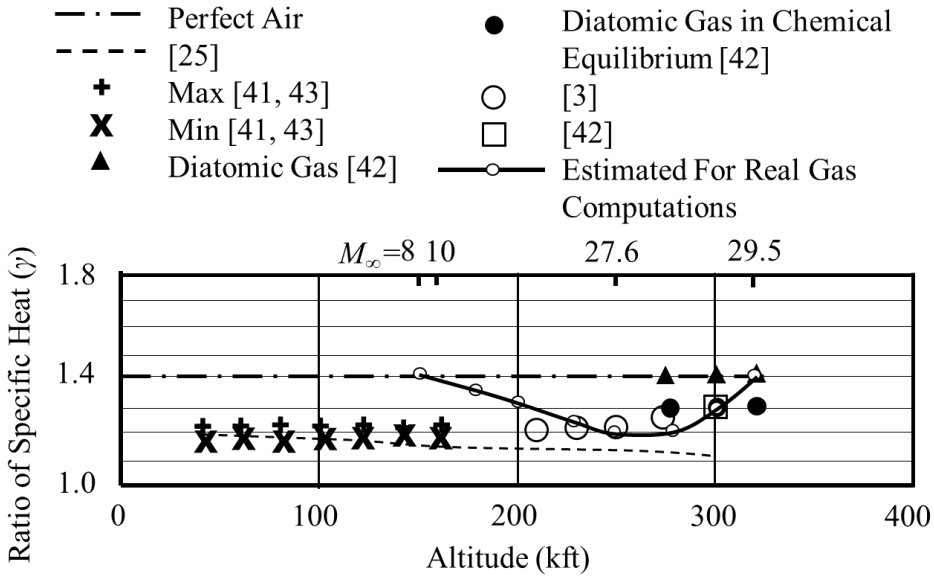

Figure 6.4 Change in the ratio of specific heat

"In most hypersonic applications, the flow has insufficient time to obtain thermodynamic equilibrium. Instead, the flow in the shock layer will generally be nonequilibrium flow. There also exist two limiting cases. Depending on the specific free stream velocity, density, temperature, atmospheric composition, and the absolute size of the body, the flow may be either almost frozen or reach nearly equilibrium," I studied this

under my UAH professor, Rudolf Hermann." Figure 6.5 shows that the flow within the Orbiter shock layer is nonequilibrium real gas, and the boundary layer is laminar until transition; after that, equilibrium real gas and turbulent boundary layer.

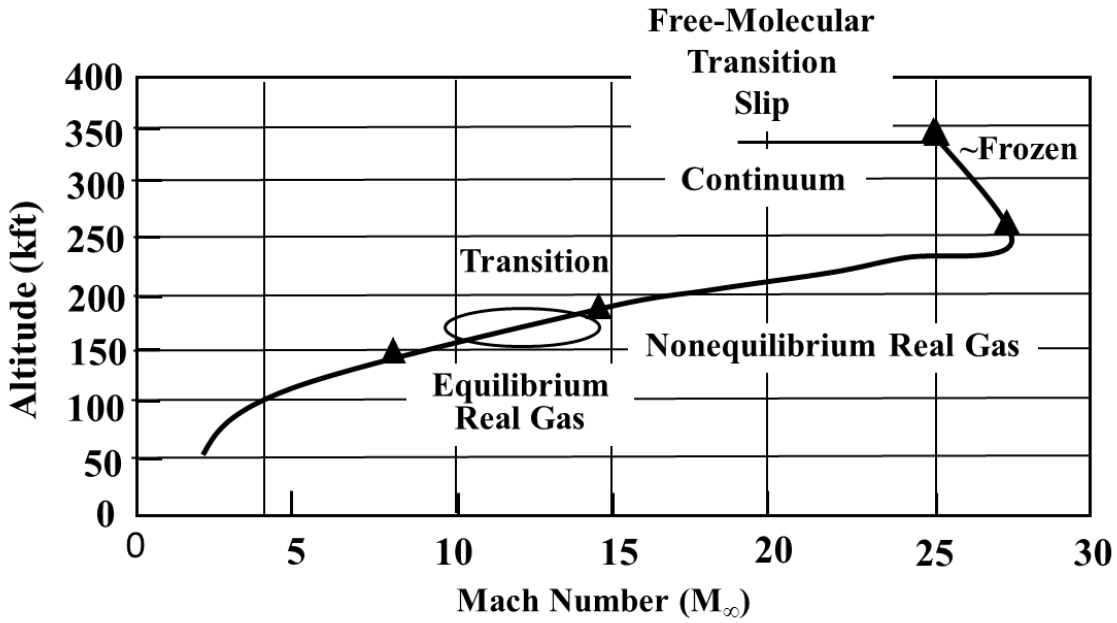

Figure 6.5 Orbiter real gas altitude range

Equations 6.2, 6.3, and 6.4 are plotted in Figure 6.6 as a function of altitude and M_∞. Thus, the assumption made in this analysis is that the change in the pressure (C_P) acting on the surface, and hence the resulting pitching moment, C_M, due to real gas effects, changes proportionally with density at the stagnation point and the sonic line. In other words, for one given inverse of the density ratio, ρ_∞/ρ, there can only be one C_M.

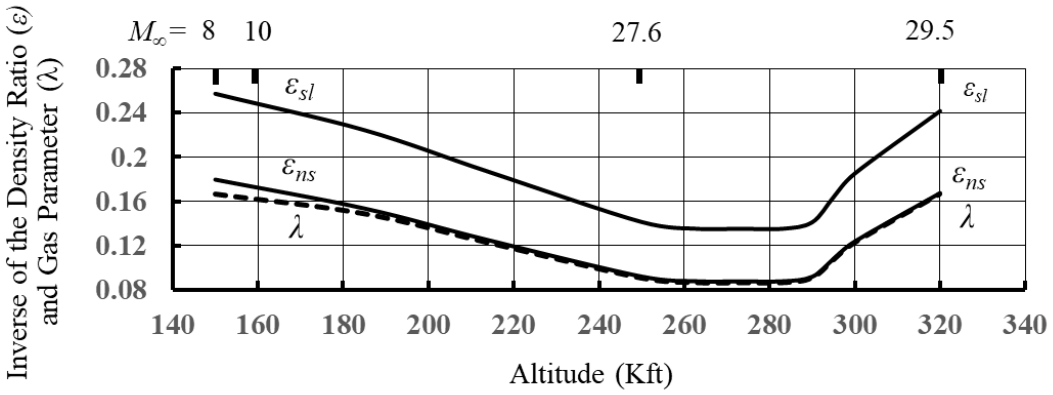

Figure 6.6 Change in the gas parameter and the inverse of the density ratio

The differences in the incremental inverse of the density ratio, Equation 6.6,

$$\Delta\varepsilon = \varepsilon_{Ideal\ Gas} - \varepsilon_{Real\ Gas}, \tag{6.6}$$

taken at the stagnation point and the sonic line, are shown in Figure 6.7.

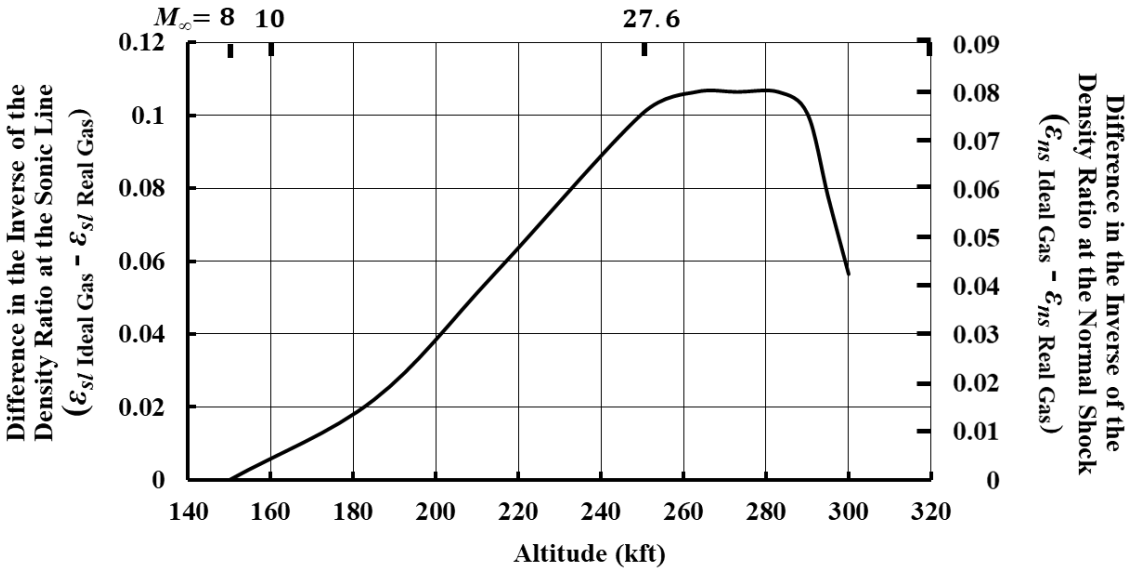

Figure 6.7 Difference in the inverse of the density ratio between perfect and real gas

The ratio of specific heats, γ, can significantly affect the pressure distribution over the lower surface and control surfaces of the orbiter. This is because γ, also the isentropic exponent, directly influences the rate of expansion or compression of the flow. This can

manifest in changing the trim angle of attack from the perfect gas wind tunnel measurements. This is observed in Figure 6.8, where the pressure distribution along the windward side of the Orbiter is calculated for a non-reacting, perfect gas boundary layer (γ = 1.4) and a real gas. The results look very similar, but when integrated over the Orbiter's lower surface, the ideal gas and the real gas pressure distributions induce different stability characteristics.

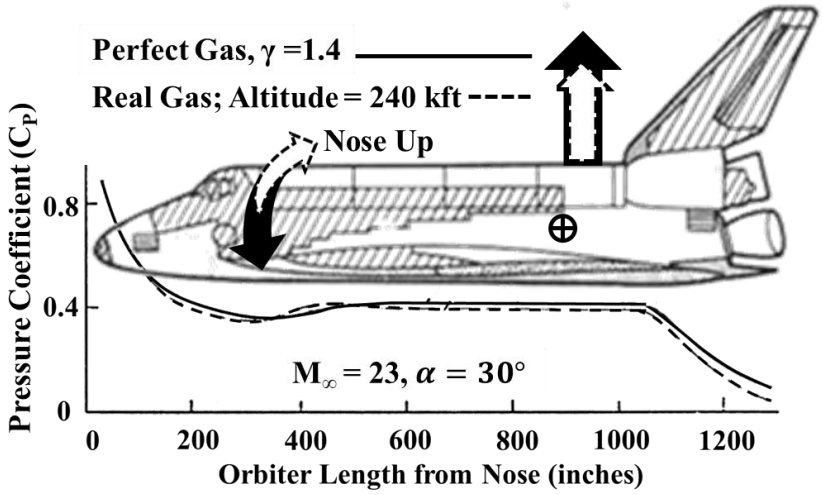

Figure 6.8 Windward centerline pressure distribution

It can be seen that the real gas pressure distribution is slightly lower but has the most significant effect in the after-body region due to the largest surface area. This lower pressure acting aft of the center of gravity induces a nose-up pitching moment. The incremental pitching moment coefficient, Equation 6.7,

$$\Delta C_M = C_{M_{Ideal\,Gas}} - C_{M_{Real\,Gas}}, \tag{6.7}$$

shows this positive moment in Figure 6.9.

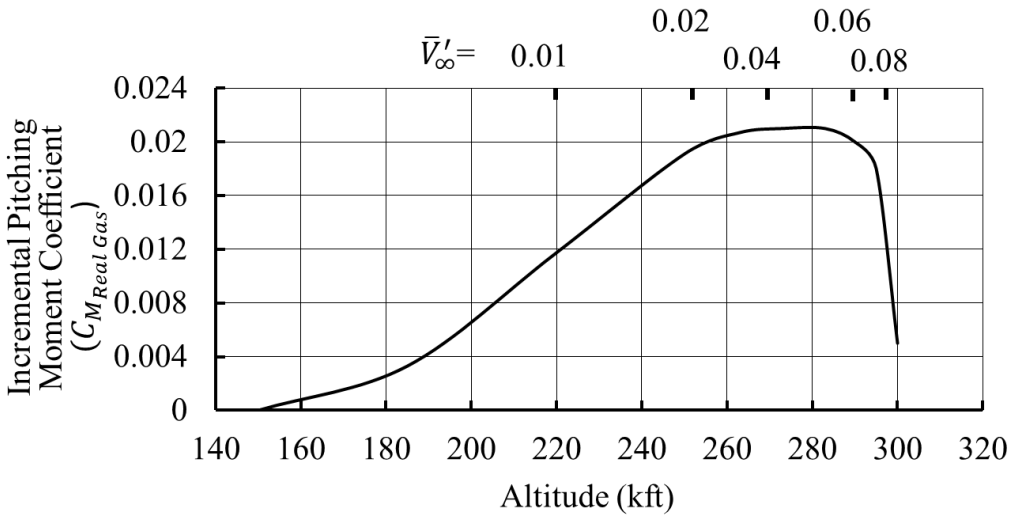

Figure 6.9 Incremental real gas pitching moment coefficient

Further, it can be seen when comparing Figure 6.9 with Figure 6.7 that ΔC_M changes proportionally with ε. This means that for one given ε, there can only be one total vehicle C_M. Finally, it can be assumed that normal force and axial force coefficients, derived from wind tunnel and ideal gas computations, are sufficiently accurate for making preflight predictions. On the other hand, real gas effects must be considered when predicting flight pitching moment.

6.3 ESTIMATED REAL GAS EFFECTS ON PITCHING MOMENT

To correct for real gas effects, the incremental real gas pitching moment coefficient from Figure 6.9 is added to the ideal gas pitching moment coefficient provided in Chapter 5, or

$$C_{M_{Total}} = C_{M_{Ideal\ Gas}} + \Delta C_{M_{Real\ Gas}}, \tag{6.8}$$

Though small, this nose-up increment in pitching moment (i.e., a loss of control effectiveness) is sufficient to force the control surfaces towards maximum positive

deflection—body flap (16.3°) and elevon (15°)—to ensure a stable (negative pitching moment) reentry for the aft center-of-gravity location. Figure 6.10 shows pitching moment coefficients for maximum control surface deflections for both forward and aft center of gravity positions.

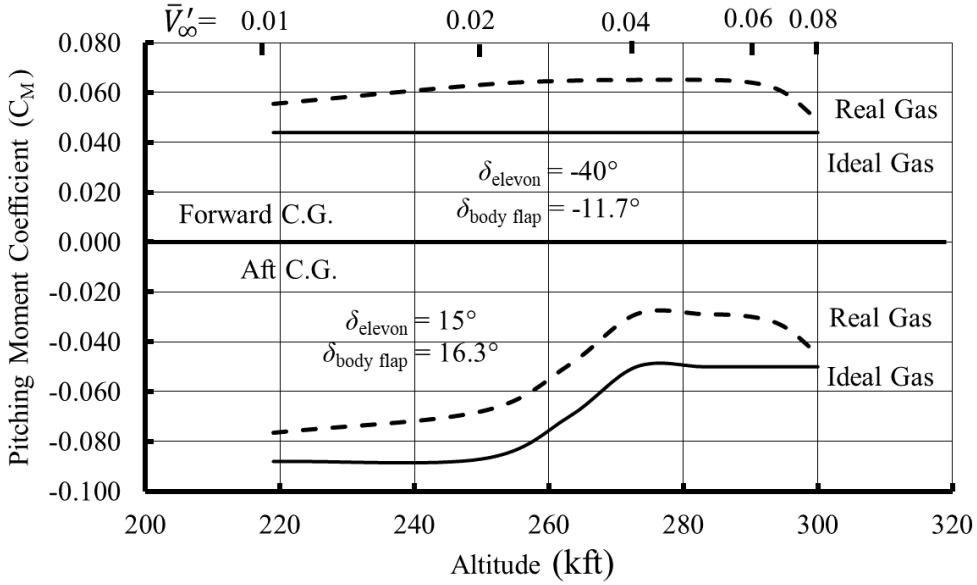

Figure 6.10 Real gas effects on pitching moment coefficient for maximum control surface deflections

Though a destabilizing effect for the aft center-of-gravity location, using full control authority—body flap = 16.3° and elevon = 15°—the Orbiter still trims between 300,000 ft and 260,000 ft.

However, the RI Aerodynamic Design Data Book (ADDB) used the wind tunnel data and thus predicted that a body flap deflection of 8° and an elevon deflection of 5° would be sufficient to produce trim. Figure 6.11 shows what happens if the ADDB-predicted control surface deflections are exposed to real gas (i.e., bringing in Equation 6.8 and Figure 6.9). It can be seen that a severe nose-up pitching moment coefficient is

produced, resulting in the Orbiter unlikely achieving trim above 200,000 ft. And further extending the body flap to 16.3° may be insufficient as the results also indicate instability between 260,000 ft and 290,000 ft. And regardless of the center-of-gravity location, the lower pressure induces a positive (nose-up) pitching moment, nearly doubling the control surface deflections predicted by the ADDB to achieve trim.

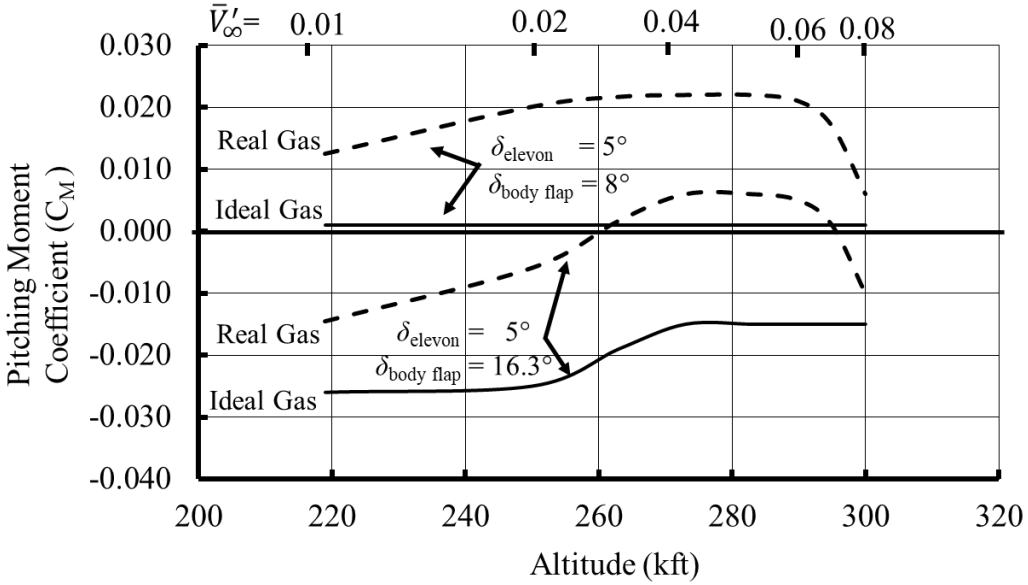

Figure 6.11 Perfect and real gas effects on pitching moment coefficient for the aft c.g. location

These results forewarned of the possibility that the Orbiter might not trim at all for the aft c.g. location. As previously noted, though these analytically derived real gas C_M values raised concern, their verification by wind tunnel tests was impossible. Until additional analysis could be conducted, the author recommended providing a more positive control surface deflection range or reducing the aft c.g. location (e.g., from 0.675L to 0.665L).

NEXT CHAPTER DESCRIPTION

The next chapter, Chapter 7, compares the aerodynamic predictions developed and presented in Chapters 5 and 6 with STS-1 flight data.

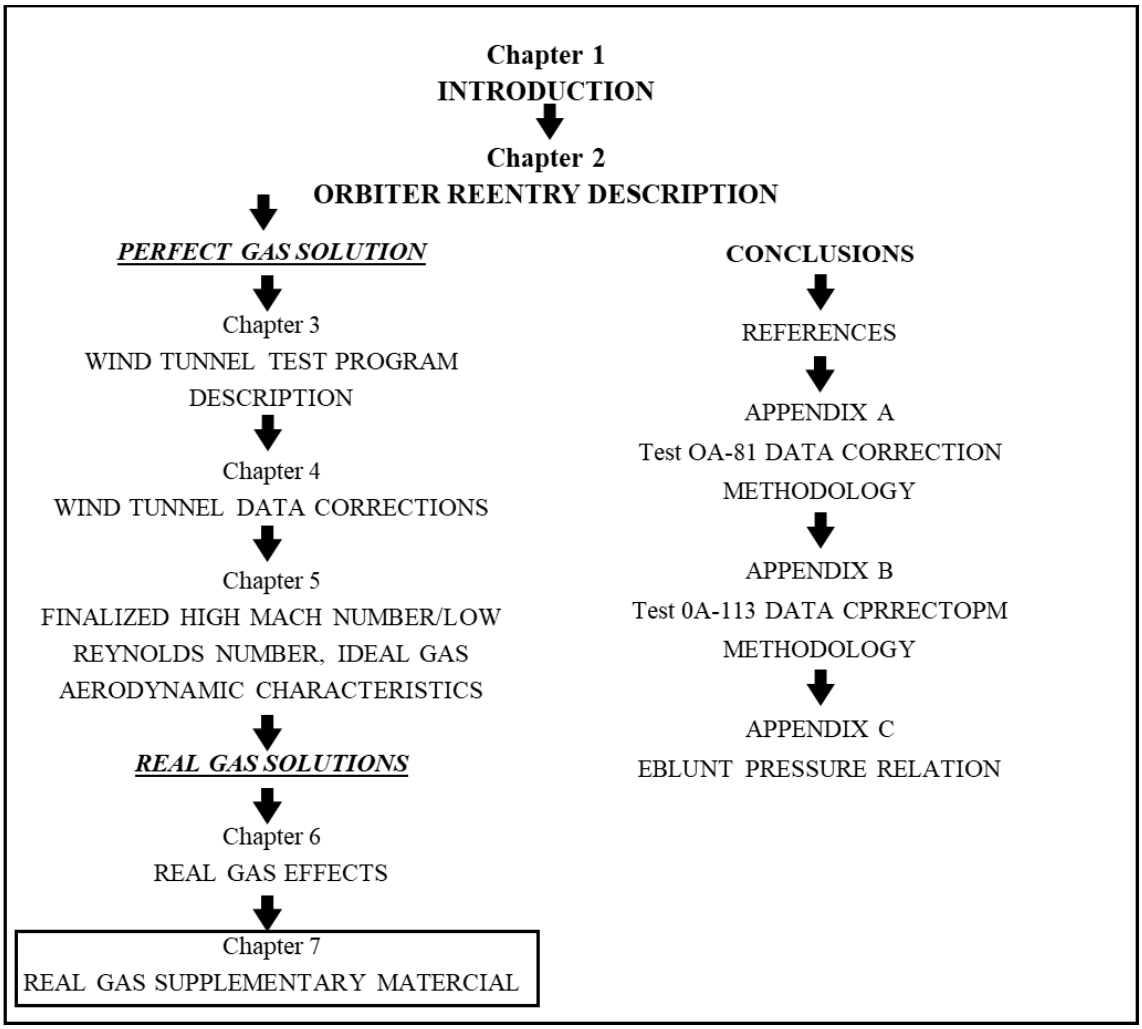

CHAPTER 7

STS-1 SUPPLEMENTARY REAL GAS MEASUREMENTS

This accompanying supplementary material is provided to strengthen and validate the research work documented in this thesis. It compares my 1975-1976 predicted real gas effects presented in Chapter 6 with flight data from the first reentry flight of the Space Transportation System (STS-1), launched on April 12, 1981. Since the flight of STS-1 occurred five years after this thesis was to be completed, the following material should only be considered a supplement. Notwithstanding, it has been included herein to demonstrate that the real gas effects presented in Chapter 6 correctly predicted that the Orbiter would experience a significant nose-up pitching moment requiring the body flap to be deflected down to an angle over twice that predicted by the wind tunnels. This phenomenon became known as the hypersonic "trim anomaly" or "pitching moment anomaly" by post-STS-1 aerodynamicists. Unfortunately, Dr. Brainerd (original thesis advisor) would have had to decide on the quality of Chapter 6 in 1975 without having the flight data presented here.

7.1 PREDICTED AND FLIGHT COMPARISONS

The Space Transportation System (STS-1) was the first orbital spaceflight of the NASA Space Shuttle program. STS-1 was launched on 12 April 1981, and the Orbiter returned to Earth on 14 April 1981. The following compares the aerodynamic predictions

developed in this study with STS-1 flight data. Simulation of hypersonic flow was performed by *v*arying γ, "which was the only tool available for attempting to model real gas chemistry effects."

7.1.1 Axial Force Coefficient

Wind tunnel prediction of C_A is compared with STS-1 flight data in Figure 7.1. Excellent data correlation is observed from 350,000 ft. to approximately the boundary layer transition. The boundary layer transition to turbulent flow below a $\bar{V}_\infty'$ of roughly 0.005. The comparison: (1) validated the methodologies used to correct AEDC's OA81 and CALSPAN's OA113 test data; (2) substantiated the assumption that wind tunnels can reasonably predict pre-flight normal force and axial force coefficients; and (3) proved that $\bar{V}_\infty'$, was a wise choice for a scaling parameter.

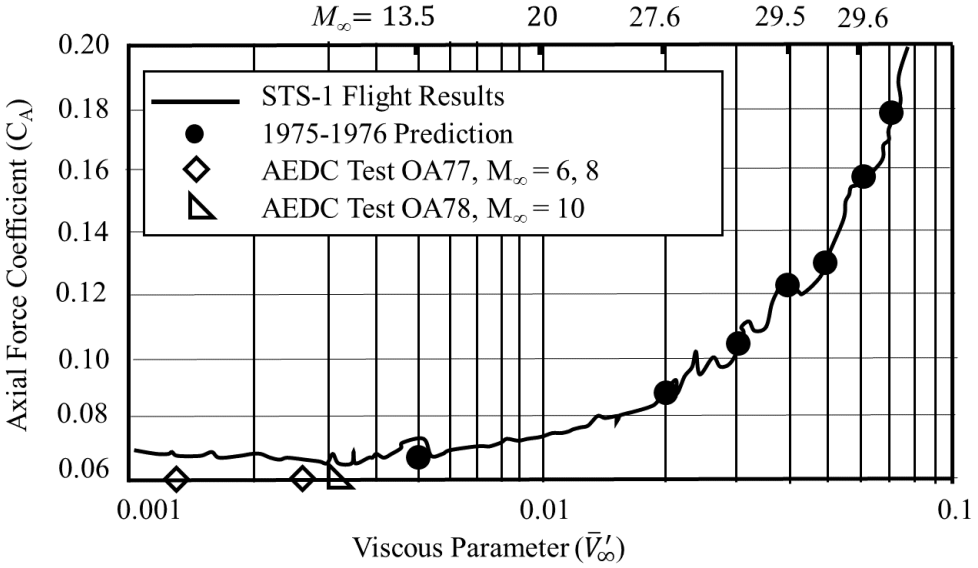

Figure 7.1 Comparison of axial force coefficient

7.1.2 Pitching Moment Coefficient

Real gas-derived C_M estimates are compared with STS-1 flight data in Figure 7.2. It can be seen that the STS-1 body flap and elevon deflections changed continuously along the trajectory seeking body flap and elevon angle combinations to trim. As a result, it can be seen that the flight control surfaces "wander" from 300 kft to 250 kft. The predicted 1975-1976 real gas effects were calculated for constant deflection angles (recall Figure 6.8). When the control surfaces finally became more effective (i.e., $q_\infty \geq 20$ psi), the Orbiter could be trimmed with the body flap at 16° and elevons at -2°. This body flap/elevon configuration was held approximately constant until the Orbiter reached 200 kft.

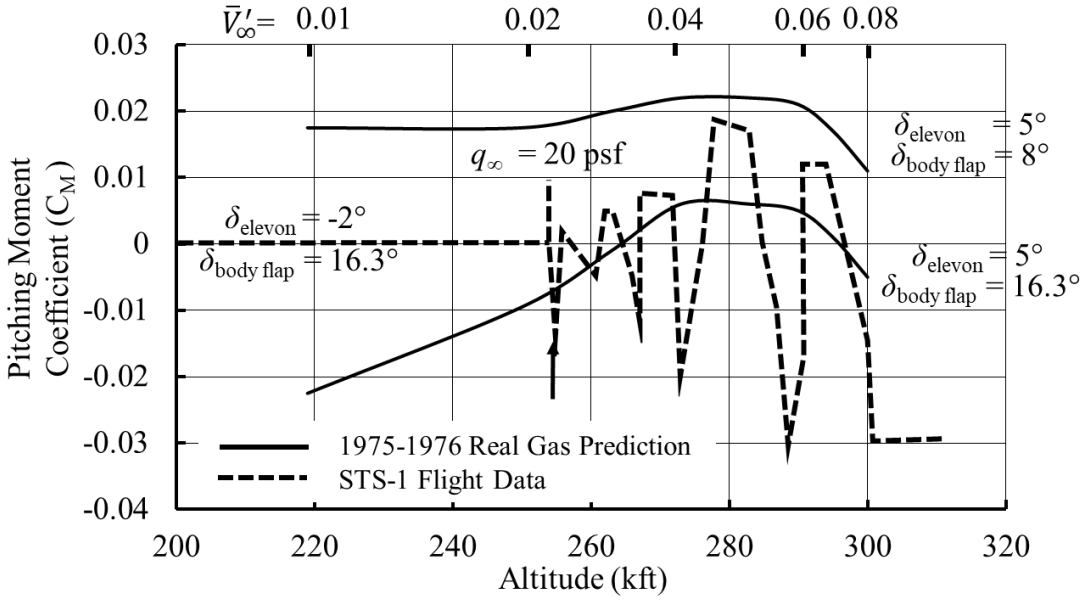

Figure 7.2 Comparison of pitching moment coefficient

These results substantiate the hypothesis that wind tunnel test conditions cannot simulate flight conditions. Also, the real gas pressure distribution is the major contributor to stability compared to the small nose-down, shear moment induced by viscous skin friction. Therefore, the comparison between estimated and flight is reasonable and further

validated that ΔC_M changes proportionally with the inverse of the density ratio, $\varepsilon = \rho_\infty / \rho_{sl}$, taken at the sonic line.

7.1.3 Body Flap Deflection

Real gas-derived body flap deflection is compared with STS-1 flight data in Figure 7.3. To maintain trim, the ADDB [15] preflight prediction specified a body flap deflection of 7.5°. However, the Orbiter's body flap had to be deflected to an angle over twice the ADDB prediction. It can be seen that the real gas estimate matches the Orbiter. The required flap deflection below M_∞ = 18 gradually decreased until the deflection matched the ADDB predictions.

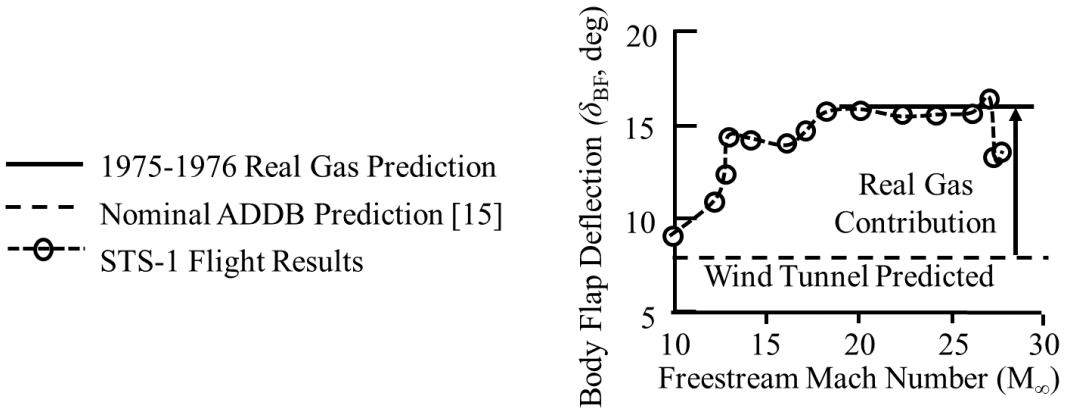

Figure 7.3 Comparison of body flap deflection

7.2 THE SO-CALLED PITCHING MOMENT ANOMALY

In January 1977, the real gas effort (Chapter 6) was discontinued. I was transferred to the L.A. Division (next to the L.A. International Airport) to perform aerodynamic analysis on early scramjet concepts. After that, RI or NASA conducted few, if any, real gas studies on the Orbiter. The following supports this supposition:

1) In 1975 and 1976, NASA/LaRC conducted perfect, equilibrium, and non-equilibrium gas computations on half cones, simple winged lifting shapes, and air, helium, nitrogen, and Freon wind tunnel tests to determine real gas effects. Their analysis indicated that real gas aerodynamics fell within the tolerances and variations established by the ADDB and, thus, reduced or discontinued their efforts [48].
2) In 1979, W. E. Bornemann (Manager, RI Space Shuttle Aerodynamics) and T. E. Surber (Supervisor, RI Orbiter Aerodynamics) chronicled the development of the Orbiter aerodynamic design. However, high-altitude aerodynamics were briefly reviewed without mentioning real gas effects [49].
3) In 1983, a NASA "Lessons Learned" conference addressed the Orbiter's high-altitude performance. Unfortunately, no evidence was presented that NASA/LaRC continued their studies of real gas effects after 1976 [50].

Several NASA Lessons Learned conference presenters observed that the first Orbiter (STS-1) had to deflect the body flap over twice the ADDB prediction (7° to 16°) to maintain trim. Not aware of my 1975-1976 real gas analysis, post-STS-1 aerodynamicists incorrectly dub this difference a hypersonic "pitching moment anomaly." This anomaly was attributed to many phenomena, including viscous effects, diminished body flap effectiveness, Mach number effects, and real gas effects. Only after 1983, when CFD codes began to improve, was the hypersonic pitching moment anomaly recognized as a real gas phenomenon.

However, the results presented herein showed that the nose-up pitching moment was a normal response caused by a relatively small pressure differential acting on the aft,

windward surface of the Orbiter, which has a vast surface area. The primary cause of this lower pressure was a lower ratio of specific heat induced by higher temperature effects.

7.3 Real Gas Dissociation

To compare my work in the mid-1970s and today's knowledge base, Dr. Jason Cassibry, my current thesis advisor, requested that I include N_2 and O_2 dissociation data on the Orbiter hypersonic regime. Figure 7.4 displays the temperature ranges of vibrational excitation and chemical reactions of air [51]. And Figure 7.5 shows the Orbiter trajectory from Figure 6.5 overlay the changing air/altitude regions from [51]. It can be seen that the gas around the vehicles exhibits different characteristics at various altitudes. Surprisingly, my 1975 results in Figure 6.5 compare well with these 2022 assessments. The approximate altitudes for (1) noncontinuum and continuum flow regimes and (2) nonequilibrium and equilibrium flow regimes agree.

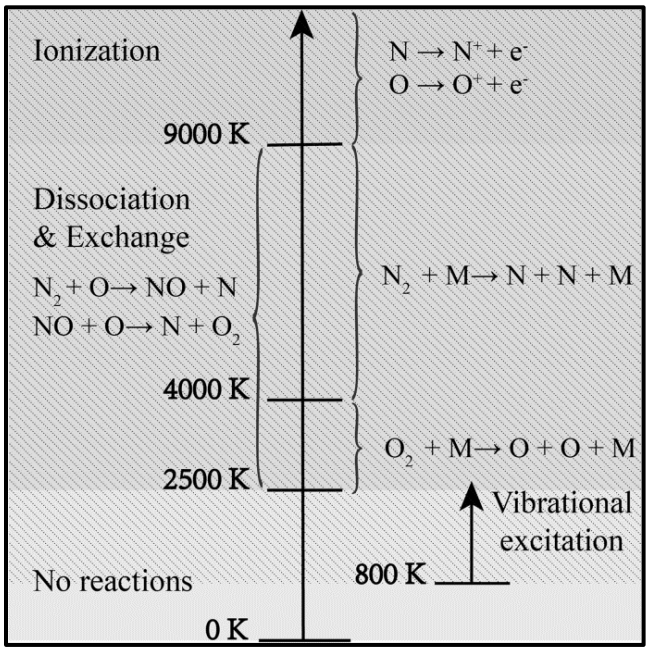

Figure 7.4 Temperature ranges of vibrational excitation and chemical reactions in the air

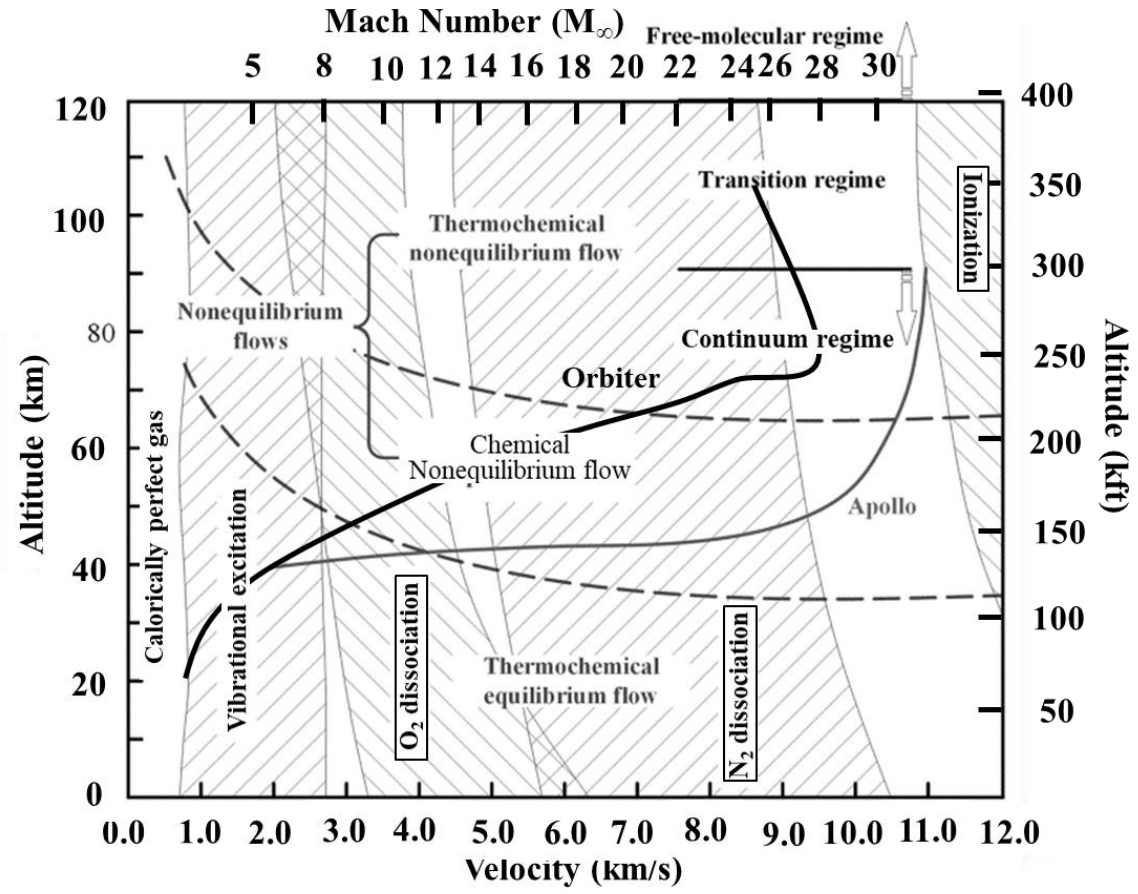

Figure 7.5 How the air around the Orbiter changes with altitude

NEXT SECTOPM DESCRIPTION

The following section provides the conclusions of the development of high Mach number/low Reynolds number aerodynamic characteristics for a blended, double-delta wing configuration (aka, NASA/Rockwell Space Shuttle Orbiter).

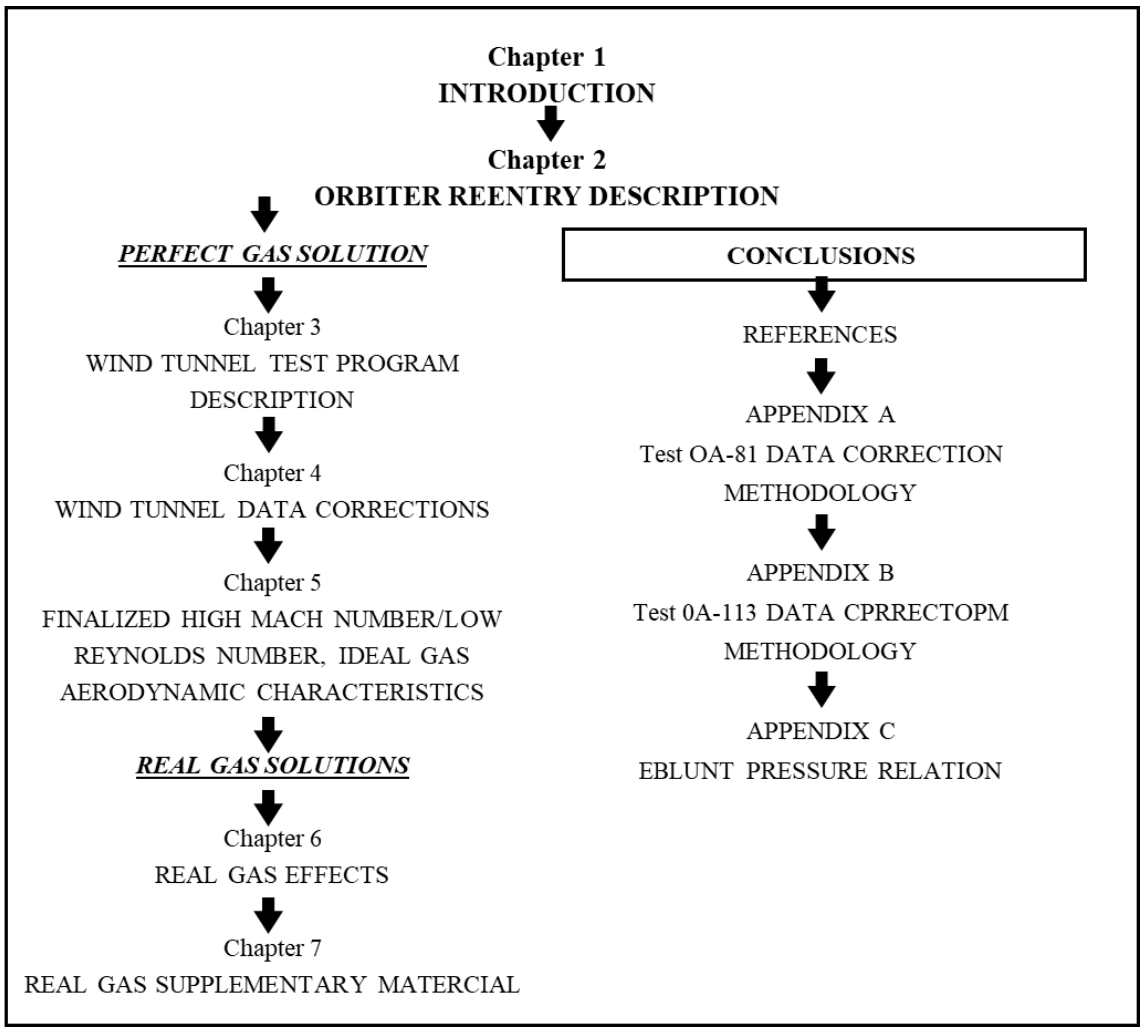
Chapter 1
INTRODUCTION
Chapter 2
ORBITER REENTRY DESCRIPTION
PERFECT GAS SOLUTION
Chapter 3
WIND TUNNEL TEST PROGRAM
DESCRIPTION
Chapter 4
WIND TUNNEL DATA CORRECTIONS
Chapter 5
FINALIZED HIGH MACH NUMBER/LOW
REYNOLDS NUMBER, IDEAL GAS
AERODYNAMIC CHARACTERISTICS
REAL GAS SOLUTIONS
Chapter 6
REAL GAS EFFECTS
Chapter 7
REAL GAS SUPPLEMENTARY MATERCIAL
CONCLUSIONS
REFERENCES
APPENDIX A
Test OA-81 DATA CORRECTION
METHODOLOGY
APPENDIX B
Test 0A-113 DATA CPRRECTOPM
METHODOLOGY
APPENDIX C
EBLUNT PRESSURE RELATION

CONCLUSIONS

The presented results comprise a compendium of hypersonic research in solving the technical challenges of developing the NASA Space Shuttle Orbiter's high Mach number/low Reynolds number aerodynamic characteristics. Because theoretical prediction methodologies had limited applicability for complex geometries in the 1970s—e.g., Orbiter's blended, double-delta wing configuration—it was understood at the program's start that deriving the hypersonic aerodynamics—inviscid/viscous and perfect/real gas flow—would be a challenging undertaking. In addition, a conventional flight test program of slowly and cautiously approaching more severe flight conditions (e.g., the Saturn/Apollo program started with unmanned flights and eventually to manned flights) was not possible as the first Orbiter flight would be manned. Thus, the Orbiter reentry program required the aerodynamicist to take a new but unproven approach to determine flight characteristics.

CON.1 WIND TUNNEL / IDEAL GAS

Four wind tunnels and a three-dimensional digital computer program system developed a perfect gas aerodynamic database.

Unfortunately, AEDC Tunnel F and CALSPAN 48-in tunnels produced poor-quality data that required "significant corrections." The causes included: contaminated flow by copper, tungsten, and beryllium dust particles; incorrect dynamic pressure measurements; misalignment of nozzle parts; nozzle non-uniformities; source flow; and flow irregularities. A rigorous effort was conducted to correct the wind tunnel

measurements and thus successfully salvage the usefulness of the tests. The theoretical ideal gas aerodynamic characteristics—calculated by the Hypersonic Arbitrary Body Aerodynamic Computer Program—compared exceptionally well with the corrected wind tunnel measurements. The Orbiter's corrected wind tunnel longitudinal aerodynamic characteristics were correlated to single curves by the well-known viscous parameter (Chapters 4 and 5) and documented in Rockwell International's 1975 and 1976 Substantiation Reports and Aerodynamic Design Data Books. Thus, the essential part of the research for Dr. J. J. Brainerd's approval was completed.

CON.2 REAL GAS

Real gas estimations (Chapter 6) were derived by solving the energy equation behind the shock. The gas was assumed to be perfect, the flow steady and inviscid, and the ratio of specific heat varied with velocity and altitude. Using effective ratios of specific heat, which was the only tool available for attempting to analyze real gas effects on the actual Orbiter configuration, appears to compute a meaningful nose-up pitching moment coefficient—for the aft center of gravity location—that exceeded the established tolerances and variations established by the Aerodynamic Design Data Book. In addition, the body flap had to be deflected over twice the wind tunnel predictions. Though disconcerting, the study was terminated early in 1977 because real gas wind tunnels were nonexistent for verification. Despite this, the effort to include preliminary real gas effects in the thesis was successfully estimated for the first time for a complex configuration at a high angle of attack.

CON.3 SUBSTANTIATIONS OF THE INITIAL HYPOTHESES

STS-1 flight data validated the eight hypotheses defined at the start of this effort (Introduction, page 9).

1. Viscous interaction showed a negligible effect on the normal force coefficient.
2. Viscous interaction mainly affected the shear and axial force coefficient.
3. Viscous interaction induced a significant degradation in the lift-to-drag ratio.
4. An increased axial force coefficient due to viscous interaction induced a nose-down pitching moment, thereby increasing stability. But it had little effect countering the stronger nose-up pitch due to the real gas effect.
5. Normal force and axial force coefficients derived from wind tunnels and perfect gas computations were sufficiently accurate for making preflight predictions.
6. The well-known viscous parameter was suitable for correlating high Mach number/low Reynolds number normal force and axial force data from the wind tunnel data and the HABP computations.
7. Real gas chemistry changed the body's pressure distribution and hence changed the pitching moment, resulting in the need for correcting the ideal gas pitching moment values.
8. The pressure distribution over the entire lower surface changed proportionally with the inverse of the sonic density ratio during reentry; i.e., only one pressure distribution can exist for only one sonic line condition.
9. Real gas effects on stability gets worse with increasing altitude and velocity.

The STS-1 flight data validated the longitudinal aerodynamic characteristics (Chapters 4, 5, and 6). In addition, it further validated the assumption that coupling the

two phenomena, viscous interaction and real gas, with one parameter, as NASA proposed, was mistaken since viscous interaction mainly affects skin friction along the surface, and real gas affects pressure on the surface because of high temperatures. However, this is not to say that the two phenomena do not interact. Still, such an interaction was not detectable based on the computational limitations of this effort. Therefore, such measurements wait for CFD calculations. The flight data did verify that the wind tunnel test conditions could not duplicate flight conditions regarding the pitching moment. Thus, the measurement of the wind tunnel pitching moment had to be adjusted using real gas computations.

The STS-1 flight data further verified this thesis candidate's assumption that the pressure distribution over the entire lower surface changed proportionally with the inverse sonic density ratio during reentry; i.e., only one pressure distribution and hence pitching moment can exist for only one sonic line condition.

CON.4 LESSONS LEARNED

It is still astonishing to look back to 1961—when I first started working as a summer student for NASA/MSFC Aerodynamic Design Branch—and witness the rapid development of hypersonic flight systems, from early RVs and lifting bodies to hypersonic scramjets and projectiles. The challenge has always been to build on past experience and develop a new flight vehicle generation. The main interest, like the Space Shuttle Orbiter reentry, is on sustained and controlled hypersonic flight, whether for civil or military applications.

The high Mach number/low Reynolds number regime characterized by the viscous interaction flowfield is the same regime where real gas dynamics occur in flight. Therefore,

many aerodynamicists in the 1970s had difficulty distinguishing between low-density and real gas effects. Interestingly, the UAH/UA coursework taken under Brainerd, Hermann, and Doughty contributed to the approach taken in this thesis advancing a solution— as a prelude to CFD capabilities—that considered two phenomena simultaneously that affected the Orbiter performance characteristics differently: (1) an increase in skin friction and hence axial force (viscous interaction) and (2) a change in the pressure distribution and hence pitching moment (real gas).

Over the years, I investigated many military reentry concepts requiring control surface deflections, significant maneuvers, and large pull-ups. The most recent example of using the technology developed in this thesis is the mini-Orbiter, better known as the X-37. The X-37, and the more recent X-37B, is one of the world's newest and most advanced reentry spacecraft, designed to operate in low-earth orbit, 150 to 500 miles above the earth. In addition, the vehicle is the first since the Space Shuttle with the ability to return experiments to Earth for further inspection and analysis. NASA's original X-37 program began in 1999 and continued until September 2004, when NASA transferred the program to DARPA and, after that, to the USAF. Between 2002 and 2003, I took over the aerodynamic technical manager's responsibility in Huntington Beach, CA, to move the concept from the already successful X-37 drop and landing tests to developing the reentry flight performance characteristics similar to the original Orbiter but with CFD codes. My contribution seemed helpful as the X-37B has reentered the atmosphere successfully many times.

In addition to Earth's entries/reentries, missions to other planets, where many entry speeds into those atmospheres are going to be greater than on Earth, are on the horizon.

Though the atmospheres differ, each has to be examined as a function of velocity, density, and properties. For example, I recall spending six months working on a Viking Mars Lander proposal to be submitted to NASA in early 1969. Entry and descent comprised four phases: (1) deorbit burn, (2) atmospheric entry with peak heating occurring a few seconds after the start of the Martian entry, (3) parachute deployment, and (4) retrorockets to slow descent with a soft landing. I was involved in phase 2. However, the Jet Propulsion Laboratory/Martin Marietta won the contract. Another entry undertaking into another planet's atmosphere was the Galileo probe to Jupiter, designed to enter the Jovian atmosphere at 60 km/s, an altitude of 1000 km, and an atmosphere H2 and He at a mixture of 89:11 by mass (D.G. Fletcher, "*Fundamentals of Hypersonic Flow-Aerothermodynamics"*). The point is that problems, like the Orbiter in 1973, will always seem unsolvable initially but are solvable with effort and enthusiasm.

Since the approach developed herein to developing the hypersonic aerodynamic characteristics of the Orbiter has been replaced with advanced CFD capabilities and improved wind tunnels, its usefulness is its historical value by showing young aerospace engineering students how the technology has evolved from the first semi-empirical (Newtonian) equation that the candidate used in 1961 to the use of advanced CFD codes.

NEXT SECTION DESCRIPTION

The following references includes those in the main body of the manuscript and the following Appendixes.

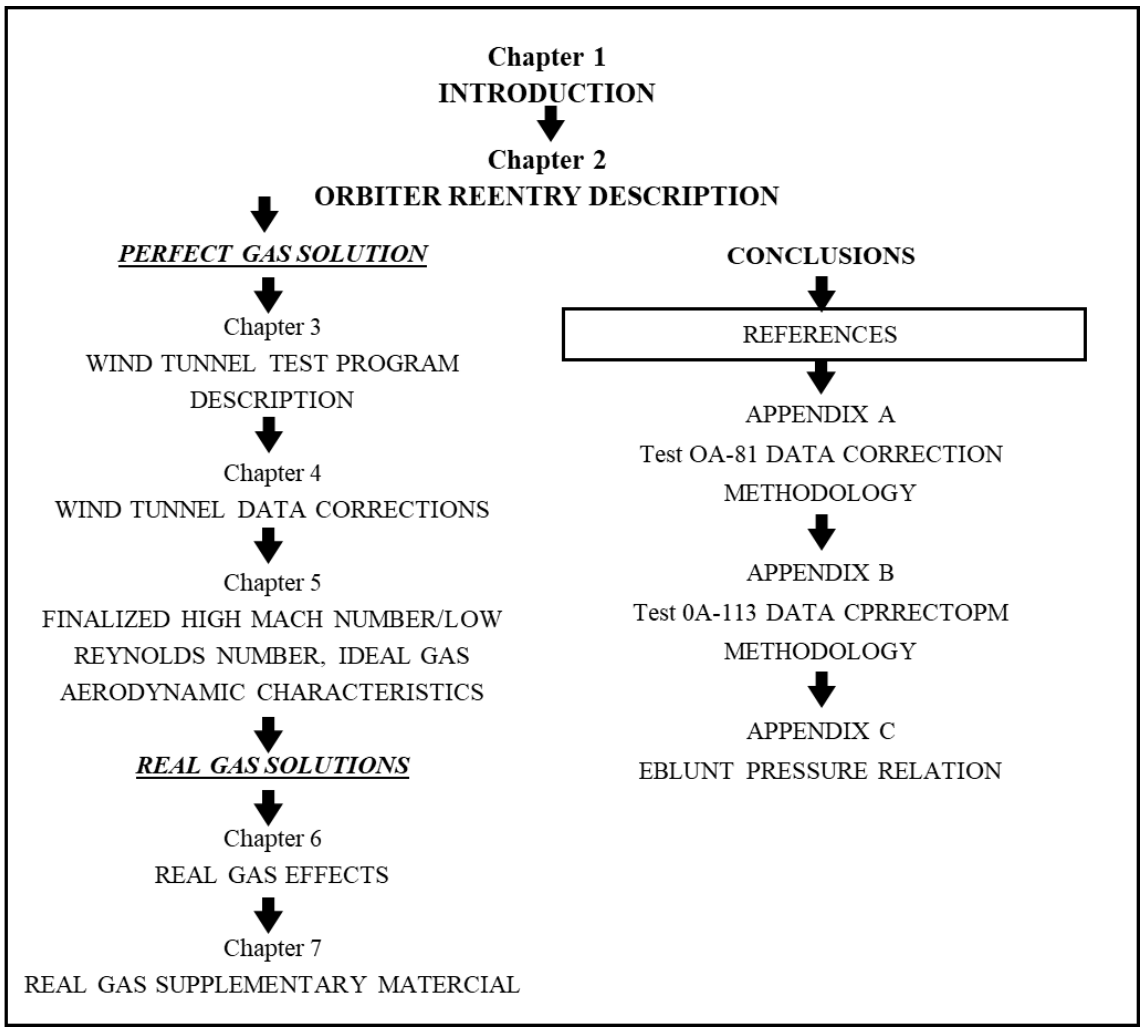
Chapter 1
INTRODUCTION
Chapter 2
ORBITER REENTRY DESCRIPTION
PERFECT GAS SOLUTION
Chapter 3
WIND TUNNEL TEST PROGRAM
DESCRIPTION
Chapter 4
WIND TUNNEL DATA CORRECTIONS
Chapter 5
FINALIZED HIGH MACH NUMBER/LOW
REYNOLDS NUMBER, IDEAL GAS
AERODYNAMIC CHARACTERISTICS
REAL GAS SOLUTIONS
Chapter 6
REAL GAS EFFECTS
Chapter 7
REAL GAS SUPPLEMENTARY MATERCIAL
CONCLUSIONS
REFERENCES
APPENDIX A
Test OA-81 DATA CORRECTION
METHODOLOGY
APPENDIX B
Test 0A-113 DATA CPRRECTOPM
METHODOLOGY
APPENDIX C
EBLUNT PRESSURE RELATION

REFERENCES

1 Gentry, A. E., "*Hypersonic Arbitrary Body Aerodynamic Computer Program*," DAC 61552, Douglas Aircraft Co., Inc, Santa Monica, California, April 1968.

2 Tsien, H. S., "*Superaerodynamics, Mechanics of Rarefied Gases*," Journal of Aeronautical Sciences, pp. 652-664, December 1946.

3 Lees, L., and Probstein, "*Hypersonic Viscous Flow Over a Flat Plate*," Dept. of Aero Engineering, Princeton Univ., Princeton, New Jersey, 1952.

4 Hermann, R., "*Problems of Hypersonic Flight at the Re-Entry of Satellite Vehicles*," Reprint from Sixth International Astronautical Congress, Amsterdam, 1958.

5 Bertram, M. H., and Henderson, A., Jr., "*Effects of Boundary Layer Displacement and Leading Edge Bluntness on Pressure Distribution, Skin Friction and Heat Transfer of Bodies at Hypersonic Speeds*," NACA TN 4301, July 1958.

6 Bertram, M. H., "*Boundary Layer Displacement Effects in Air at Mach Numbers of 6.8 and 9.6*," NASA TR R-22, 1959.

7 Dorrance, W. H., "*Viscous Hypersonic Flow*," McGraw Book Co., New York, 1960.

8 Truitt, T. W., "*Fundamentals of Aerodynamic Heating*," The Ronald Press Co., New York, 1960.

9 Whitfield, J. D., and Griffith, B. J., "*Hypersonic Viscous Drag Effects on Blunt Slender Cones*," AIAA Journal, Vol. 2, No. 10, October 1964.

10 Sieron, T. R., and Martinez, C., Jr., "*Effects and Analysis of Mach Number and Reynolds Number on Laminar Skin Friction at Hypersonic Speeds*," AFFDL-TR-65-5, April 1965.

11 Nagel, A. L., and Thomas, A.C., "*Analysis of the Correlation of Wind Tunnel and Ground Test Data to Flight Test Results*," AIAA/NASA Flight Testing Conference in Huntsville, Alabama, February 15-17, 1965.

12 Bertram, M. H., *Hypersonic Laminar Viscous Interaction Effects on the Aerodynamics of Two-Dimensional Wedge and Triangular Planform Wings*," NASA TN D-3523, August 1966.

13 Liepmann, H. W., and Roshko, A., "*Elements of Gasdynamics*," John Wiley and Sons, Inc., New York, May 1967.

14 John, J. E. A., "*Gas Dynamics*," Allyn and Bacon, Inc., Boston, 1969.

15 *"Aerodynamic Design Data Book, Orbiter Vehicle – Volume 1*," SD 74-SH-0060-1J, Rockwell International/Space Division, Downey, CA, Dec 1975.

16 Elder, D. J., "*Status of Orbiter Hypersonic Studies*," Rockwell International/Space Division, SAS/AERO/76-315, Downey, California, November 1976.

17 Elder, D. J., "*Experimental Investigation of the Hypersonic Viscous Interaction Effects on the Shuttle Orbiter Vehicle Obtained in the CALSPAN Hypersonic Facility*," Rockwell International/Space Division, SAS/AERO/76-283, Downey, California, May 23, 1975.

18 Burt, R. H., and Jones, J. H., "*Static-Force and Moment Tests of a 0.015-Scale Rockwell International Space Shuttle Orbiter Model at Mach Number 6, 8 and 10*," AEDC-DR-74-20, February 1974.

19 Siler, L. G., and Coats, "*Static Stability and Axial Force Characteristics of the NASA STS 0.01-Scale Model (51-0) of the Vehicle 4 Orbiter at Mach Numbers 16 and 20 (Test 0A81)*," AEDC-DR-74-25, March 1974.

20 Burrows, R. R., and Rogers, C. E. "*Wind Tunnel Test OA113 of the 0.01-Scale Space Shuttle Orbiter Model 51-0 in the CALSPAN Hypersonic shock Tunnel (48-inch Leg)*," DMS-DR-2234, NASA-CR-141,547, July 1975.

21 Jones, R. A., and J. L. Hunt, "*Investigation of Orbiter Real-Gas Effects on Viscous and Inviscid Drag, Pitching Moment and Interaction Effects*," HSAD-NASA-Langley, October 1974.

22 Fivel, H. J., "*Calculated Results and Correlation of Real gas Effects on Orbiter Skin Friction Drag*," McDonnell Douglas Astronautics Company-East, Copy sent to Bill Woods, NASA Langley, July 9, 1975.

23 Fivel, H. J., Masek, R. V., and Mockapetris, L. J., "*Analytical Comparison of Hypersonic Flight and Wind Tunnel Viscous/Inviscid Flow Fields*," NASA CR-2489, 1975.

24 Hunt, J. L., Jones, R. A., and W.C. Woods, "*Investigation of Real-Gas and Viscous Effects on the Aerodynamic Characteristics of a 40 Degree Half-Cone With Suggested Correlations of the Shuttle Orbiter,"* NASA TN D-8418, June 1977.

25 Lomax, H. and M. Inouye, "*Numerical Analysis of Flow Properties About Bodies at Supersonic Speeds in an Equilibrium Gas*," NASA TR R-204, July 1964.

26 Curtis, J. T., and C. R. Strom, "*Computations of the Nonequilibrium Flow of a Viscous, Radiating Fluid About a Blunt Axisymmetric Body, Volume 1: Equations and Results,*" AFFEDL-TR-67-40, June 1967.

27 Cebeci. T., Smith, A. M. O. and L D. Wang, "*A Finite-Difference Method for Calculating Compressible Laminar and Turbulent Boundary Layers*," DAC-67131, Part 1, McDonnell Douglas, March 1969.

28 Cebeci. T., Smith, A. M. O. and G. Mosinskis, "*Calculation of Compressible Adiabatic Turbulent Boundary Layer*," AIAA Paper No. 69-687, June 1969.

29 Blottner, F. G., "*Chemical Nonequilibrium Boundary Layer*," AIAA Paper No. 63-443, August 1963.

30 Hamilton, H., Langley Research Center, provided this researcher with early calculations on a modified 140C Orbiter later published by Marconi, Salas, and Yaeger in the following references [30, 31].

31 Marconi, F., Salas, M., and L. Yaeger, "*Development of a Computer Code for Calculating the Steady Super/Hypersonic Inviscid Flow Around Real Configurations,*" Volume I, Computational Technique. NASA CR-2675, 1976.

32 Marconi, F., Salas, M., and L. Yaeger, "*Development of a Computer Code for Calculating the Steady Super/Hypersonic Inviscid Flow Around Real Configurations,*" Volume II, Code Description, NASA CR-2676, 1976.

33 Moretti, G, and G. Bleich, "*Three-Dimensional Flow Around Blunt Bodies*," AIAA Journal 5, 1966.

34 Moretti, G., Grossman, B., and F. Marconi, *"A Complete Numerical Technique for the Calculation of Three-Dimensional Inviscid Supersonic Flows,"* AIAA Paper No. 72-192, 1972.

35 Moretti, G., *"Thoughts and Afterthoughts about Shock Computations,"* PIBAL Report No. 72-37, 1972.

36 Moretti, G., and M. Pandolfi, *"Entropy Layers" Journal Computers and Fluids,"* January 19, 1973.

37 Moretti, G. and M. Pandolfi, "*Analysis of the Inviscid Flow about a Yawed Cone*," Preliminary studies, PIBAL Report No. 72-18, 1972.

38 Brainerd, J. J., "*Thin Oblique Gasdynamic Shock Waves*," UARI Research Report No. 45, the University of Alabama in Huntsville, Huntsville, Alabama, June 1967.

39 Brainerd, J. J., and W. R. Waldrop, "*The Plasma Sheath in the Nose Region of Selected Reentry Bodies,*" UARI Research Report No. 60, the University of Alabama in Huntsville, Huntsville, Alabama, June 1968.

40 Chen, T. Y., "*Real Gas Flow Fields About Entry Orbiter*," SAS/AERO/74-734, Rockwell International/Space Division, October 1974.

41 Feldman, S., "*On Trails of Axisymmetric Hypersonic Blunt Bodies Flying Through the Atmosphere*," JAS, Vol. 28, pp. 433-448, June 1961.

42 Cheng, H. K., "*The Blunt-Body Problem in Hypersonic Flow at Low Reynolds Number*," CAL Report No. AF-1285-a-10, Cornell Aeronautical Laboratory, Inc., Buffalo, NY, June 1963.

43 Hanson, C. F., "*Approximation for the Thermodynamic and Transport Properties of High Temperature Air*," NASA TR R-50, 1959.

44 Elder, D. J., "*An Evaluation of the AEDC Correction Procedure to Test OA-81 Tunnel F Contaminated Data*," IL No. SAS/AERO/74-350, Rockwell/Space Division, Downey, May 1974.

45 Sievon, T. R., and C. Martinez, Jr., "*Effects and Analysis of Mach Number and Reynolds Number on Laminar Skin Friction at Hypersonic Speeds*," AFFDL-TR-65-5m Wright Patterson Air Force Base, Ohio, April 1965.

46 Elder, D. J., "*Response to Aerodynamic Performance Panel Meeting August 1975-Action Item 8/26-20*," Rockwell/Space Division, Downey, October 1975.

47 Elder, D. J., "*Viscous Contribution to the Total Aerodynamic Characteristics of a Typical Shuttle Spacecraft Configuration at Hypersonic Speeds*," T.M. 54/20-279, Lockheed Missiles and Space Co., Inc., Huntsville, Alabama, September 1970.

48 Woods, W. C., Arrington, J. P., and H. H. Hamilton II, "A Review of Preflight Estimates of Real-Gas Effects on Space Shuttle Aerodynamic Characteristics," Shuttle Performance: Lessons Learned, NASA Conference Publication 2283, Parts 1, Hampton, VA, Mar 8-10, 1983.

49 Bornemann, W. E., and Surber, T. E., "Aerodynamic Design of the Space Shuttle Orbiter," NASA_techdoc_19790013835, Rockwell International Corporation, Space Division, Downey, CA, 1979.

50 "Shuttle Performance: Lessons Learned," NASA Conference Publication 2283, Parts 1 and 2, Hampton, VA, Mar 8-10, 1983.

51 Wenqing Zhang, Zhijun Zhang, Xiaowei Wang, and Su Tianyi, "A Review of the Mathematical Modeling of Equilibrium and Nonequilibrium Hypersonic Flows," Advances in Aerodynamics, Article 38, 19 December 2022.

52 Gentry, A. E., "*Hypersonic Arbitrary Body Aerodynamic Computer Program*," DAC 61552, Douglas Aircraft Co., Inc, Santa Monica, California, April 1968.

53 Tsien, H. S., "*Superaerodynamics, Mechanics of Rarefied Gases*," Journal of Aeronautical Sciences, pp. 652-664, December 1946.

54 Lees, L., and Probstein, "*Hypersonic Viscous Flow Over a Flat Plate*," Dept. of Aero Engineering, Princeton Univ., Princeton, New Jersey, 1952.

55 Hermann, R., "*Problems of Hypersonic Flight at the Re-Entry of Satellite Vehicles*," Reprint from Sixth International Astronautical Congress, Amsterdam, 1958.

56 Bertram, M. H., and Henderson, A., Jr., "*Effects of Boundary Layer Displacement and Leading Edge Bluntness on Pressure Distribution, Skin Friction and Heat Transfer of Bodies at Hypersonic Speeds*," NACA TN 4301, July 1958.

57 Bertram, M. H., "*Boundary Layer Displacement Effects in Air at Mach Numbers of 6.8 and 9.6*," NASA TR R-22, 1959.

58 Dorrance, W. H., "*Viscous Hypersonic Flow*," McGraw Book Co., New York, 1960.

59 Truitt, T. W., "*Fundamentals of Aerodynamic Heating*," The Ronald Press Co., New York, 1960.

60 Whitfield, J. D., and Griffith, B. J., "*Hypersonic Viscous Drag Effects on Blunt Slender Cones*," AIAA Journal, Vol. 2, No. 10, October 1964.

61 Sieron, T. R., and Martinez, C., Jr., "*Effects and Analysis of Mach Number and Reynolds Number on Laminar Skin Friction at Hypersonic Speeds*," AFFDL-TR-65-5, April 1965.

62 Nagel, A. L., and Thomas, A.C., "*Analysis of the Correlation of Wind Tunnel and Ground Test Data to Flight Test Results*," AIAA/NASA Flight Testing Conference in Huntsville, Alabama, February 15-17, 1965.

63 Bertram, M. H., *Hypersonic Laminar Viscous Interaction Effects on the Aerodynamics of Two-Dimensional Wedge and Triangular Planform Wings*," NASA TN D-3523, August 1966.

64 Liepmann, H. W., and Roshko, A., "*Elements of Gasdynamics*," John Wiley and Sons, Inc., New York, May 1967.

65 John, J. E. A., "*Gas Dynamics*," Allyn and Bacon, Inc., Boston, 1969.

66 *"Aerodynamic Design Data Book, Orbiter Vehicle – Volume 1*," SD 74-SH-0060-1J, Rockwell International/Space Division, Downey, CA, Dec 1975.

67 Elder, D. J., "*Status of Orbiter Hypersonic Studies*," Rockwell International/Space Division, SAS/AERO/76-315, Downey, California, November 1976.

68 Elder, D. J., "*Experimental Investigation of the Hypersonic Viscous Interaction Effects on the Shuttle Orbiter Vehicle Obtained in the CALSPAN Hypersonic*

Facility," Rockwell International/Space Division, SAS/AERO/76-283, Downey, California, May 23, 1975.

69 Burt, R. H., and Jones, J. H., "*Static-Force and Moment Tests of a 0.015-Scale Rockwell International Space Shuttle Orbiter Model at Mach Number 6, 8 and 10*," AEDC-DR-74-20, February 1974.

70 Siler, L. G., and Coats, "*Static Stability and Axial Force Characteristics of the NASA STS 0.01-Scale Model (51-0) of the Vehicle 4 Orbiter at Mach Numbers 16 and 20 (Test 0A81)*," AEDC-DR-74-25, March 1974.

71 Burrows, R. R., and Rogers, C. E. "*Wind Tunnel Test OA113 of the 0.01-Scale Space Shuttle Orbiter Model 51-0 in the CALSPAN Hypersonic shock Tunnel (48-inch Leg)*," DMS-DR-2234, NASA-CR-141,547, July 1975.

72 Jones, R. A., and J. L. Hunt, "*Investigation of Orbiter Real-Gas Effects on Viscous and Inviscid Drag, Pitching Moment and Interaction Effects*," HSAD-NASA-Langley, October 1974.

73 Fivel, H. J., "*Calculated Results and Correlation of Real gas Effects on Orbiter Skin Friction Drag*," McDonnell Douglas Astronautics Company-East, Copy sent to Bill Woods, NASA Langley, July 9, 1975.

74 Fivel, H. J., Masek, R. V., and Mockapetris, L. J., "*Analytical Comparison of Hypersonic Flight and Wind Tunnel Viscous/Inviscid Flow Fields*," NASA CR-2489, 1975.

75 Hunt, J. L., Jones, R. A., and W.C. Woods, "*Investigation of Real-Gas and Viscous Effects on the Aerodynamic Characteristics of a 40 Degree Half-Cone With Suggested Correlations of the Shuttle Orbiter,"* NASA TN D-8418, June 1977.

76 Lomax, H. and M. Inouye, "*Numerical Analysis of Flow Properties About Bodies at Supersonic Speeds in an Equilibrium Gas*," NASA TR R-204, July 1964.

77 Curtis, J. T., and C. R. Strom, "*Computations of the Nonequilibrium Flow of a Viscous, Radiating Fluid About a Blunt Axisymmetric Body, Volume 1: Equations and Results,*" AFFEDL-TR-67-40, June 1967.

78 Cebeci. T., Smith, A. M. O. and L D. Wang, "*A Finite-Difference Method for Calculating Compressible Laminar and Turbulent Boundary Layers*," DAC-67131, Part 1, McDonnell Douglas, March 1969.

79 Cebeci. T., Smith, A. M. O. and G. Mosinskis, "*Calculation of Compressible Adiabatic Turbulent Boundary Layer*," AIAA Paper No. 69-687, June 1969.

80 Blottner, F. G., "*Chemical Nonequilibrium Boundary Layer*," AIAA Paper No. 63-443, August 1963.

81 Hamilton, H., Langley Research Center, provided this researcher with early calculations on a modified 140C Orbiter later published by Marconi, Salas, and Yaeger in the following references [30, 31].

82 Marconi, F., Salas, M., and L. Yaeger, "*Development of a Computer Code for Calculating the Steady Super/Hypersonic Inviscid Flow Around Real Configurations,*" Volume I, Computational Technique. NASA CR-2675, 1976.

83 Marconi, F., Salas, M., and L. Yaeger, "*Development of a Computer Code for Calculating the Steady Super/Hypersonic Inviscid Flow Around Real Configurations,*" Volume II, Code Description, NASA CR-2676, 1976.

84 Moretti, G, and G. Bleich, "*Three-Dimensional Flow Around Blunt Bodies*," AIAA Journal 5, 1966.

85 Moretti, G., Grossman, B., and F. Marconi, *"A Complete Numerical Technique for the Calculation of Three-Dimensional Inviscid Supersonic Flows,"* AIAA Paper No. 72-192, 1972.

86 Moretti, G., *"Thoughts and Afterthoughts about Shock Computations,"* PIBAL Report No. 72-37, 1972.

87 Moretti, G., and M. Pandolfi, *"Entropy Layers" Journal Computers and Fluids,"* January 19, 1973.

88 Moretti, G. and M. Pandolfi, "*Analysis of the Inviscid Flow about a Yawed Cone*," Preliminary studies, PIBAL Report No. 72-18, 1972.

89 Brainerd, J. J., "*Thin Oblique Gasdynamic Shock Waves*," UARI Research Report No. 45, the University of Alabama in Huntsville, Huntsville, Alabama, June 1967.

90 Brainerd, J. J., and W. R. Waldrop, "*The Plasma Sheath in the Nose Region of Selected Reentry Bodies,*" UARI Research Report No. 60, the University of Alabama in Huntsville, Huntsville, Alabama, June 1968.

91 Chen, T. Y., "*Real Gas Flow Fields About Entry Orbiter*," SAS/AERO/74-734, Rockwell International/Space Division, October 1974.

92 Feldman, S., "*On Trails of Axisymmetric Hypersonic Blunt Bodies Flying Through the Atmosphere*," JAS, Vol. 28, pp. 433-448, June 1961.

93 Cheng, H. K., "*The Blunt-Body Problem in Hypersonic Flow at Low Reynolds Number,*" CAL Report No. AF-1285-a-10, Cornell Aeronautical Laboratory, Inc., Buffalo, NY, June 1963.

94 Hanson, C. F., "*Approximation for the Thermodynamic and Transport Properties of High Temperature Air,*" NASA TR R-50, 1959.

95 Elder, D. J., "*An Evaluation of the AEDC Correction Procedure to Test OA-81 Tunnel F Contaminated Data*," IL No. SAS/AERO/74-350, Rockwell/Space Division, Downey, May 1974.

96 Sievon, T. R., and C. Martinez, Jr., "*Effects and Analysis of Mach Number and Reynolds Number on Laminar Skin Friction at Hypersonic Speeds*," AFFDL-TR-65-5m Wright Patterson Air Force Base, Ohio, April 1965.

97 Elder, D. J., "*Response to Aerodynamic Performance Panel Meeting August 1975-Action Item 8/26-20*," Rockwell/Space Division, Downey, October 1975.

98 Elder, D. J., "*Viscous Contribution to the Total Aerodynamic Characteristics of a Typical Shuttle Spacecraft Configuration at Hypersonic Speeds*," T.M. 54/20-279, Lockheed Missiles and Space Co., Inc., Huntsville, Alabama, September 1970.

99 Woods, W. C., Arrington, J. P., and H. H. Hamilton II, "A Review of Preflight Estimates of Real-Gas Effects on Space Shuttle Aerodynamic Characteristics," Shuttle Performance: Lessons Learned, NASA Conference Publication 2283, Parts 1, Hampton, VA, Mar 8-10, 1983.

100 Bornemann, W. E., and Surber, T. E., "Aerodynamic Design of the Space Shuttle Orbiter," NASA_techdoc_19790013835, Rockwell International Corporation, Space Division, Downey, CA, 1979.

101 "Shuttle Performance: Lessons Learned," NASA Conference Publication 2283, Parts 1 and 2, Hampton, VA, Mar 8-10, 1983.

102 Wenqing Zhang, Zhijun Zhang, Xiaowei Wang, and Su Tianyi, "A Review of the Mathematical Modeling of Equilibrium and Nonequilibrium Hypersonic Flows," Advances in Aerodynamics, Article 38, 19 December 2022.

THE FOLLOWING APPENDIX A DESCRIPTION

The Arnold Engineering Development Center's (AEDC) von Karman Facility (VKF) Hotshot Tunnel F flowfield was contaminated by fine dust particles. The dust particles were produced by the vaporization of small amounts of copper, tungsten, and beryllium during electrical discharge in the tunnel's arc chamber. In addition, source flow and flow non-uniformities in the nozzle further contributed to the poor data quality. A joint effort with the test facility resulted in the development of two methods to correct the data; one by this researcher and one by the VKF engineers.

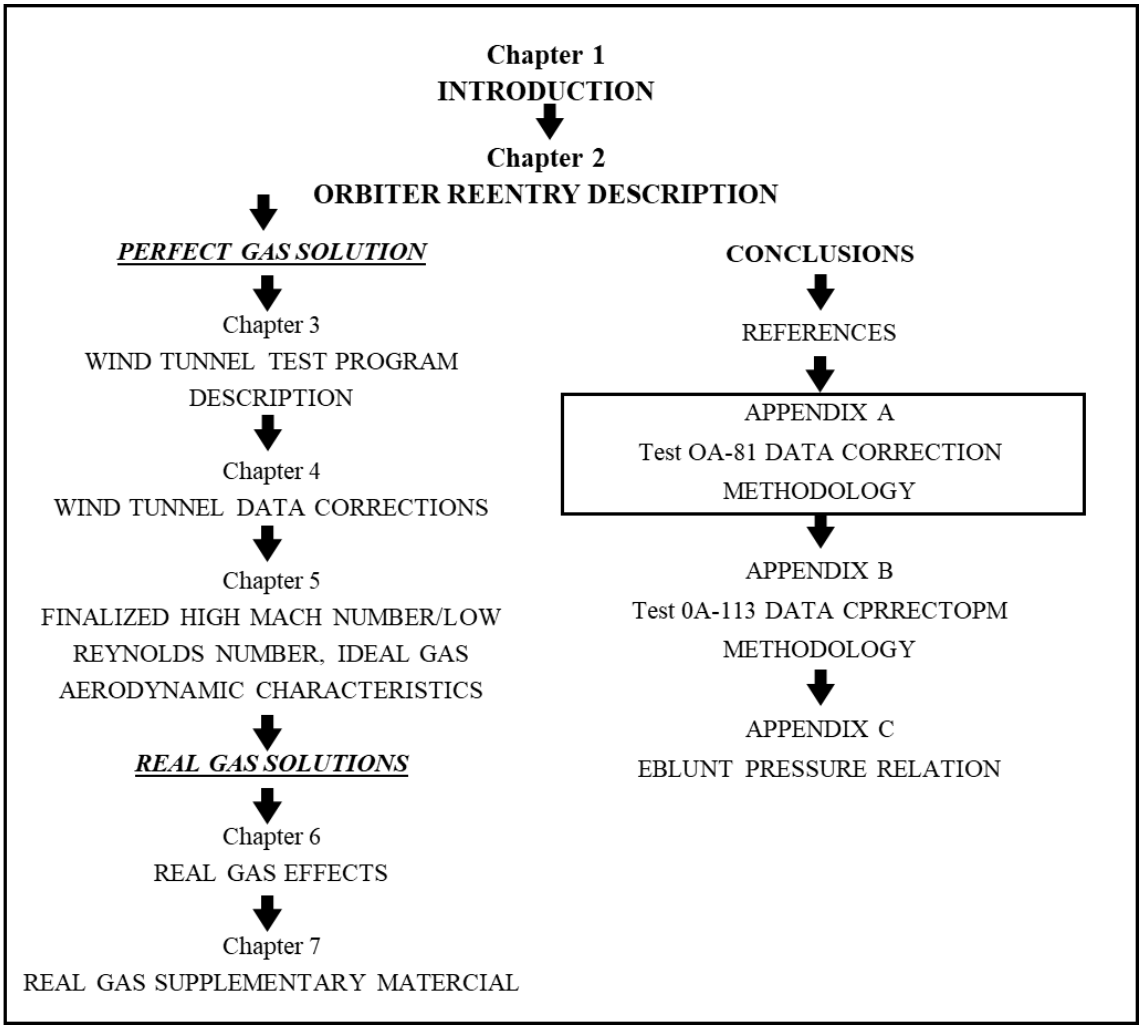
Chapter 1
INTRODUCTION
Chapter 2
ORBITER REENTRY DESCRIPTION
PERFECT GAS SOLUTION
Chapter 3
WIND TUNNEL TEST PROGRAM
DESCRIPTION
Chapter 4
WIND TUNNEL DATA CORRECTIONS
Chapter 5
FINALIZED HIGH MACH NUMBER/LOW
REYNOLDS NUMBER, IDEAL GAS
AERODYNAMIC CHARACTERISTICS
REAL GAS SOLUTIONS
Chapter 6
REAL GAS EFFECTS
Chapter 7
REAL GAS SUPPLEMENTARY MATERCIAL
CONCLUSIONS
REFERENCES
APPENDIX A
Test OA-81 DATA CORRECTION
METHODOLOGY
APPENDIX B
Test 0A-113 DATA CPRRECTOPM
METHODOLOGY
APPENDIX C
EBLUNT PRESSURE RELATION

APPENDIX A

TEST OA-81 DATA CORRECTION METHODOLOGY

An example of AEDC Test OA-81 data scatter is shown in Figure A.1, which was considered unusable without corrections. Because the Hotshot tunnel's contaminated flowfield was considered excessive, a joint and cooperative effort with the VKF engineers was made to develop a method to correct the data. As a result, the cost of conducting the subject tests was saved, preventing additional costly tests. Two approaches were made to correct the contaminated data: (1) this researcher and (2) AEDC VKF wind tunnel staff.

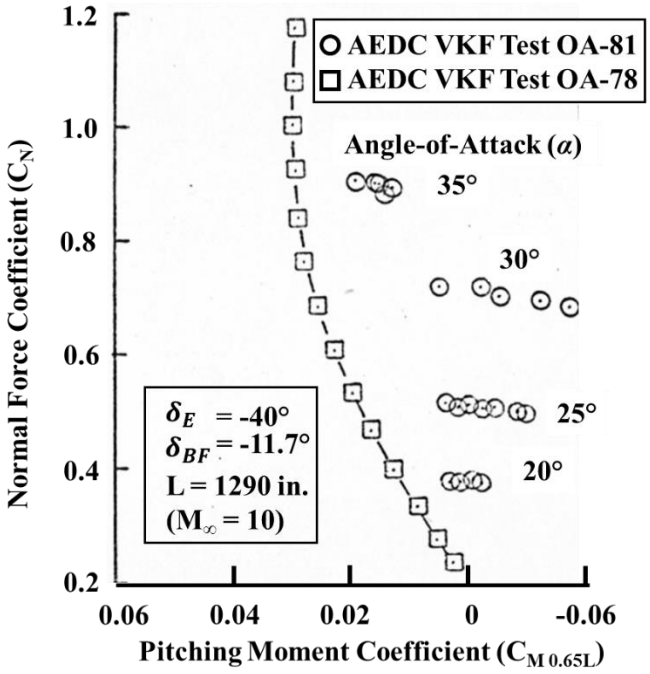

Figure A.1 Example of AEDC OA-81 test data

A.1 SOLUTION 1-RESEARCHER'S APPROACH

The instrumentation used to determine the flow temperature in Tunnel F provided the method for evaluating the contamination effects. In part, the stagnation temperature in Tunnel F is determined from measurements of the heating rates by heat-transfer gauges located in hemisphere/cylinder probes. One gauge is situated at the stagnation point of the hemisphere, and two additional gauges are located on opposite sides of the probe shoulder downstream of the hemisphere/cylinder junction. Theoretical calculations by VKF have provided them with "inferring constants" that define the relationship between the shoulder gauges and the stagnation point heat transfer rate for contamination-free flow. Experiments have shown that the ratio of the measured stagnation point heat-transfer rate inferred by the shoulder gauges, $\dot{q}_o/\dot{q}_o(I)$, is related to the contamination in the tunnel flow. It must be emphasized strongly that the ratio of $\dot{q}_o/\dot{q}_o(I)$—hereafter referred to as the contamination factor—is not a direct measure of the amount of contamination in the flow. Instead, it is a comparison of the effect of contamination on heat transfer between the stagnation point, which is directly in the path of the particles and where the gauge is subject to the maximum contamination effects, to the conditions at the shoulder, where the particles are suspended in the boundary layer and flow tangentially past the gauge with minimal effects.

Figure A.2 shows the viscous parameter, $\bar{V}_\infty'$, and axial force coefficient (C_A) plotted against the contamination factor. It can be seen that a $\bar{V}_\infty'$ range from 0.03 to 0.05 has a correspondingly more extensive range of contamination factors (1.2 to 1.6) than that of $\bar{V}_\infty'$>0.05 (1.15 to 1.38). It can also be seen that C_A scatter is approximately constant over the range of contamination factors. However, theory indicates that C_A increases with

increasing $\bar{V}'_{\infty}$. These observations imply that a more significant amount of contamination occurred at the higher Reynolds number. It must be emphasized again that this is not a measure of the contamination's magnitude, nor can the contribution to C_A due to contamination be obtained. It cannot even be stated with any justification that the contamination factors between 1.1 and 1.3 [lowest $\dot{q}_o/\dot{q}_o(I)$ measured] will not significantly affect the aerodynamics. Whereas it is known that: (1) contamination to some degree is present in the data; (2) differences in C_A between Mach 16 and Mach 20 were measured; and (3) C_A versus $\bar{V}'_{\infty}$ does not conform to theory. Hence, it follows that the data with contamination is suspect and cannot be used with confidence. To salvage the test data, the correlation of C_A and $\dot{q}_o/\dot{q}_o(I)$ was then made using these facts.

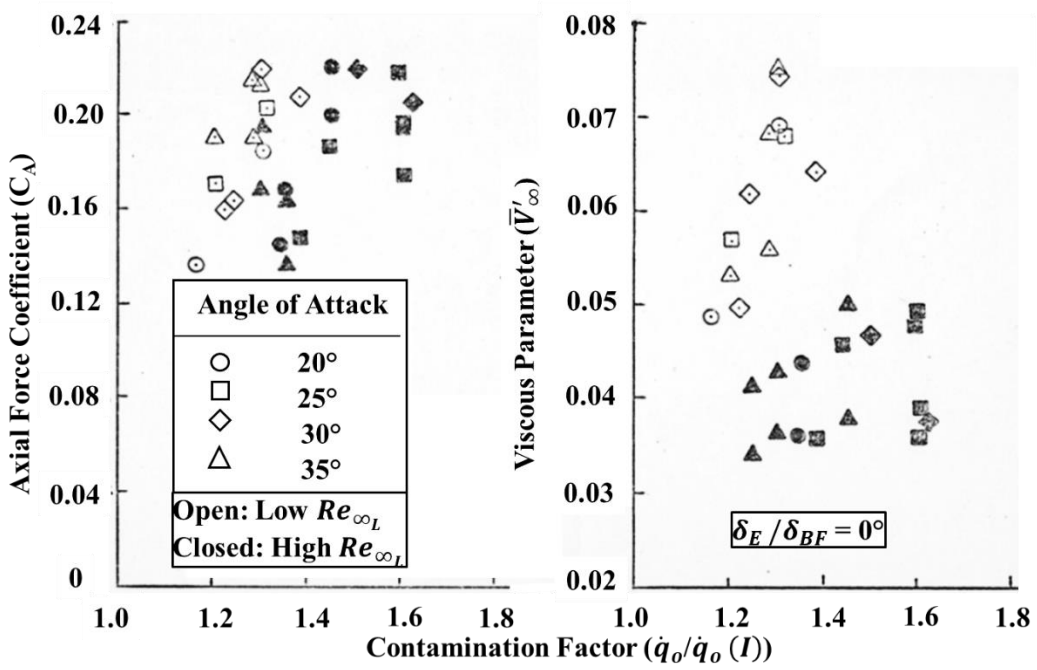

Figure A.2 Example of AEDC OA-81 data scatter as a function of contamination factor

The following relationship defines an unknown axial force:

(A.1)

$$C_{A_v} = C_{A_{iv}}(1 + f),$$

where $C_{A_{iv}}$ is approximately an inviscid axial force coefficient, and C_{A_v} is the axial force coefficient in viscous flow [17, 44]. The variable f is some function of the viscous parameter, $\bar{V}'_\infty$. For this analysis, $C_{A_{iv}}$ is the Mach 10 data from AEDC Test OA-7, 8, and C_{A_v} is the axial force that would have been obtained in Test 0A-81 without contamination.

The procedure used in this analysis was to determine the "average" amount of contaminated and uncontaminated axial force by:

$$\frac{C_{A_{v_m}}}{C_{A_v}} = 1 + F, \tag{A.2}$$

where $C_{A_{v_m}}$ is the measured Test OA-81 data, and F is a function of the contamination factor ($\dot{q}_o/\dot{q}_o(I)$). Note that when the contaminated $C_{A_{v_m}}$ equals the uncontaminated C_{A_v}, F = 0. From Equations (A.1) and (A.2)

$$\frac{C_{A_{v_m}}}{C_{A_{in}}} = (1 + F)(1 + f), \tag{A.3}$$

or simply

$$\frac{C_{A_{v_m}}}{C_{A_{in}}(1 + f)} - 1.0 = \frac{C_{A_{v_m}}}{C_{A_v}} - 1.0, \tag{A.4}$$

where the C_A values are at the same angle of attack and have the same body geometry. Equation (A.4) as a function of the contamination factor is presented in Figure A.3, where C_{A_v} is Mach 10 data obtained from Test OA-78, and $C_{A_{v_m}}$ is the contaminated Mach 20 data.

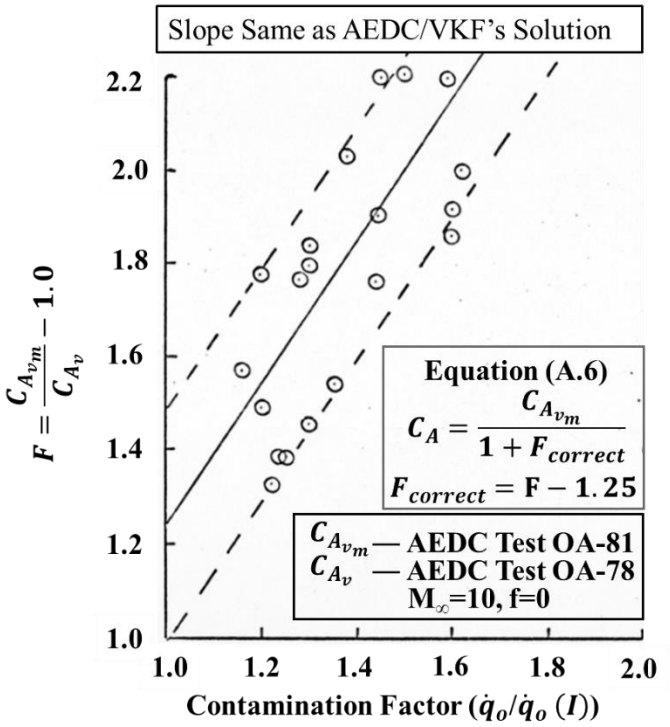

Figure A.3 Correlation of the measured axial force as a function of contamination factor

The data displays a clear dependence on the contamination factor. The correlation of the data with the contamination factor suggests using the linear fairing as an "approximate" correction of the measured axial force. The slope of F with the contamination factor is identically equal to the results obtained by the VKF staff [17, 19, 44], except that F is displaced by a constant at $(\dot{q}_o/\dot{q}_o(I))$ = 1.0. This is simply because f in Equation (A.4) is an unknown and assumed equal to zero. If f were known, the slope of F with the contamination factor would pass through F=0 at $(\dot{q}_o/\dot{q}_o(I))$ = 1.0, as in the case of VKF's solution, which obtains an excellent estimate of axial force with viscous interaction effects. Hence, for this analysis,

$$F_{corrected} = F\text{-}1.25, \tag{A.5}$$

And the corrected axial force coefficient is,

$$C_A = \frac{C_{A_{v_m}}}{1 + F_{corrected}}. \tag{A.6}$$

It must be noted that the purpose of the estimated axial force coefficient was to normalize the measured values and hence, eliminate the angle of attack as a dependent parameter. This allows all the test OA-81 data to be used in one curve, Figure A.3, which increases the accuracy of the linear fairing. The procedure developed here introduces errors in the neighborhood of $\pm$ 15 percent [17, 19, and 44]. Although this is admittedly an undesirable uncertainty, the corrected axial forces are substantially improved over the uncorrected values shown to have more than 100 percent data uncertainty, as shown in Figure A.3.

The axial force component in the presence of dust particles in the flow also produced an error in the pitching moment and calculated center-of-pressure. The contamination contributed false negative (nose down) pitching moment to the model due to contaminated C_A acting on the lower model surface. All locations on the lower model surface are not vertically equidistant from the moment reference center. However, a distance of one inch was used as a representative moment arm length upon which the contaminated C_A acted. All the pitching moment coefficient and center-of-pressure data obtained at M_∞ = 20 have been adjusted to account for this erroneous contamination contribution. It must be noted that this correction procedure has less validity for the positive control surface deflections. This is because dust particles' effects in the boundary layer's separation region are unknown. The problem with using the contamination correction technique is that the data may be overcorrected. Hence, a certain amount of viscous interaction effects may be subtracted. This occurs for the contaminated data below

the linear fairing shown in Figure A.3. However, the contaminated data above the fairing will be under-corrected; hence, contamination remains in the corrected data. Thus the final results must be obtained by fairing through the corrected Test OA-81 data and treating all of the data "equally." Hence, judicious fairing of the data must be made as a function of viscous parameters and angle of attack. This procedure was described in Chapter 3.

A.2 SOLUTION 2-AEDC/VKF'S APPROACH

Unlike the author's approach, AEDC/VKF used a procedure based on heat transfer data and theory to obtain the normalizing C_{A_v} value, Equation A.1. Because of the combination of test data and theory; the VKF staff were forced to make several assumptions.

The first assumption the VKF staff introduced into the analysis is that at high angles of attack, all of the viscous forces and contamination particles acted on the lower surface of the model. This assumption is quite proper as the pressure drops around the fuselage and the upper surface is significant, resulting in a large shallow region with low pressure.

The central assumption that the complete VKF analysis depends on is that heat transfer and skin friction data may be correlated in hypersonic flow using a form of Reynolds Analogy. Reference 45 permitted an exact comparison of skin friction and heat transfer data for the first time for identical test conditions using the same experimental model. The results showed a definite correlation between heat transfer and skin friction on hypersonic flow. The two Reynolds Analogy methods presented in Reference 45 compared well with the test data. Due to the combined errors in the skin friction and heat transfer data, choosing methods is probably fortuitous. However, Reynolds Analogy may be

employed in preliminary design analysis to estimate the friction drag using known heat transfer data or vice versa at hypersonic speeds. This verification is considered proper regarding the VKF's assumption that heat transfer and skin friction data may be correlated in hypersonic flow using a form of Reynolds Analogy.

The VKF staff related the local skin friction to the local Stanton number, C_{h_∞}, by Reynolds Analogy with $C_{f_\infty} = 2C_{h_\infty} Pr^{2/3}$, where Pr is Prandtl number. They assumed that a Stanton number could represent the overall lower model surface. The magnitude of error using this assumption is more likely insignificant when compared with the choice and belief that $C_{f_\infty} = 2C_{h_\infty} Pr^{2/3}$. The overall magnitude of error due to these assumptions is unknown. However, the premises are justified from a theoretical viewpoint and verified experimentally.

With the Reynolds analogy employed in the analysis, the total viscous axial force can then be written as:

$$C_{A_v} = C_{h_\infty})_{average} \frac{S_{wet}}{S_{ref}} = 2C_{h_\infty})_{average} Pr^{2/3} \frac{S_{wet}}{S_{ref}}, \tag{A.7}$$

and introducing the viscous parameter, $\bar{V}'_{\infty,}$ results in the expression:

$$C_{A_v} = C_{h_\infty})_{average} \left(Re_{\infty_L}\right)^{1/2} \frac{2\bar{V}'_\infty \, S_{wet} Pr^{2/3}}{M_\infty (C'_\infty) S_{ref}}. \tag{A.8}$$

Examination of previous experimental force data obtained during the test of the Orbiter model in the AEDC/VKF facility, at Mach numbers from 6 to 16, led the VKF staff to estimate the pressure drag by a value of 0.52. Although this value is not exact and disagrees with the theory by 0.004, the magnitude of error using this value regarding the

(A.9)

overall performance of the Orbiter and C_M is insignificant. Therefore, the VKF staff adequately estimated the pressure drag and, thus, the total estimated axial force as:

$$C_{A_v} = 0.052 + C_{h_\infty})_{average}\left(Re_{\infty_L}\right)^{1/2} \frac{2\bar{V}'_\infty \, S_{wet} Pr^{2/3}}{M_\infty (C'_\infty) S_{ref}}.$$

Although the results from AEDC Test OA-81 did not include either skin friction or heat transfer measurements, they did have test data obtained during the heat transfer test of the Orbiter configuration from Test OH-11 for contamination-free flow. With this data, the VKF staff were able to define the variation of $C_{h_\infty})_{average}\left(Re_{\infty_L}\right)^{1/2}$ as a function of $M_\infty sin\alpha$. However, it must be noted that the values of $C_{h_\infty})_{average}\left(Re_{\infty_L}\right)^{1/2}$ were obtained at low $\bar{V}'_\infty$ conditions, and hence, did not simulate the $\bar{V}'_\infty$conditions experienced during Test OA-81. First, the heat transfer data used by the VKF staff were not extrapolated to the viscous interaction regime of interest (i.e., Test OA-81). On the contrary, they used the actual Test OH-11 measured heat transfer date results. Hence, they assumed that:

$$C_{h_\infty})_{average}\left(Re_{\infty_L}\right)^{1/2} = f(M_\infty, \alpha). \tag{A.10}$$

It may be shown that this assumption is technically justified by relating an empirical relation from CALSPAN Test OA-113 data to Equation A.9. An empirical relation for calculating axial force coefficients in the viscous interaction regime was developed based on CALSPAN Test OA-113 data. The empirical relationship between known and unknown axial force coefficients [17] is as follows:

$$C_A = C_{A_{inviscid}}(1 + F\,\bar{V}'_\infty), \tag{A.11}$$

Where F=F(α). Using the VKF staff's estimated value of the inviscid axial force and substituting it into Equation (A.9) gives:

$$0.052F = C_{h_\infty})_{average}\left(Re_{\infty_L}\right)^{1/2} \frac{2\bar{V}'_\infty \, S_{wet} Pr^{2/3}}{M_\infty (C'_\infty) S_{ref}}. \tag{A.12}$$

Writing this expression in terms of $C_{h_\infty})_{average}\left(Re_{\infty_L}\right)^{1/2}$ gives:

$$C_{h_\infty})_{average}\left(Re_{\infty_L}\right)^{1/2} = \frac{0.52 S_{ref} (C'_\infty)^{1/2}}{2 S_{wet} Pr^{2/3}} \, (M_\infty F). \tag{A.13}$$

For the experimental hypersonic regime of interest, $(C'_\infty)^{1/2}/Pr^{2/3}$ is approximately constant [46]. Hence,

$$C_{h_\infty})_{average}\left(Re_{\infty_L}\right)^{1/2} = G M_\infty F, \tag{A.14}$$

where

$$G = \frac{0.52 S_{ref} (C'_\infty)^{1/2}}{2 S_{wet} Pr^{2/3}}.$$

Therefore,

$$C_{h_\infty})_{average}\left(Re_{\infty_L}\right)^{1/2} = F(M_\infty, \alpha),$$

And hence, it substantiates the VKF staff's assumption, Equation (A.10). Thus, heat transfer data obtained from Test OH-11in the neighborhood of $\bar{V}'_\infty$=0.013 may be used to get theoretical estimates of C_A in the high viscous interaction regime.

A.3 CORRECTED ORBITER TEST OA-81 DATA

Figure A.4 presents AEDC Test OA-81 data before and after applying the contamination correction schemes. It can be seen that the contaminated data is corrected

sufficiently well to correlate with CALSPAN Test OA-113 data. For further examples of the corrected data, return to Figures 3.6 through 3.11.

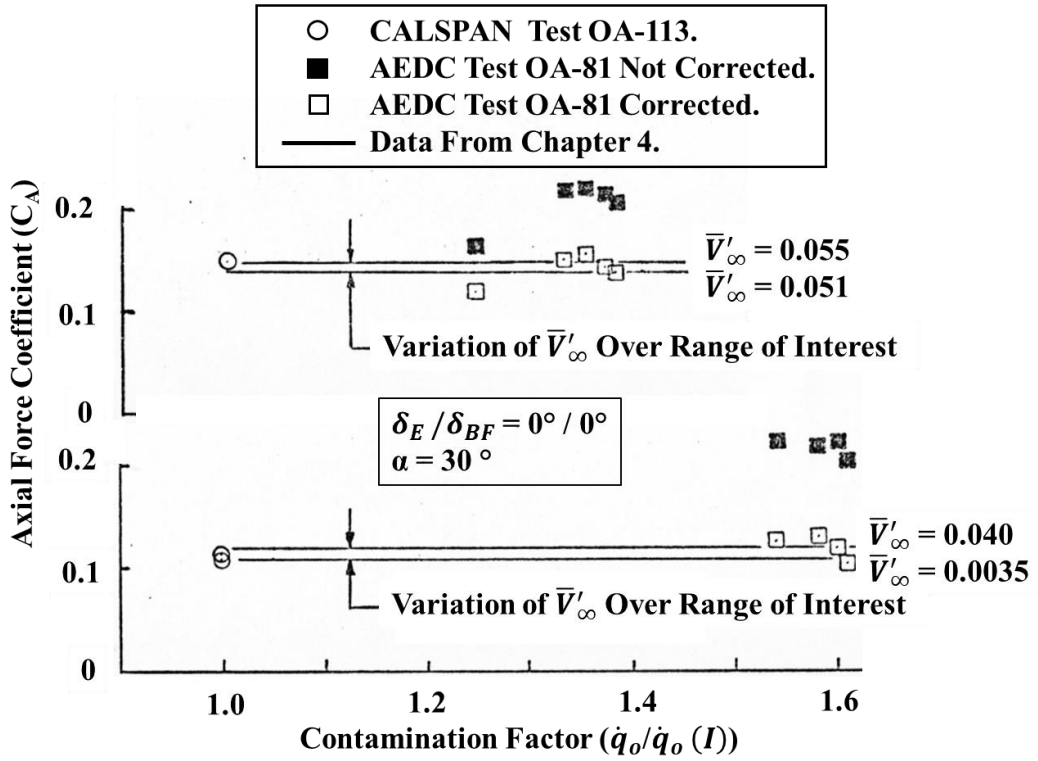

Figure A.4 Example of contaminated axial force coefficients corrected

Since the VKF Tunnel F nozzle is conical, source flow effects were present. Assuming the pressure coefficient at any station of the flat-bottom Orbiter vehicle can be described by the Newtonian expression as a function of the angle of attack and source flow angle, the center-of-pressure location (X_{CP}/L) with source flow present is approximately 0.2 percent forward, and the normal force coefficient is 1.0 percent lower than the uniform flow values. Therefore, these values were applied to the force data (C_N, X_{CP}/L) to account for source flow effects.

Additional corrections to C_N and X_{CP}/L were applied to compensate for flow non-uniformities. The effect of flow non-uniformities on the model's static stability

characteristics was determined by comparing the aerodynamic data obtained with the model in the normal upright mode and that obtained from several runs with the model and balance inverted 180 degrees and pitched towards the bottom of the tunnel. The aerodynamic coefficient C_N and X_{CP}/L were plotted versus the angle of attack for the upright and inverted model orientations. A curve representing the average of these results was assumed to represent the model's actual aerodynamic characteristics. The corrections to C_N and X_{CP}/L are constant increments, independent of the angle of attack, for both Mach numbers 16 and 20 conditions. The resulting corrections were an increase in C_N of 1.7 and 3 percent and a rearward shift in X_{CP}/L of 0.5 and 0.6 percent for the Mach 16 and 20 data, respectively, for upright runs only. The sign of the corrections was reversed for the inverted runs.

The pitching moments were recomputed to reflect the corrections to the center of pressure, normal force, source flow, and flow non-uniformities. Since these effects are negligible, no source flow or flow non-uniformity corrections were applied to the axial force data for the Mach 16 and 20 conditions.

THE FOLLOWING APPENDIX B DESCRIPTION

The CALSPAN (Test OA-113) pitot probe—used to measure dynamic pressure in the 48-inch shock tunnel to compute aerodynamic force and moment coefficients—was mounted too far from the model and close to the tunnel boundary layer to provide reliable values of dynamic pressure. It was also believed that improper alignment of parts in the nozzle and irregularities downstream of the throat contributed to larger-than-normal errors. A solo effort by this researcher developed a method to correct the data.

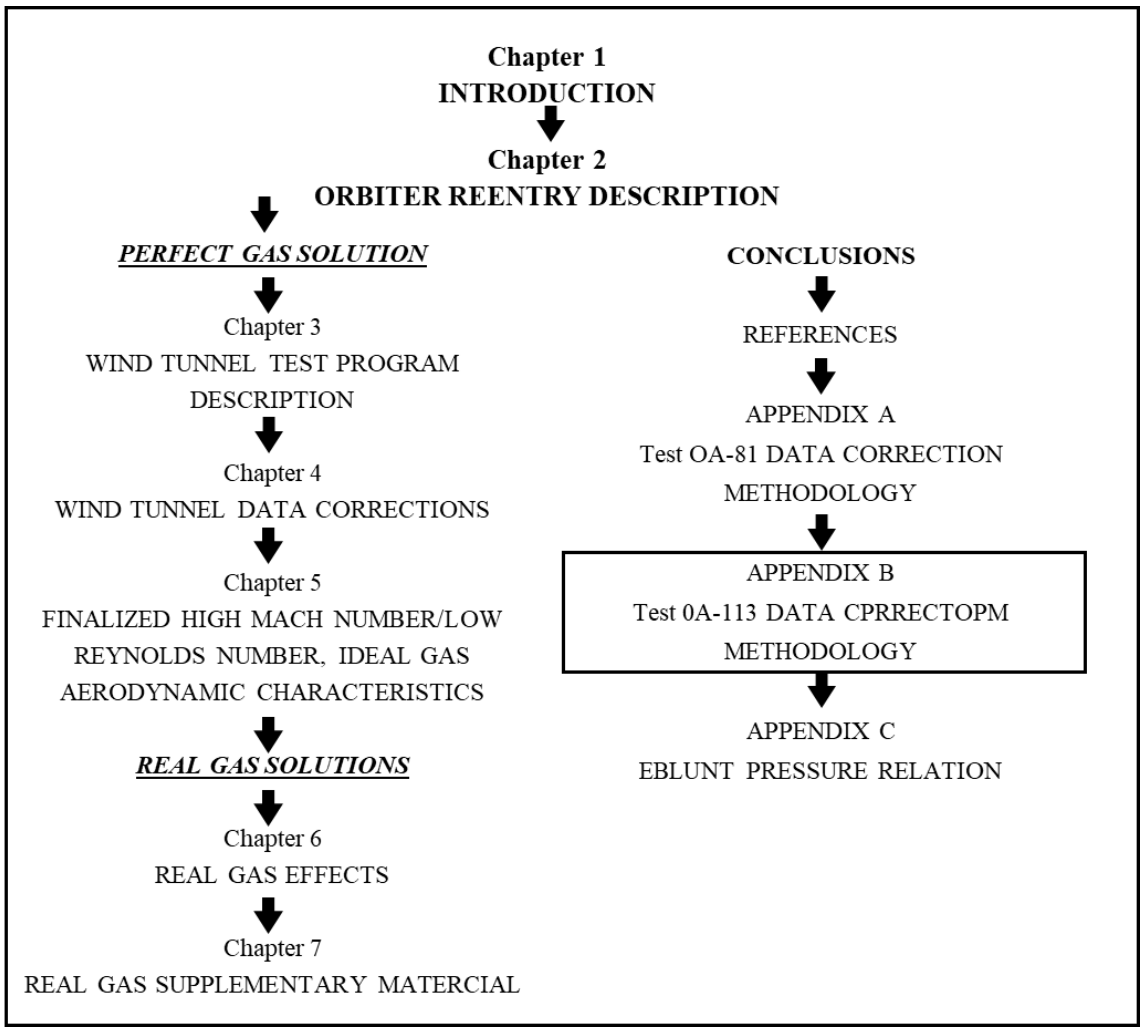
Chapter 1
INTRODUCTION
Chapter 2
ORBITER REENTRY DESCRIPTION
PERFECT GAS SOLUTION
Chapter 3
WIND TUNNEL TEST PROGRAM
DESCRIPTION
Chapter 4
WIND TUNNEL DATA CORRECTIONS
Chapter 5
FINALIZED HIGH MACH NUMBER/LOW
REYNOLDS NUMBER, IDEAL GAS
AERODYNAMIC CHARACTERISTICS
REAL GAS SOLUTIONS
Chapter 6
REAL GAS EFFECTS
Chapter 7
REAL GAS SUPPLEMENTARY MATERCIAL
CONCLUSIONS
REFERENCES
APPENDIX A
Test OA-81 DATA CORRECTION
METHODOLOGY
APPENDIX B
Test 0A-113 DATA CPRRECTOPM
METHODOLOGY
APPENDIX C
EBLUNT PRESSURE RELATION

APPENDIX B

TEST OA-113 DATA CORRECTION METHODOLOGY

Because the CALSAPN Shock Tunnel's (Test OA-113) dynamic pressures were considered unreliable, the author developed a procedure to correct dynamic pressures for the 121 test points. As a result, the cost of conducting the subject tests was saved, preventing additional costly tests.

The solution employed to correct the dynamic pressure was empirical in nature. It utilized the hypersonic principle that the model static pressure divided by the freestream dynamic pressure is a constant (i.e., to within two percent and hence, inside measuring accuracy) for an ideal gas regardless of the flow conditions and is only a function of angle-of-attack. It should be noted that the maximum effect of two percent decreases rapidly and is less than 0.5 percent for freestream Mach numbers greater than 10. Further, this principle has been verified by many experimental investigations. Figure B.1 provides evidence of the validity of this principle. Recall Figure 3.2, which illustrates the location of the two pressure transducers on the lower center line of the fuselage. The experimentally measured model static pressure (i.e., P_{m_3}, P_{m_4}) variation with dynamic pressure is shown in Figure B.2. It can be seen that regardless of Mach number or Reynolds number,

P_{m_3} and P_{m_4} varies linearly with q_∞ to within measuring accuracy. Hence, P_m/q_∞ is only a function of the angle of attack, as shown in Figure B.3.

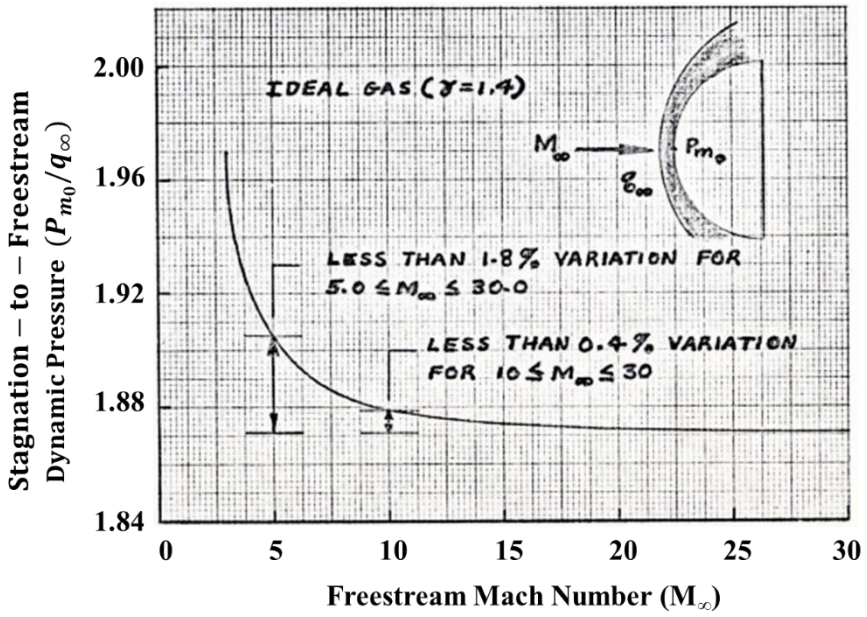

Figure B.1. Theoretical stagnation-to-freestream dynamic pressure as a function of Mach number for an ideal gas

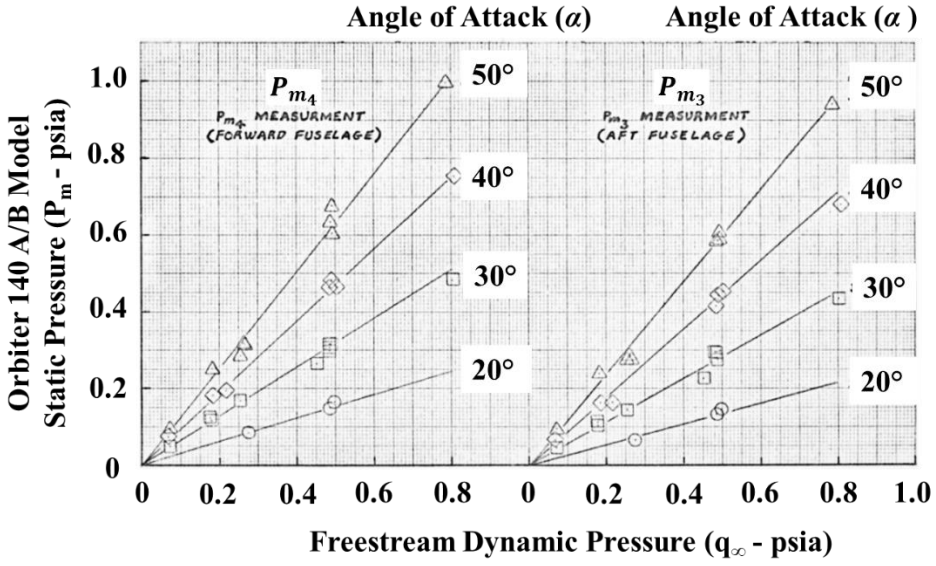

Figure B.2 Orbiter 140 A/B Model 51-0 static pressure variation with dynamic pressure

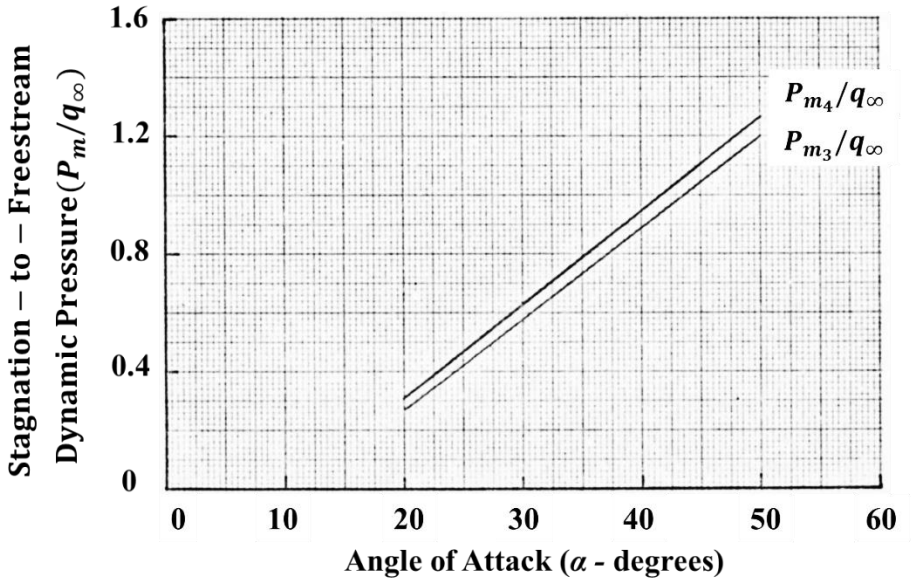

Figure B.3 Orbiter 140 A/B Model 51-0 stagnation-to-freestream dynamic pressure as a function of angle of attack

Figure B.4 shows the measured forward model static pressure, P_{m_4} (again, see Figure 3.2), versus the measured dynamic pressure.

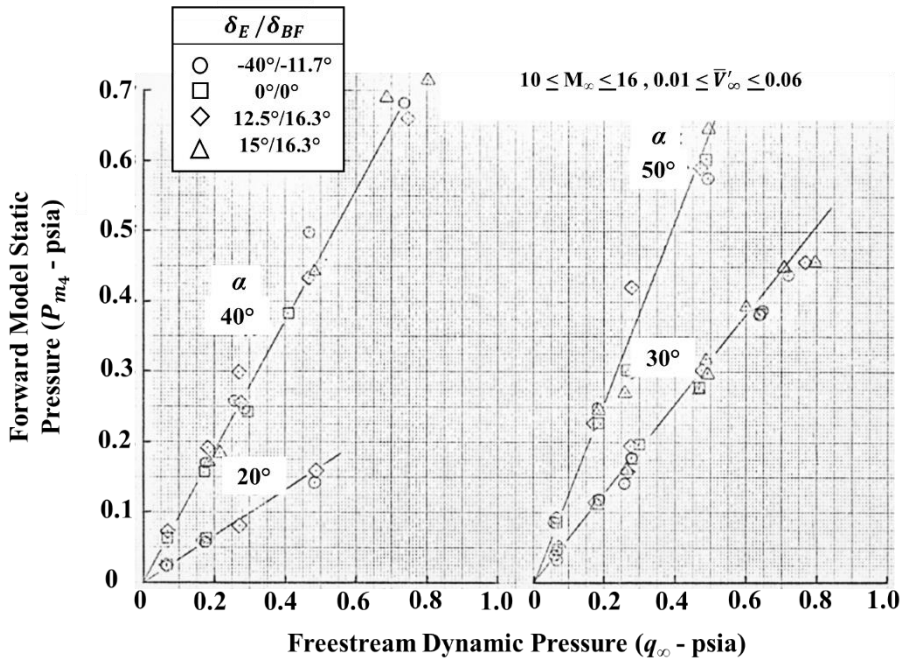

Figure B.4 Model static pressure vs. airflow measured dynamic pressure

It can be seen that although P_{m_4} does correlate with the measured q_∞, the data scatter is such that a poor definition of P_{m_4}/q_∞ is achieved at best. However, since P_{m_4} can have but one value for a given q_∞ (i.e., disregarding flow separation or induced pressure effects), it follows that P_{m_4} must also correlate with normal force, F_N. Both should change proportionally with the angle of attack, see Figure B.5. The linearity of the data correlation indicates that F_N is unaffected by viscous interaction. This was substantiated by theory, Reference 47, and Chapter 5, where it was estimated that viscous interaction effects on F_N are 3 percent or less over the altitude range of interest and, effectively, cannot be measured. This is further substantiated by Figure B.6, where axial force, F_A, does not correlate linearly with P_{m_4}, nor do the two change proportionally with the angle of attack. As expected, the FA magnitude depends on the viscous interaction contribution.

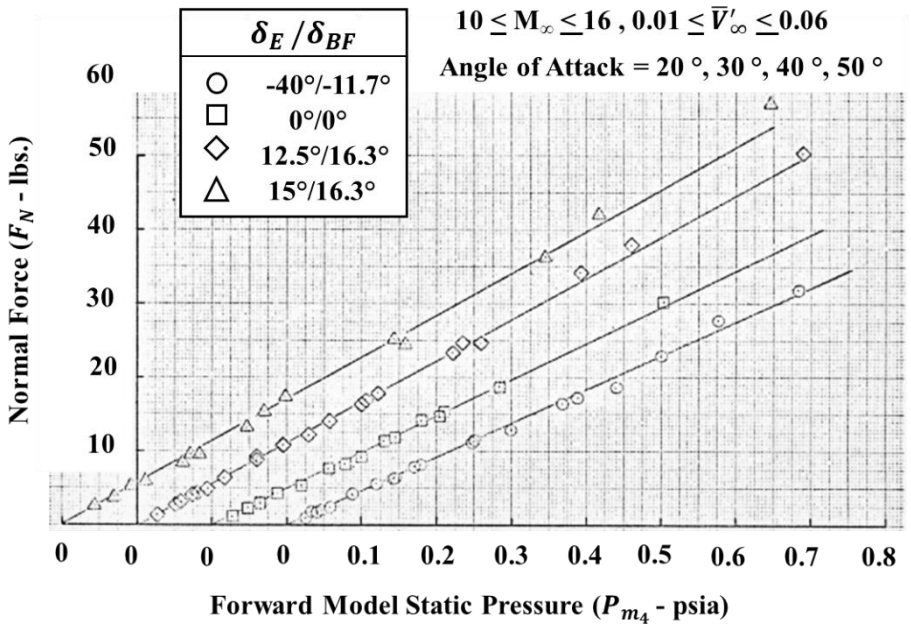

Figure B.5 Normal force versus forward model static pressure

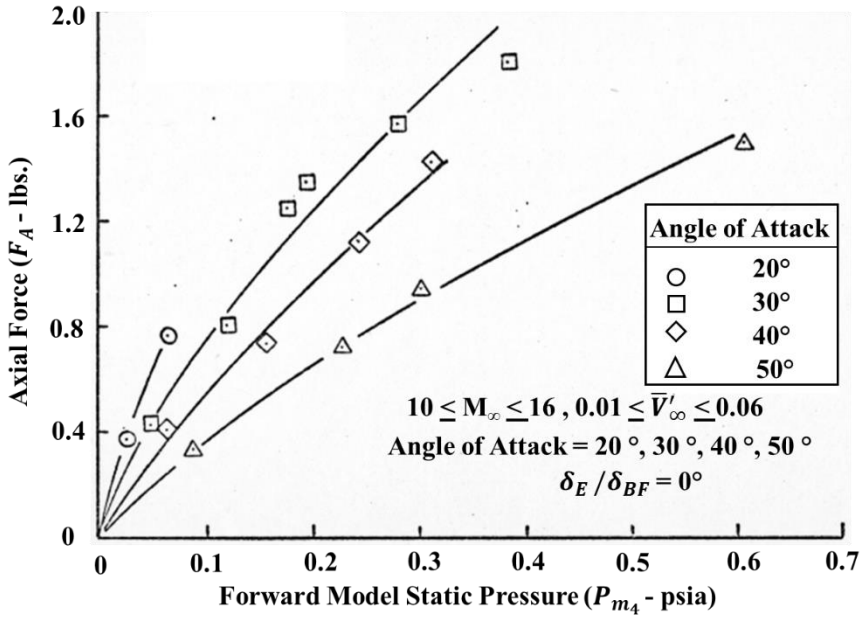

Figure B.6 Axial force versus forward model static pressure

Interestingly, in the four pressure transducers mounted on the model, the only noticeable change in pressure with $\bar{V}'_\infty$ was on the outer wing. Figure B.7 shows that the data correlation is not linear, which substantiates the observation that P_{m_4} and F_N are unaffected by viscous interaction effects (i.e., within measuring accuracy).

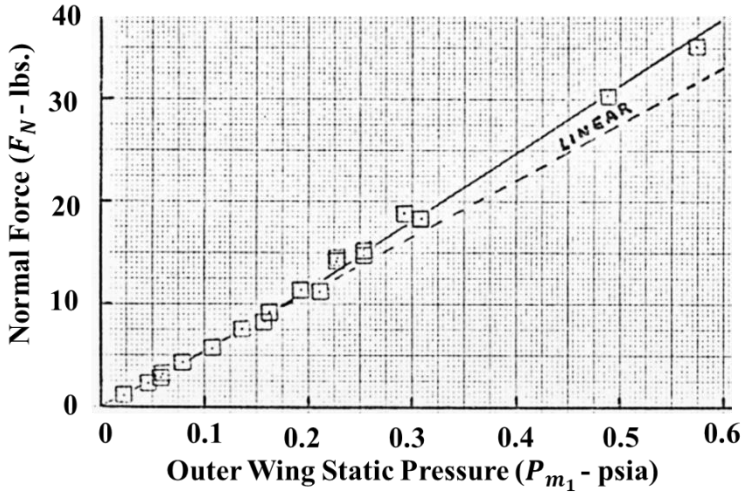

Figure B.7 Normal force versus outer wing static pressure

Following reasoning by deduction: "Since P_{m_4} and q_∞ must correlate and P_{m_4} and F_N must correlate, then F_N and q_∞ must correlate." Figures B.8a through B.8d show their correlation. Since it is assumed that F_N is a constant, within measuring accuracy, the corrected dynamic pressures, $q_{\infty_{Corrected}}$, are obtained by adjusting each q_∞ data point to the faired line in the four figures.

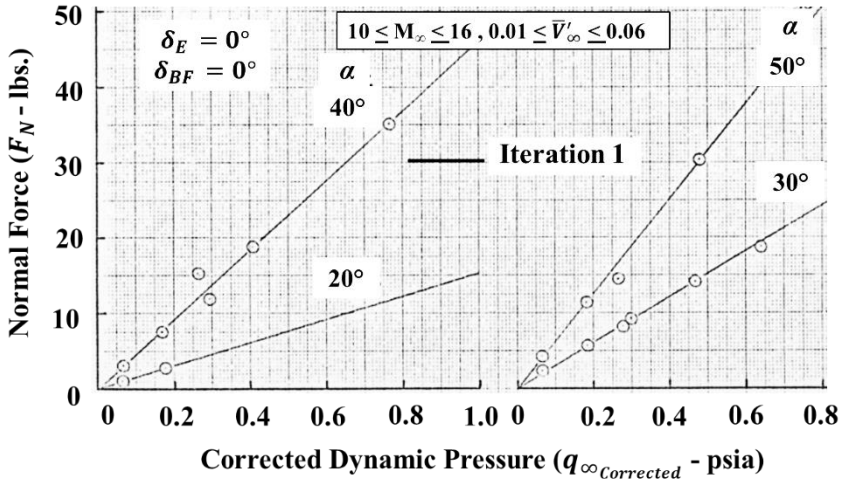

Figure B.8a Normal force versus dynamic pressure, $\delta_E = 0°$ and $\delta_{BF} = 0°$

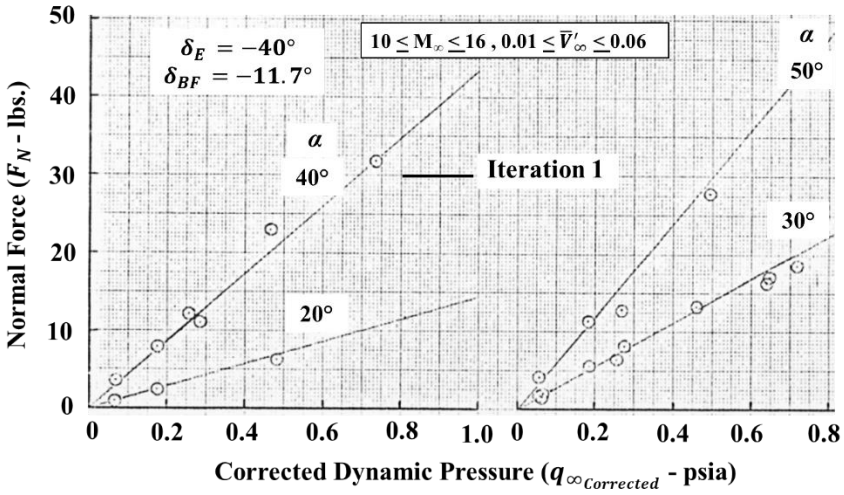

Figure B.8b Normal force versus dynamic pressure, $\delta_E = -40°$ and $\delta_{BF} = -11.7°$

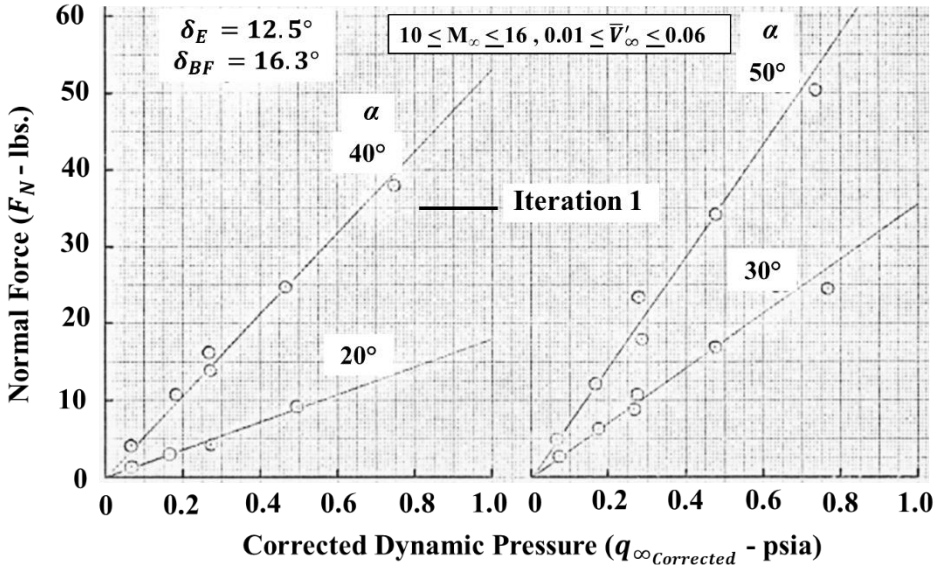

Figure B.8c Normal force versus dynamic pressure, $\delta_E = 12.5°$ and $\delta_{BF} = 16.3°$

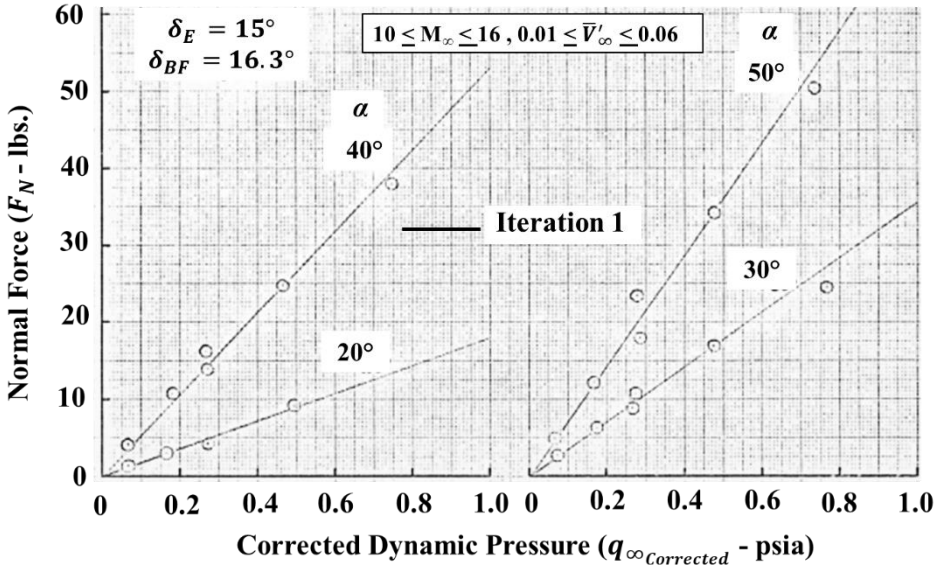

Figure B.8d Normal force versus dynamic pressure, $\delta_E = 15°$ and $\delta_{BF} = 16.3°$

An example of obtaining $q_{\infty_{Corrected}}$ from Figure B.8a is provided in Figure B.9.

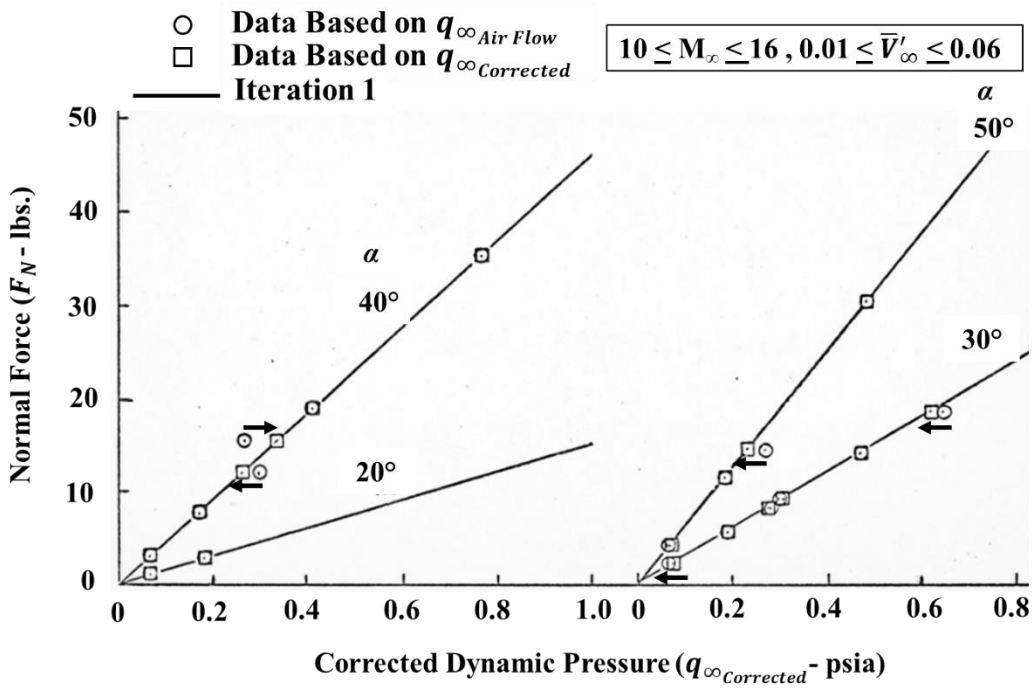

Figure B.9 Example for obtaining $q_{\infty_{Corrected}}$ based on Iteration 1, $\delta_E/\delta_{BF} = 0°$

This first correction is designated Iteration 1.

Suppose the initial fair (Iteration 1) was correctly performed through the data in Figures B.8a through B.8d. In that case, all the data must collapse to one linear line for P_{m_4} versus $q_{\infty_{Corrected}}$ for a given angle of attack regardless of model geometry (e.g., control surface deflections). It can be seen from Figure B.10a that the scatter has collapsed sufficiently well to obtain a reasonably good fair when compared with Figure B.4. This second correction is designated Iteration 2.

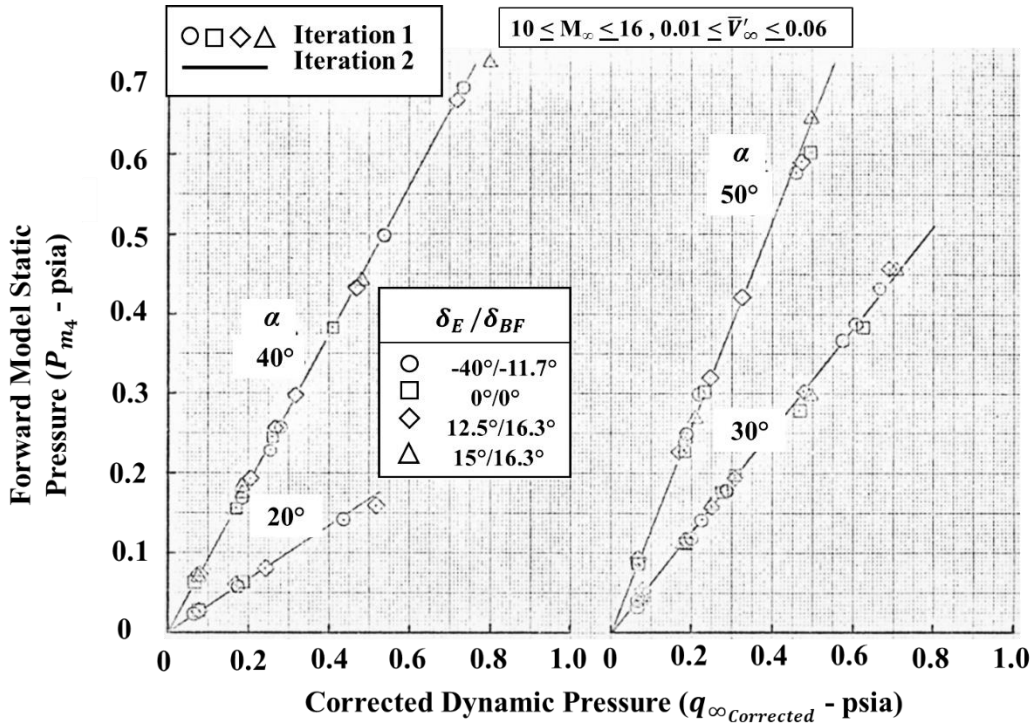

Figure B.10a Model P_{m_4} static pressure vs. corrected dynamic pressure

What makes this approach so attractive over that of attempting to correlate P_{m_4} with q_∞ in Figure B.4 is the fact that four different sets of data correlations (i.e., geometry dependent) at given angles of attack were used to establish the one required fair in Figure B.10a. Hence, it can be thought of that Iteration 2 is a statistical average from Iteration 1. It must be pointed out that the actual measured values of F_N and P_{m_4} have not been changed; only q_∞ has been corrected from its wind tunnel measurements.

Figures B.10b and B.10c demonstrate that $q_{\infty_{Corrected}}$ correlates well with P_{m_3} and P_{m_2}, hence, any point on the body; except for the case of P_{m_1} shown in Figure B.10d. Results of these corrections were presented in Chapter 4, Figures 4.4 through 4.7.

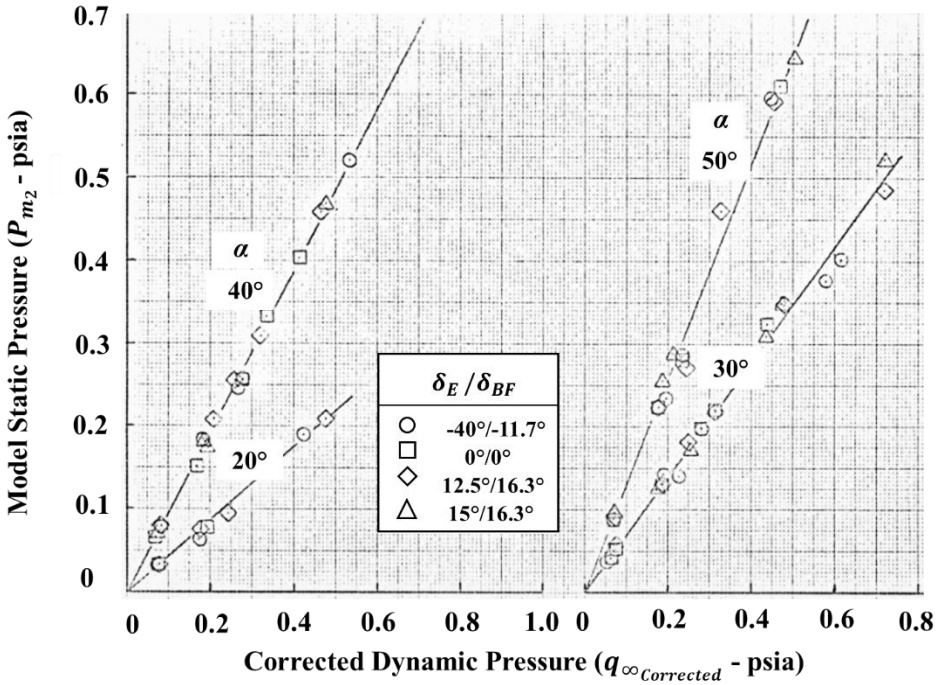

Figure B.10b Model P_{m_2} static pressure vs. corrected dynamic pressure

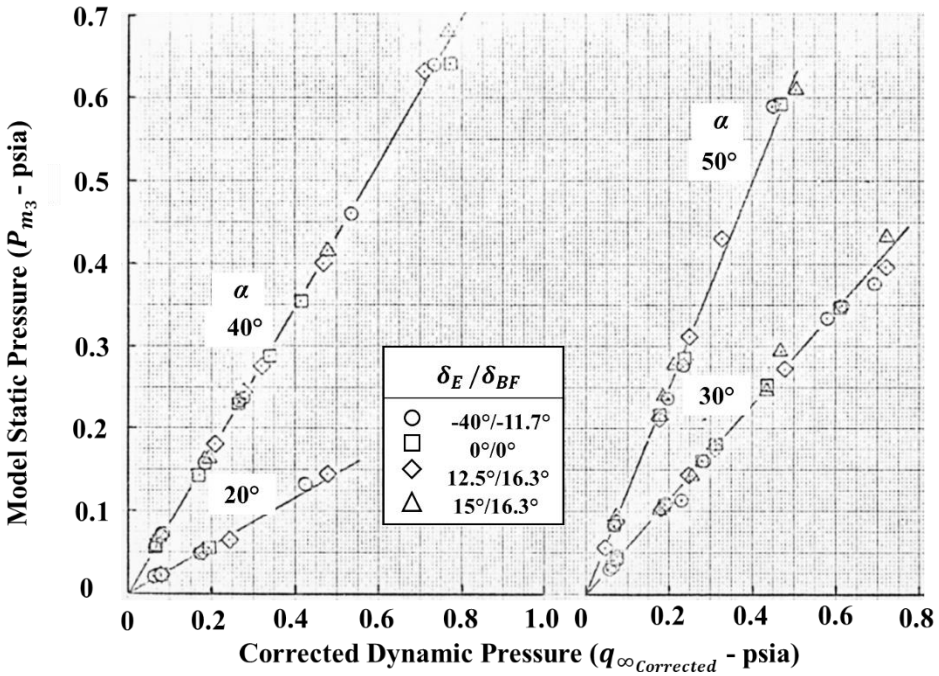

Figure B.10c Model P_{m_3} static pressure vs. corrected dynamic pressure

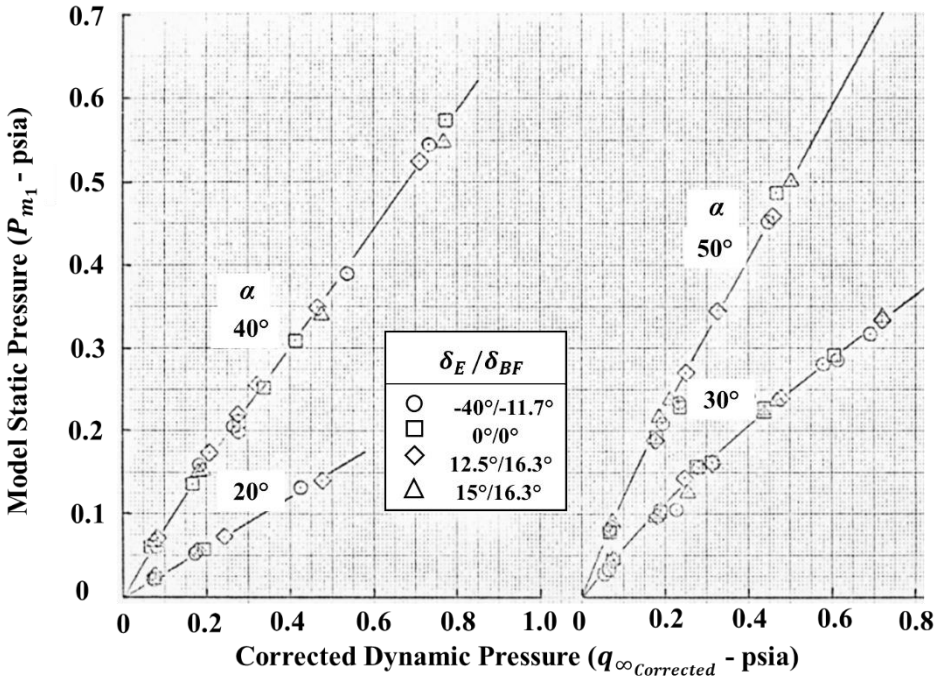

Figure B.10d Model P_{m_1} static pressure vs. corrected dynamic pressure

As is the case for any analysis by deduction, the actual validity of the solution rests on comparison with the known; test data in this case. If the solutions presented herein are valid, they must be substantiated by results from other 140 A/B Orbiter hypersonic test data. Figure B.11 compares the results from Iteration 2 and test data for a Mach number range between 5 and 10. Within engineering accuracy, the solution developed is excellent.

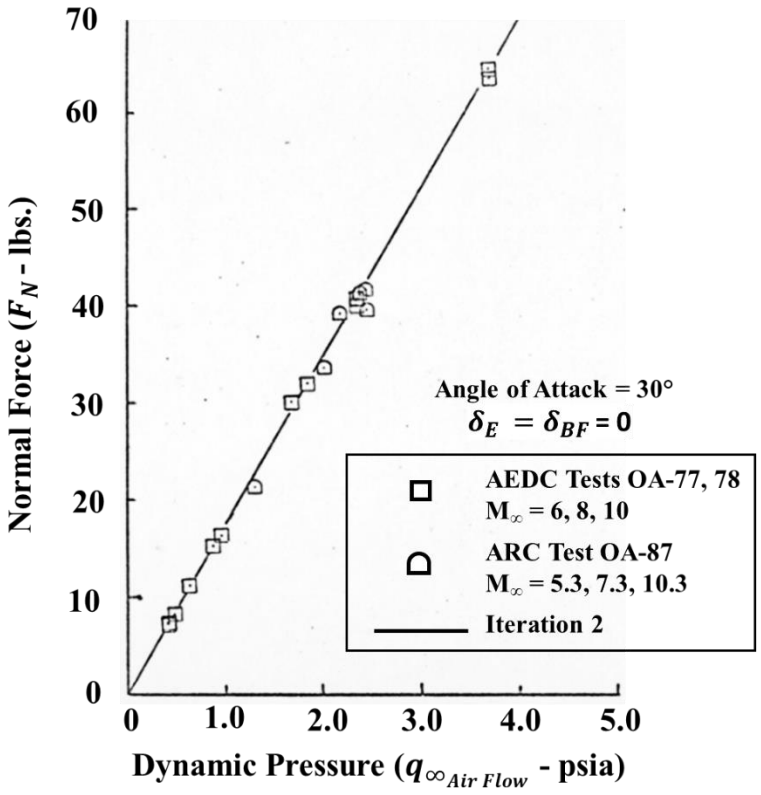

Figure B.11 Substantiation of Iteration 2 by plotting against AEDC and ARC's test data

The dynamic pressure was also analyzed with the measured data because of similar data uncertainties in AEDC Test OA-81 (see Appendix B). As a result, it was determined that the dynamic pressure had a scatter not anticipated by the AEDC test engineers. Figure B.12 compares AEDC Test OA-81 data results against the corrected results obtained from Iteration 2. It can be seen from this example that much of the AEDC Test OA-81 data substantiates $q_{\infty_{Corrected}}$. However, the results indicate a dynamic pressure problem similar to CALSAPN Test OA-113. Therefore, this researcher adjusted the AEDC Test OA-81 data similarly to CALSAPN Test OA-113. The results of the corrections were presented in Chapter 3, Figures 3.8 through 3.11.

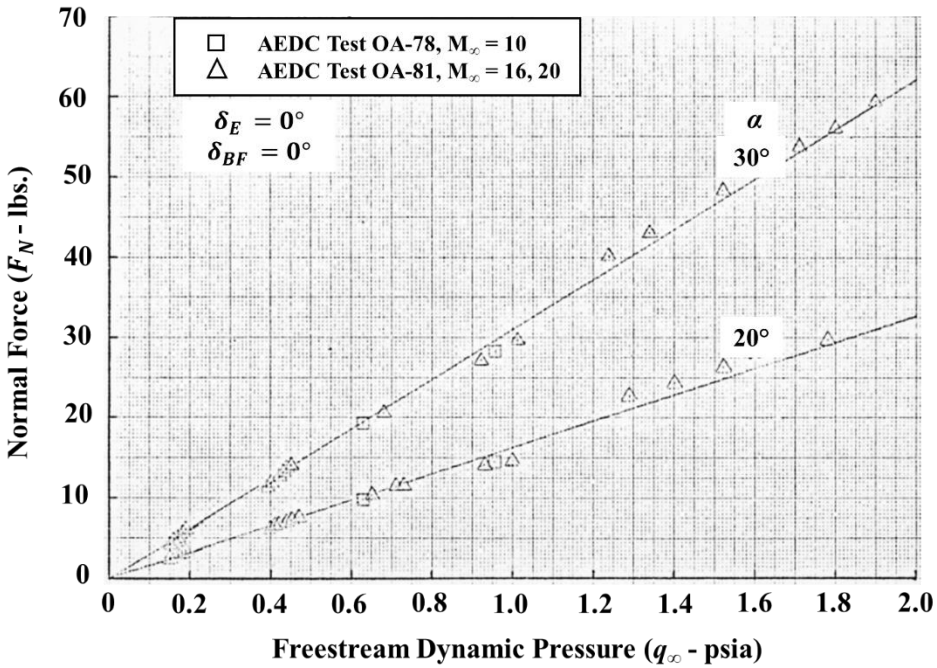

Figure B.12 Example of the amount of adjustment necessary to correct the AEDC Test OA-81 data

The conclusions that can be drawn from these corrections of dynamic pressure are:

1. The probable cause for the data anomalies observed during the CALSAPN Test OA-113 program was resolved. CALSPAN took action to ensure that the spurious misalignment of the nozzle parts will not occur in future tests.

2. The CALSPAN standard data reduction procedure, which relies on past airflow correlations, is reliable.

3. The employment and use of static pressure taps near the nose of the model is a reliable procedure to check dynamic pressures based on standard facility data reduction procedures and should be used as a fail-safe system for all impulse facility testing.

4. The correction technique described in this Appendix has theoretical justification and is substantiated by a recent airflow test performed by CALSPAN.

THE FOLLOWING APPENDIX C DESCRIPTION

A rapid and accurate analytical method is provided for calculating the stagnation and sonic conditions and pressure distribution on blunt bodies in a uniform stream is provided. The real gas aerodynamic estimations in Chapter 6 were derived based on these results.

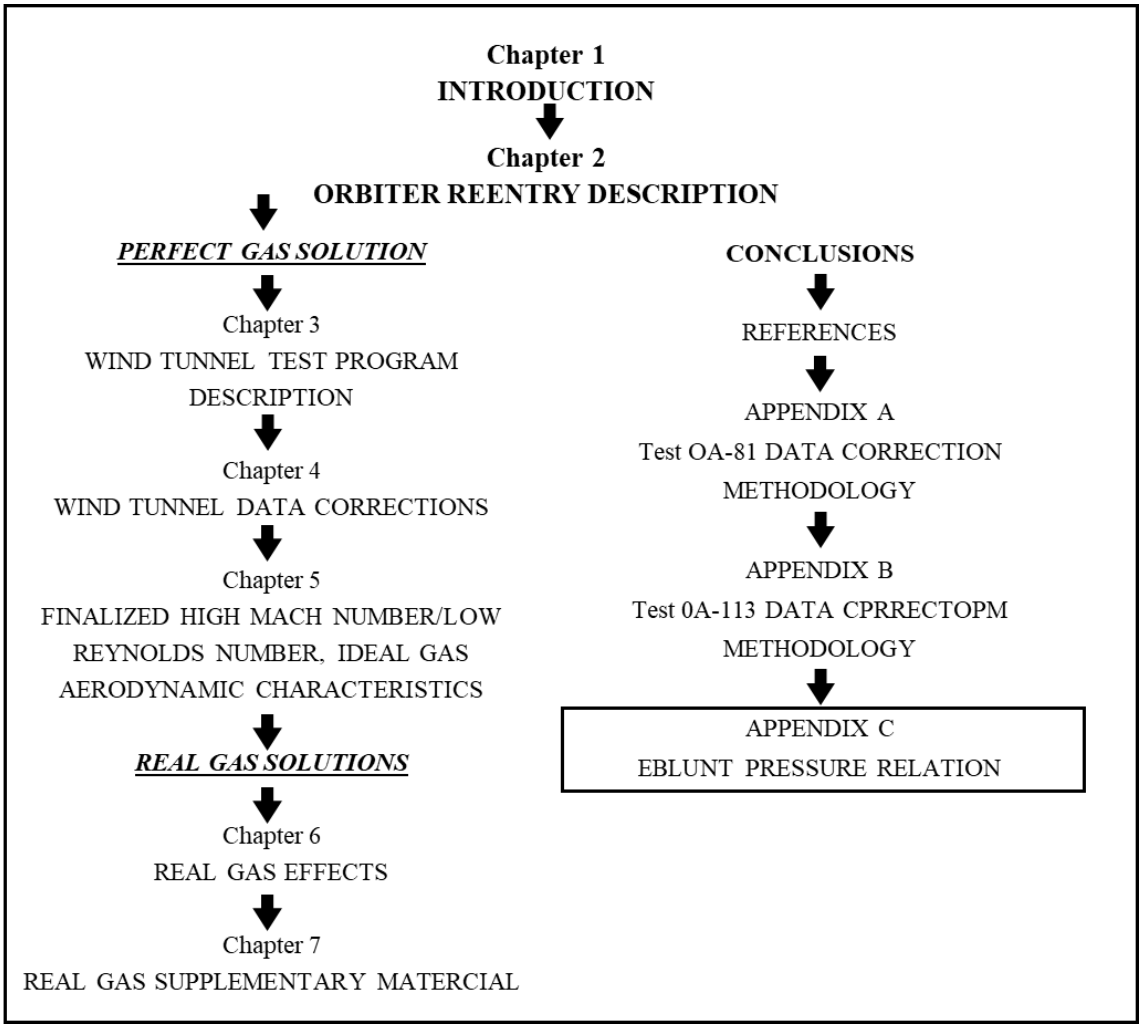

APPENDIX C

EBLUNT PRESSURE RELATION

A rapid and accurate analytical method for calculating the pressure distribution on blunt bodies in a uniform stream and real gas aerodynamic estimations were derived by solving the energy equation behind the shock. The gas was assumed to be perfect, the flow steady and inviscid, and the ratio of specific heat varied with velocity and altitude. The inverse of the density ratio, $\varepsilon = \rho_\infty/\rho$, was not necessarily small compared with unity.

The resultant solution is perhaps the first acceptable analytical treatment of the nosetip solution having the form of the well-known modified Newtonian impact theory, i.e., $\boldsymbol{P_n} = 1 - K\,sin^2\eta$. However, unlike the empirical constant, *K*, in the modified Newtonian expression, a complex expression that is a function of the ratio of specific heats, density, and velocity is derived. This nosetip solution, applicable from the stagnation point to the sonic line, has been named EBLUNT for the sake of no better name.

The results of the analysis approached the Newtonian values for the limit:

$$\begin{matrix} \gamma \to 1.0, \\ M_\infty \to \infty. \end{matrix} \tag{C.1}$$

For this limit, the gas parameter

$$\lambda = \frac{\gamma - 1}{\gamma + 1}, \tag{C.2}$$

and the inverse of the density ratio, ε, across a normal shock and at the sonic line [38, 39]

$$\varepsilon_{ns} = \lambda - \frac{1-\lambda}{M_\infty^2}, \tag{C.3}$$

$$\varepsilon_{sl} = 1.6487\ \epsilon_{ns}\left[1 - \frac{\varepsilon_{ns}}{4}\left(2 + \frac{\lambda}{\varepsilon_{ns}}\right)\right], \tag{C.4}$$

approaches zero, the shock standoff distance approaches zero, the shock approaches the body's shape, and the sonic point on the surface approaches the stagnation point.

C.1 ENERGY EQUATION

The energy equation is given by:

$$H = h + \frac{1}{2}V^2 = h_\infty + \frac{1}{2}V_\infty^2. \tag{C.5}$$

Using the expression for a thermally[4] and calorically[5] perfect gas,

$$h = \frac{\gamma}{\gamma - 1}\frac{p}{\rho},$$

yields

$$\frac{\gamma}{\gamma - 1}\frac{p}{\rho} + \frac{1}{2}V^2 = \frac{\gamma}{\gamma - 1}\frac{p_\infty}{\rho_\infty} + \frac{1}{2}V_\infty^2,$$

or

$$\frac{\gamma}{\gamma - 1}\left[\frac{\rho_\infty}{\rho}\frac{p - p_\infty}{\rho_\infty} + \frac{\rho_\infty}{\rho}\frac{p_\infty}{\rho_\infty} - \frac{p_\infty}{\rho_\infty}\right] + \frac{1}{2}V^2 = \frac{1}{2}V_\infty^2. \tag{C.6}$$

---

[4] $p = \rho RT$.

[5] Specific heat at constant pressure, C_p, is a constant and $C_p - C_v = R$.

Using the gas parameter, Equation C.2, the normalized pressure parameter, $\boldsymbol{P_n} = (p - p_\infty)/\rho_\infty V_\infty^2$, and the inverse of the density ratio, $\varepsilon = \rho_\infty/\rho$, and dividing by V_∞^2, Equation C.6 becomes:

$$\frac{1+\lambda}{\lambda}\left[\varepsilon \boldsymbol{P_n} - (1-\varepsilon)\frac{p_\infty}{\rho_\infty V_\infty^2}\right] + \frac{V^2}{V_\infty^2} = 1. \tag{C.7}$$

Since the speed of sound in a perfect gas is given by:

$$a^2 = \frac{\gamma p}{\rho},$$

the second term in the brackets of Equation C.7 is arranged as follows:

$$\frac{p_\infty}{\rho_\infty V_\infty^2} = \frac{1}{\gamma}\left(\frac{\gamma p_\infty}{\rho_\infty}\right)\frac{1}{V_\infty^2} = \frac{1-\lambda}{1+\lambda}\,\frac{a_\infty^2}{V_\infty^2} = \frac{1-\lambda}{1+\lambda}\left(\frac{1}{M_\infty^2}\right).$$

The energy equation is now,

$$(1+\lambda)\varepsilon \boldsymbol{P_n} - (1-\varepsilon)(1-\lambda)\frac{1}{M_\infty^2} = \lambda(1-Q^2), \tag{C.8}$$

where $Q^2 = V^2/V_\infty^2$. Using Equation C.3 gives the pressure relation

$$\boldsymbol{P_n} = \frac{1}{1+\lambda}\left[\frac{\varepsilon_{ns} - \lambda Q^2}{\varepsilon} + \lambda - \varepsilon_{ns}\right]. \tag{C.9}$$

or simply

$$\boldsymbol{P_n} = \boldsymbol{P_n}(\lambda, \varepsilon, \text{geometry}). \tag{C.10}$$

C.2 BOUNDARY CONDITIONS ALONG THE SURFACE

The flow behind the strong shock and immediately adjacent to the body will accelerate tangentially (i.e., to the surface) from zero at the stagnation point to sonic

velocity. Hence, the density must decrease from a maximum at the stagnation point to a lower level at the sonic line. At sonic velocity, the isentropic density ratio [38, 39] is

$$\left(\frac{\rho}{\rho_o}\right)_{sonic} = \left(1 + \frac{\lambda}{4}\right) \exp\left(-\frac{1}{2}\right) + 0\,\lambda^2. \tag{C.11}$$

For the limit, $\lambda \to 0$ $(i.e., \gamma \to 1)$,

$$\left(\frac{\rho}{\rho_o}\right)_{sonic} \underset{\lambda \to 0}{\to} \exp\left(-\frac{1}{2}\right) = 0.606531 \ldots \tag{C.12}$$

The density ratio along the body will thus vary between:

$$1 \geq \frac{\rho}{\rho_o} \geq \exp\left(-\frac{1}{2}\right), \tag{C.13}$$

As a side note, it is interesting to see that the limit, $\lambda \to 0$, of a particle isentropic flow of a perfect gas, as considered here, gives

$$\left(\frac{p}{p_o}\right)_{sonic} \to \left(\frac{\rho}{\rho_o}\right)_{sonic} \to 0.606531 \ldots ,$$

$$\left(\frac{T}{T_o}\right)_{sonic} = 1 - \lambda \to 1.0.$$

This range of density, Equation (C.13), indicates that any solution employing density as a constant to the first order cannot be valid from the stagnation point to the sonic line. For stagnation,

$$\varepsilon_o = \frac{\rho_\infty}{\rho_o} = \varepsilon_{ns}\left(1 - \frac{\varepsilon_{ns}}{2}\right), \tag{C.14}$$

where ε_{ns} is given by Equation (C.3). Thus, for large Mach number and small γ (i.e., small ε), it is clear that ε will vary approximately

$$\varepsilon_{ns} \exp\left(\frac{1}{2}\right) \geq \varepsilon \geq \varepsilon_{ns}. \tag{C.15}$$

The critical point to note here is that while ε is a variable, it is mainly a function of ε_{ns}. Brainerd's basic approach was to develop all flow variables in the subsonic region in ascending power series in ε_{ns}. For this approach to be valid, ε_{ns} must be small. Hence, the inverse of the density ratio was expressed by [39].

$$\varepsilon = \varepsilon_{ns}(e_1 + \varepsilon_{ns}e_2 + \varepsilon_{ns}^2 e_3 + \cdots), \tag{C.16}$$

And similar to Equation (C.10)

$$\boldsymbol{P_n} = \boldsymbol{P_n}(\lambda, \varepsilon, \text{geometry}).$$

$\boldsymbol{P_n}$ is a function of λ, Equation (C.2) and ε, Equation (C.3), and both are functions of γ. Thus, normal force and pitching moment are also a function of γ. And for a perfect gas, $\gamma = 1.4$, and real gas, $\gamma < 1.4$.

C.3 SIMPLIFICATION OF THE PRESSURE RELATION

Since ε and Q are the only unknowns in Equation (C.9), the following procedure will permit eliminating one of these variables. Equation (C.9) can be written in the form of:

$$\frac{\varepsilon_{ns} - \lambda Q^2}{\varepsilon} = \boldsymbol{P_n}(1 + \lambda) + \varepsilon_{ns} - \lambda\,. \tag{C.17}$$

Since $\boldsymbol{P_n} = \boldsymbol{P_{n_o}}$, $Q = Q_0$, and $\varepsilon = \varepsilon_o = \varepsilon_{ns} - \varepsilon_{ns}^2/2$ for stagnation conditions, Equation (C.17) can be written in the form:

$$\frac{\varepsilon_{ns} - \lambda Q^2}{\varepsilon} = \left[\boldsymbol{P_{n_o}}(\mathbf{1} + \lambda) + \varepsilon_{ns} - \lambda\right] - F, \tag{C.18}$$

where

$$F = \frac{1}{1 - \frac{\varepsilon_{ns}}{2}} - \frac{\varepsilon_{ns} - \lambda Q^2}{\varepsilon}. \tag{C.19}$$

Thus,

$$\boldsymbol{P_n} = \boldsymbol{P_{n_o}} - \frac{F}{(1+\lambda)}, \tag{C.20}$$

and

$$\boldsymbol{P_{n_o}} = \frac{1}{1+\lambda}\left(\frac{1}{1 - \frac{\varepsilon_{ns}}{2}} + \lambda - \varepsilon_{ns}\right). \tag{C.21}$$

Interestingly, F is simply a function of λ and ε_{ns} for a given geometry. According to simple impact theory, $\boldsymbol{P_n}$ varies with the surface's angle with the stream direction. Thus, casting Equation C.20 into the well-known form of modified Newtonian impact theory for flow over a spherical nose cap (i.e., $\boldsymbol{P_{n_o}} = 1 - K\,sin^2\eta$, where η is the angle between the freestream velocity vector and the surface unit normal vector) gives:

$$\frac{\boldsymbol{P_n}}{\boldsymbol{P_{n_o}}} = 1 - \frac{G}{\boldsymbol{P_{n_o}}(1+\lambda)}\,sin^2\eta\,, \tag{C.22}$$

where

$$G = \frac{F}{sin^2\eta}, \tag{C.23}$$

or

$$F = G\,sin^2\eta\,, \tag{C.24}$$

and G must approach unity as λ and ε_{sn} approaches zero and $\boldsymbol{P_{n_o}}$ approach unity, and not equal to zero.

This analysis assumes that Equation (C.24) does not change form for flow conditions other than Newtonian. Since $\boldsymbol{P_{n_o}}$ and $1 + \lambda$ are nearly unity for hypersonic flow, the only significant difference in form between Equation (C.22) and the modified

Newtonian pressure relation is the "variable" $G = G\ (\lambda\ ,\ \eta\ ,\ \varepsilon_{ns})$ and the Newtonian "empirical constant" *K*.

Some experimentation showed the rather remarkable fact that the pressure distribution is accurately produced by treating *G* as a constant based on local sonic line conditions at the surface. Thus, for sonic conditions:

$$G_{sl} = \left(\frac{1}{1 - \frac{\varepsilon_{ns}}{2}} - \frac{1 - \lambda}{J} \right) \frac{1}{sin^2 \eta_{sl}}, \tag{C.25}$$

where J is given by

$$J = 1.6487 \left[1 - \frac{\varepsilon_{ns}}{4} \left(2 + \frac{\lambda}{\varepsilon_{ns}} \right) \right] = \frac{\varepsilon_{sl}}{\varepsilon_{ns}}, \tag{C.26}$$

and a correlation of G_{sl} as a function of λ and ε_{ns} is provided in Figure C.1 for a wide range of flow conditions for both ideal and real air.

The EBLUNT solution provides similar accuracies as some of the best computational methods. The difference is that EBLUNT can be used by either slide rule or an electric mechanical calculator such as a Monroe.

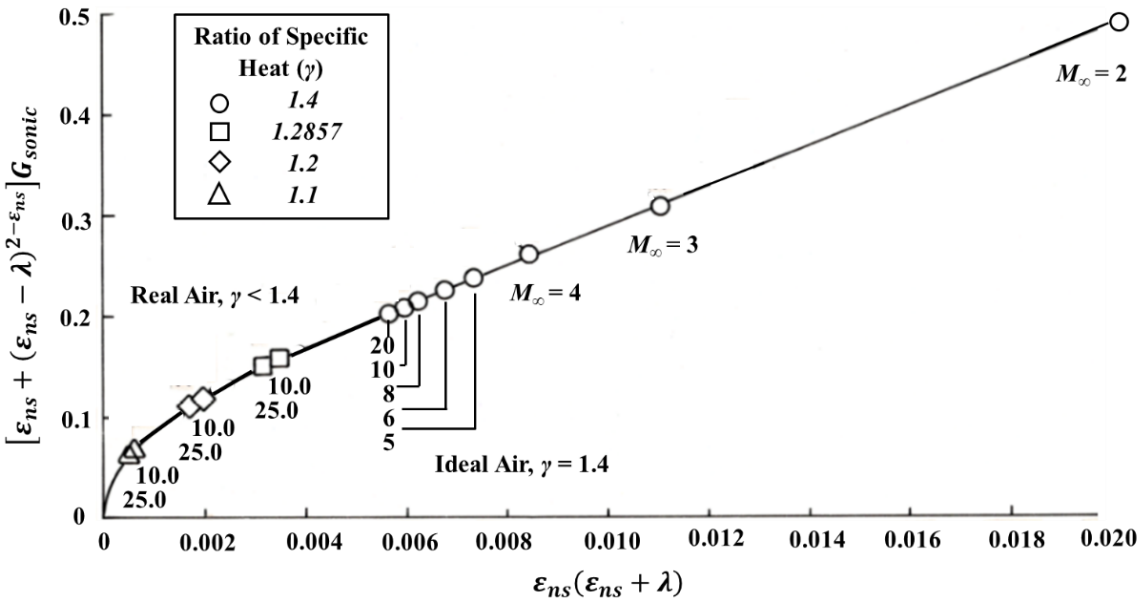

Figure C.1 Values of G based on sonic line conditions for a sphere

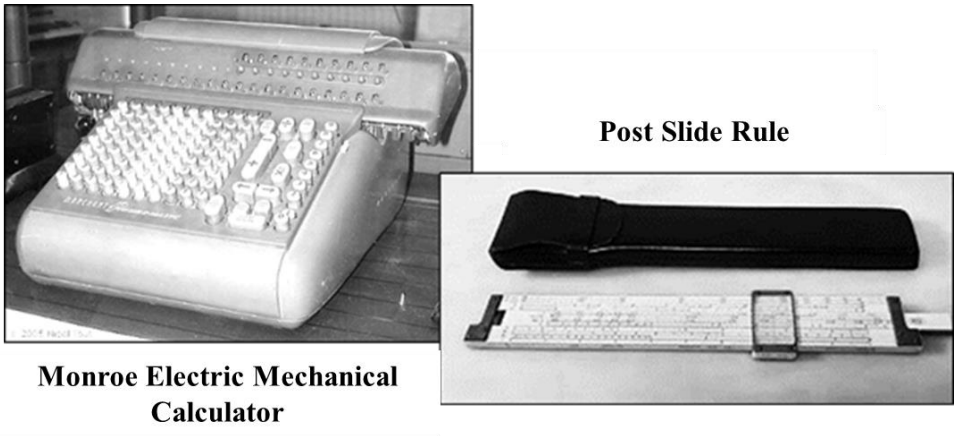

Figure C.2 Monroe Electric Mechanical Calculator and Post slide rule

Figures C.3 through C.5 provide evidence that the developed analytical method for calculating the pressure distribution on blunt bodies by EBLUNT delivers outstanding accuracy.

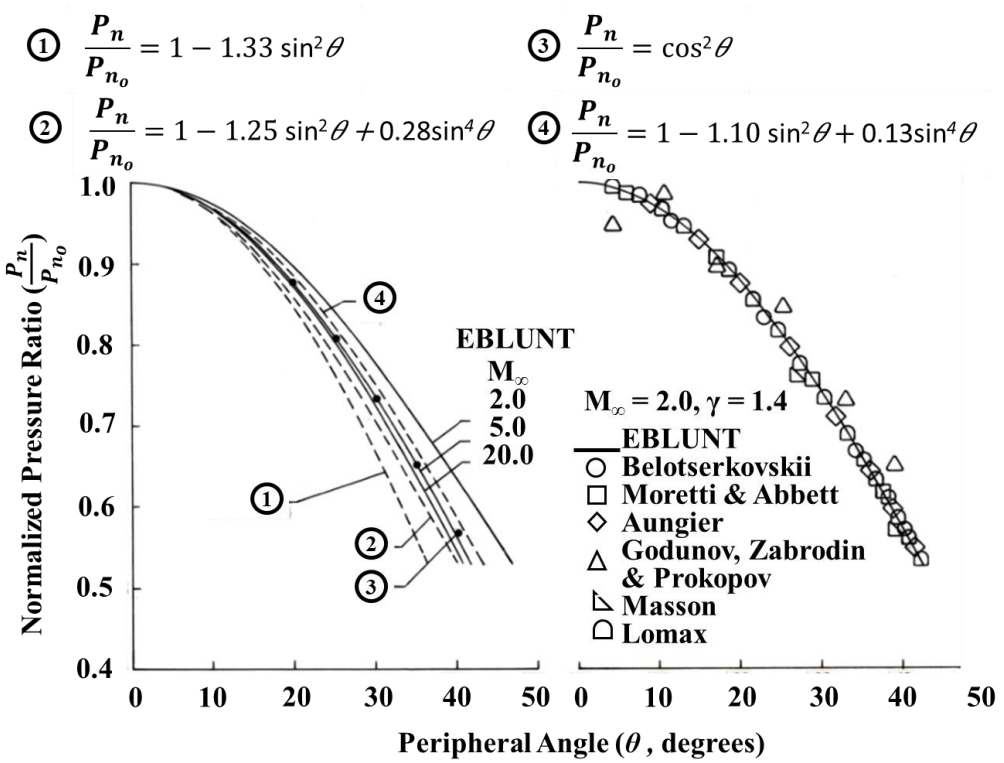

Figure C.3 Comparison of EBLUNT with well-known solutions for a sphere

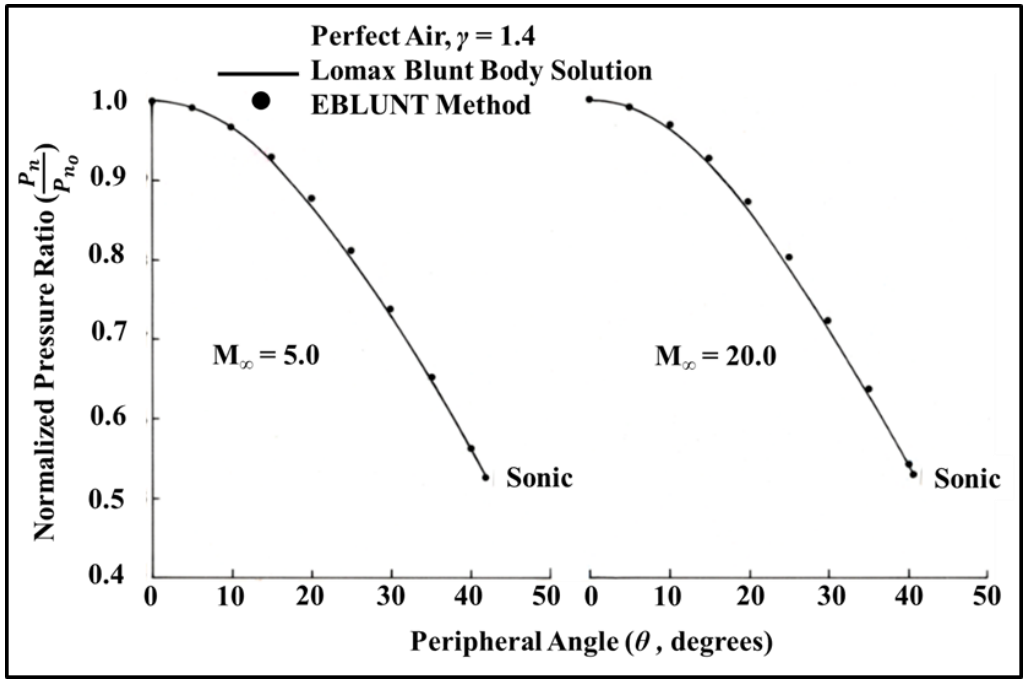

Figure C.4 Comparison of EBLUNT with Lomax's exact solution for a sphere in ideal flow

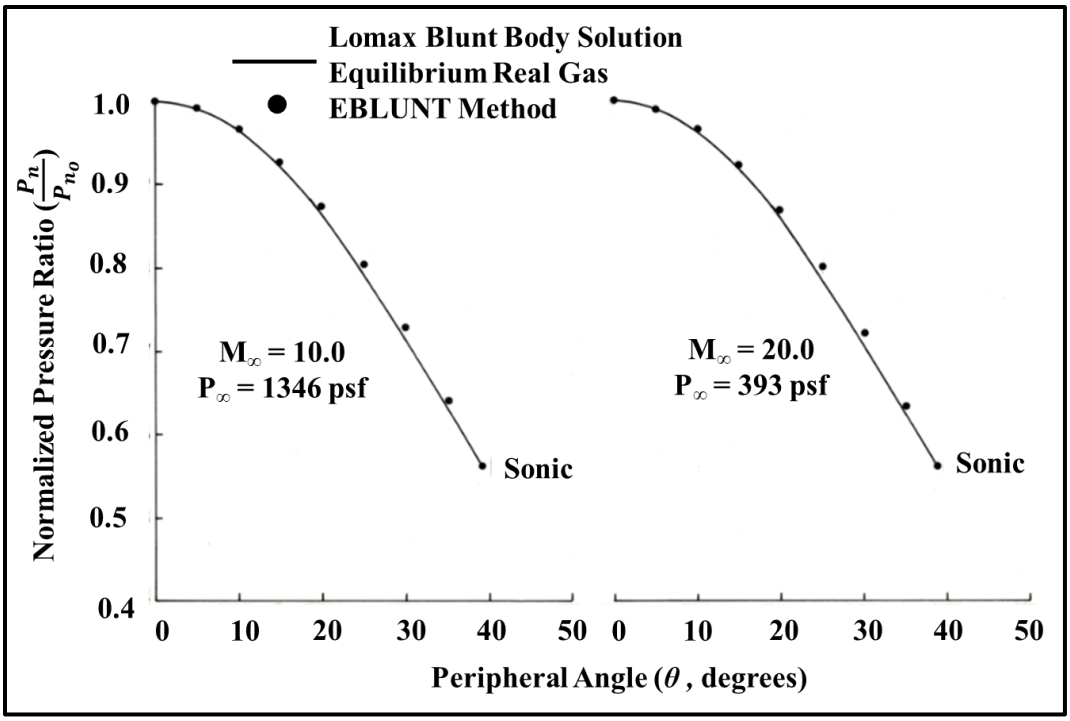

Figure C.5 Comparison of EBLUNT with Lomax's exact solution for a sphere in equilibrium flow

For completeness, the pressure relation is extended to $\eta = \theta = 90°$. However, Equation (C.22) begins to diverge from experimental data immediately downstream of the sonic line. Thus, Equation (C.22) can be expanded to include two-second order terms that are also functions of the ratio of specific heat, density, velocity, and geometry.

- For $\eta_{sonic} \leq \eta \leq 80°$

$$\frac{\boldsymbol{P_n}}{\boldsymbol{P_{n_o}}} = 1 - \frac{G}{\boldsymbol{P_{n_o}}(1+\lambda)} sin^2\eta + \frac{\varepsilon_{ns}}{\boldsymbol{P_{n_o}}(1+\lambda)} sin(\eta - \eta_{sl}) , \qquad \text{(C.27)}$$

- For $80° \leq \eta \leq 90°$

$$\frac{\boldsymbol{P_n}}{\boldsymbol{P_{n_o}}} = 1 - \frac{G}{\boldsymbol{P_{n_o}}(1+\lambda)} sin^2\eta + \frac{\varepsilon_{ns}}{\boldsymbol{P_{n_o}}(1+\lambda)} sin(\eta - \eta_{sl}) + \frac{\varepsilon_{ns}}{2\boldsymbol{P_{n_o}}(1+\lambda)} sin(\eta - 80°) , \qquad \text{(C.28)}$$